

Spring 5-22-2020

## Displacement Rates and Lateral Continuity of Baton Rouge Fault System Segments in the Vicinity of the East Orleans Land Bridge, Louisiana

Robert W. Mohollen Jr.  
*University of New Orleans*, [rwmohol1@uno.edu](mailto:rwmohol1@uno.edu)

Follow this and additional works at: <https://scholarworks.uno.edu/td>



Part of the [Geomorphology Commons](#)

---

### Recommended Citation

Mohollen, Robert W. Jr., "Displacement Rates and Lateral Continuity of Baton Rouge Fault System Segments in the Vicinity of the East Orleans Land Bridge, Louisiana" (2020). *University of New Orleans Theses and Dissertations*. 2771.

<https://scholarworks.uno.edu/td/2771>

This Thesis is protected by copyright and/or related rights. It has been brought to you by ScholarWorks@UNO with permission from the rights-holder(s). You are free to use this Thesis in any way that is permitted by the copyright and related rights legislation that applies to your use. For other uses you need to obtain permission from the rights-holder(s) directly, unless additional rights are indicated by a Creative Commons license in the record and/or on the work itself.

This Thesis has been accepted for inclusion in University of New Orleans Theses and Dissertations by an authorized administrator of ScholarWorks@UNO. For more information, please contact [scholarworks@uno.edu](mailto:scholarworks@uno.edu).

Displacement Rates and Lateral Continuity of Baton Rouge Fault System Segments in the  
Vicinity of the East Orleans Land Bridge, Louisiana

A Thesis

Submitted to the Graduate Faculty of the  
University of New Orleans  
in partial fulfillment of the  
requirements for the degree of

Master of Science  
in  
Earth and Environmental Sciences  
Structural Geology

By

Robert W. Mohollen Jr.

B.S. West Chester University, 2016

May, 2020

## Acknowledgements

I would like to sincerely thank my advisor, Dr. Mark Kulp, for his support and guidance throughout my graduate career. I would also like to thank Brad Robison and Dr. Elizabeth McDade for their undivided support as members of my committee. I extend my gratitude to Chris McLindon for his help with acquiring the seismic data and biostratigraphy data used in this study. Donations from companies were vital to completing this research including: Paleo Data Inc. for their biostratigraphy donations, Velocity Databank Inc. for their velocity survey donations, Platte River Associates Inc. for their donation of the *BasinMod* software, and IHS Markit for their donation of *IHS Kingdom* software. I would like to recognize the United States Geological Survey, the Louisiana Department of Natural Resources, the New Orleans Geological Society, Western Geco, and the National Oceanic and Atmospheric Administration for their generous donations to this study. My thanks go to Michael Brown, Joseph Hankerson, Jessica Villers, Jarrett Levesh, and Jared Bullock for their help with performing the field work necessary to complete this study. Finally, I would not have been able to accomplish this task without the help and support from my family.

# Table of Contents

<b>List of Figures</b> .....	<b>v</b>
<b>List of Tables</b> .....	<b>viii</b>
<b>Abstract</b> .....	<b>ix</b>
<b>Chapter 1. Introduction, Problem Statement, and Significance</b> .....	<b>1</b>
1.1 Introduction.....	1
1.2 Problem Statement.....	6
1.3 Purpose.....	7
.....	
<b>Chapter 2. Geologic History of the Baton Rouge Fault System</b> .....	<b>9</b>
2.1 Paleocene- Middle Miocene History and Fault Activity .....	9
2.2 Late Miocene-Pliocene History and Fault Inactivity .....	13
2.3 Pleistocene-Holocene Geologic History .....	14
2.3.1 Pleistocene Fault Reactivation and Displacement Rates .....	15
2.3.2 Pleistocene-Holocene Contact.....	17
2.3.3 Holocene Fault Activity and Displacement Rates.....	23
2.3.4 Subsidence .....	24
2.4 Geologic History of the Pontchartrain Basin.....	25
2.5 Formation of Lake Pontchartrain and Lake Borgne .....	26
<b>Chapter 3. Methodology</b> .....	<b>28</b>
3.1 LDNR Well Log Data.....	28
3.2 Integration of Seismic: Lake Borgne 3-D and Lake Pontchartrain 2-D Data.....	31
3.2.1 Seismic Analysis .....	31
3.2.2 Biostratigraphic Tie to Seismic .....	33
3.2.3 Fault Displacement Rates.....	36
3.3 <i>BasinMod</i> Burial History Diagrams.....	37
3.4 Shallow Vibracore Data.....	38
3.4.1 Chronostratigraphic Correlations .....	39
3.4.2 Lithostratigraphic Correlations.....	40
3.4.3 Pleistocene-Holocene Sediment Analysis .....	41
3.4.4 Pleistocene-Holocene Stratigraphic Analysis .....	44
3.5 Chirp Seismic Data .....	46
3.6 Aerial Imagery and Lidar Data .....	48
<b>Chapter 4. Results</b> .....	<b>49</b>
4.1 LDNR Well Log Correlations.....	49
4.2 Lake Pontchartrain and Lake Borgne Seismic Interpretation .....	54
4.3 <i>BasinMod</i> Burial History .....	57
4.4 Shallow Vibracore Correlations.....	60
4.5 Chirp Seismic Faults .....	78
4.6 Aerial Imagery and Lidar.....	84
<b>Chapter 5. Discussion</b> .....	<b>93</b>
5.1 Fault Activity .....	93

5.2 Inactive Fault Segments .....	94
5.3 Preservation of Stratigraphy .....	95
5.4 Implications of <i>BasinMod</i> Burial History .....	97
5.5 Impacts to Local Geomorphology .....	98
<b>Chapter 6. Conclusions .....</b>	<b>99</b>
<b>References.....</b>	<b>101</b>
<b>Appendix A: Shallow Vibracore Descriptions.....</b>	<b>106</b>
<b>Appendix B: Chirp Seismic Collection Information.....</b>	<b>129</b>
<b>Vita.....</b>	<b>133</b>

## List of Figures

Figure 1. Geologic Map of the Pontchartrain Basin .....	2
Figure 2. Map of the Two Dominant Fault Trends of the Baton Rouge Fault System.....	3
Figure 3. Map of the East Orleans Land Bridge .....	3
Figure 4. The Lake Borgne Fault System Map.....	4
Figure 5. Study Area Location Map and Previous Study Locations.....	4
Figure 6. Depositional Episodes in the Lake Pontchartrain Basin.....	11
Figure 7. Location of the Cenozoic Shelf Margins Map .....	12
Figure 8. Conceptual Model of Gravity-Slumping Events .....	12
Figure 9. Locations of Cross-Sections in Chef Menteur, LA .....	18
Figure 10. Chef Menteur Cross-Section A-A' .....	19
Figure 11. Chef Menteur Cross-Section C-C' .....	19
Figure 12. Locations of Cross-Sections in The Rigolets, LA .....	20
Figure 13. Rigolets Cross-Section A-A' .....	21
Figure 14. Rigolets Cross-Section B-B' .....	21
Figure 15. Pleistocene-Holocene Stratigraphic Boundaries .....	22
Figure 16. Pleistocene-Holocene Contact Contours .....	22
Figure 17. Holocene Thickness Contours .....	23
Figure 18. Conceptual Model of the Formation of Lake Pontchartrain.....	27
Figure 19. Locations of the 145 Well Logs .....	29
Figure 20. Locations of 31 Well Logs with Available Biostratigraphy.....	30
Figure 21. Proposed Surface Fault Trace Locations.....	33
Figure 22. Lake Pontchartrain Time-Depth Survey Graph.....	34
Figure 23. Lake Borgne Seismic Synthetic.....	34
Figure 24. Amplitude Spectrums for 3-D and 2-D datasets .....	35
Figure 25. Land Bridge Vibracore Locations and Cross-Section Locations .....	39
Figure 26. Generalized Composite Logs of Lake Pontchartrain.....	43
Figure 27. Generalized Composite Logs of Lake Pontchartrain Borings.....	45

Figure 28. Collected Chirp Line Locations with Structure Map Polygon .....	47
Figure 29. Goose Point Fault Well Log Cross-Section.....	50
Figure 30. Lake Pontchartrain Fault Well Log Cross-Section.....	51
Figure 31. Lake Borgne Fault and Land Bridge Well Log Cross-Section.....	52
Figure 32. Goose Point Fault Expansion Indices Graph.....	53
Figure 33. Goose Point Fault Displacement Graph .....	53
Figure 34. Goose Point Fault Expansion Indices During Time Graph .....	54
Figure 35. <i>Heterostegina SP</i> Structure Map .....	56
Figure 36. Fault Offset Rates for Increments of Time in 2-D Seismic.....	57
Figure 37. <i>BasinMod</i> Burial History Diagrams for Goose Point Fault.....	59
Figure 38. Vibracore Cross-Section A-A' .....	65
Figure 39. Vibracore Cross-Section B-B' .....	66
Figure 40. Vibracore Cross-Section C-C' .....	67
Figure 41. Vibracore Cross-Section D-D' .....	68
Figure 42. Vibracore Cross-Section E-E' .....	69
Figure 43. Vibracore Cross-Section F-F' .....	70
Figure 44. Vibracore Cross-Section G-G' .....	71
Figure 45. Vibracore Cross-Section H-H' .....	72
Figure 46. Vibracore Cross-Section A-A' with Isochron Calculations .....	73
Figure 47. Vibracore Cross-Section B-B' with Isochron Calculations.....	74
Figure 48. Vibracore Cross-Section C-C' with Isochron Calculations.....	75
Figure 49. Vibracore Cross-Section D-D' with Isochron Calculations .....	76
Figure 50. Vibracore Cross-Section F-F' with Isochron Calculations .....	77
Figure 51. Chirp Line 10 with Pleistocene Surface Pick and Goose Point Fault Pick .....	80
Figure 52. Pleistocene Structure Map using Chirp Seismic .....	81
Figure 53. Amite River Paleochannel.....	82
Figure 54. Chirp Line 12 with VC-LP-03 Overlain for Biostratigraphy Correlations .....	83
Figure 55. Surface Expressions of Faults in Southeastern Louisiana.....	85

Figure 56. Surface Expressions Located in the Study Area.....	86
Figure 57. Persistent Land Loss Map (1932-2015) .....	87
Figure 58. Landsat Look Viewer Comparison of Study Area from 1982-2018 .....	88
Figure 59. 2003 Lidar Map of Study Area.....	89
Figure 60. Enhanced View of 2003 Lidar Map .....	90
Figure 61. 2018 Lidar Map of Study Area.....	91
Figure 62. Enhanced View of 2018 Lidar Map .....	92

## List of Tables

Table 1. List of Previous Fault Studies and Rates of Fault Slip .....	16
Table 2. Dip Angle Estimations for Fault Segments .....	32
Table 3. Shallow Biostratigraphic Horizon Estimations.....	56
Table 4. <i>BasinMod</i> Net-to-Gross Values .....	58
Table 5. Radiocarbon Sample Information.....	61
Table 6. Isochron Calculations .....	63

## **Abstract**

The Baton Rouge Fault System (BRFS) is a system of deep-seated, east-trending normal faults. Analysis of a 2-D industry seismic dataset in Lake Pontchartrain and two, 3-D datasets in Lake Borgne, revealed three faults that may show lateral continuity beneath the East Orleans Land Bridge (EOLB). Biostratigraphy from 33 oil/gas industry well logs were used for correlation with deep seismic data. *BasinMod* was used to generate a burial history of the Cenozoic strata. Cross sections of 22 collected vibracores with 500 yr BP interval isochron estimations, calculated from 17 vibracore samples of radiocarbon dated ( $C^{14}$ ) relict marsh organics and *Rangia cuneata* shells, show fault displacement in Holocene stratigraphy. A grid of high-resolution, Chirp seismic data collected shows visible offset of strata during the Late Pleistocene and Holocene. Aerial imagery and Lidar datasets show possible scarps and other surface expressions along the projected surface traces of the BRFS on the EOLB.

Keywords: Baton Rouge Fault System, Offset, Land Bridge, Biostratigraphy, Lateral Continuity

# **Chapter 1. Introduction, Problem Statement, and Significance**

## **1.1 Introduction**

The Baton Rouge Fault System (BRFS) is a series of down-to-the-south, east trending normal faults that form the northern boundary of the Pontchartrain Basin (Lopez et al., 1991). The BRFS, extends approximately 11 kilometers (7 mi) south and 92 kilometers (57 mi) east-southeast of Baton Rouge through Lake Pontchartrain, and forms a border between physiographically different Pleistocene terraces to the north and Holocene delta deposits to the south (Fig. 1). This abrupt change in surface geology exists due to high subsidence to the south and isostatic uplift to the north along the BRFS (Gagliano et al., 2003). This accommodation along BRFS detachment surfaces was filled with sediments resulting in the formation of “growth faults”, a distinct type of normal fault characterized by syndepositional movement along the fault surface that results in more sediment accumulation on the down-thrown, or hanging wall side of the fault.

Lopez et al. (1998) mapped two dominant trends within the BRFS. One trend extends along the southern half of Lake Pontchartrain (Fig. 2) and contains east–striking sinuous faults with numerous bifurcated segments (Lopez et al., 1998). A second trend of east striking normal faults parallel the northeast shore of Lake Pontchartrain (Lopez et al., 1998). These two fault trends are in the study area of this project, which extends across Lakes Pontchartrain, Borgne, St. Catherine, and the “East Orleans Land Bridge” (EOLB), a low-lying area of marsh that separates Lake Pontchartrain and Lake Borgne (Fig. 3). East and south of their fault trends, the BRFS may link with the Lake Borgne Fault System (LBFS). The LBFS is another group of down-to-the-south, east-trending normal faults located below central Lake Borgne (Fig. 4). The study area of

this project includes: the eastern portion of the BRFs, the LBFS, and the area between the two previously mapped systems (Fig. 5).

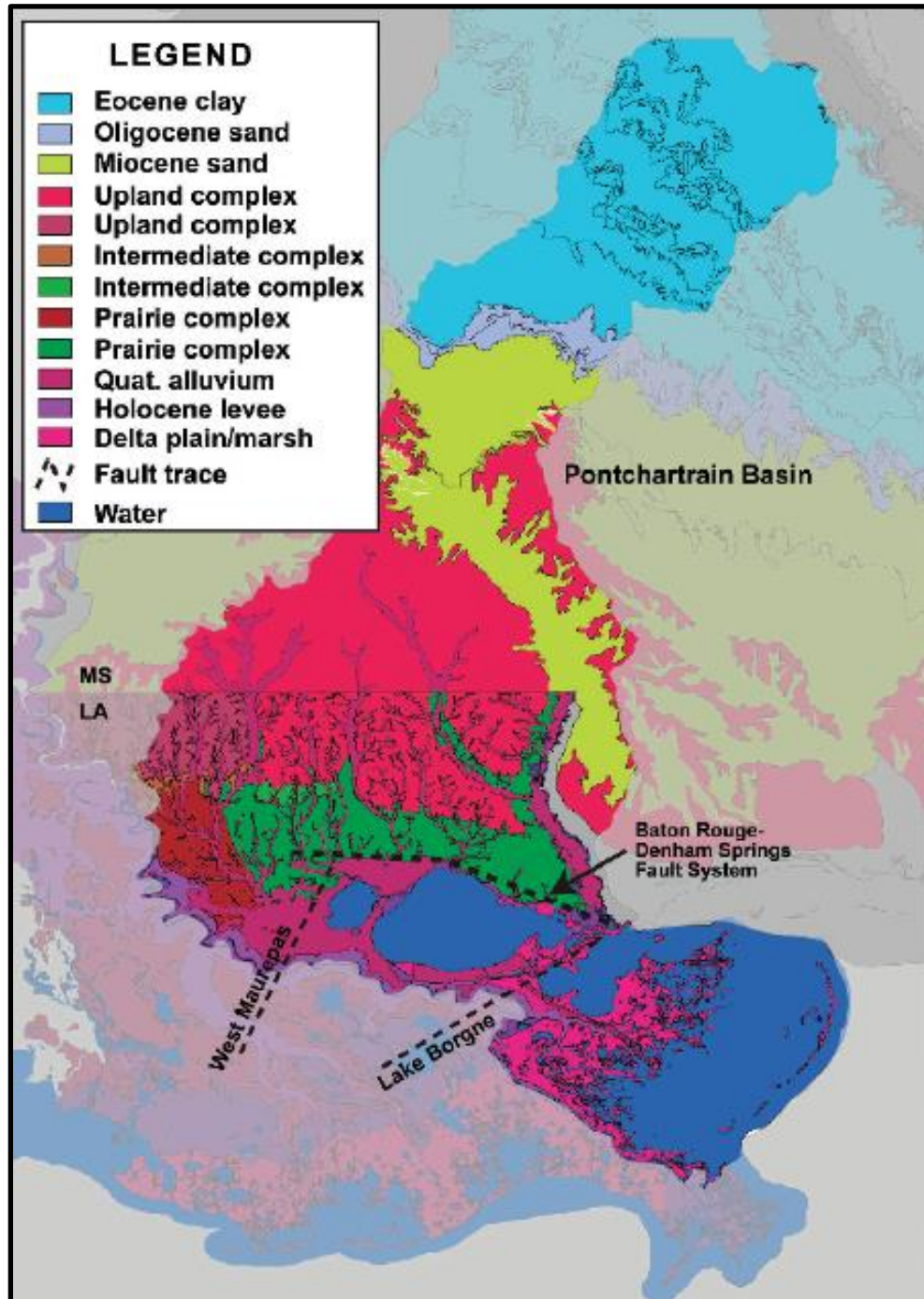


**Figure 1.** Geologic map showing the extent of the Pontchartrain Basin as well as the physiographic boundary formed by the Baton Rouge-Denham Springs Fault System, separating Pleistocene uplands to the north from Holocene deltaic deposits to the south (from Flocks et al., 2009a). Dashed lines indicate structural alignments that counter depositional strike (from Gagliano et al., 2003).

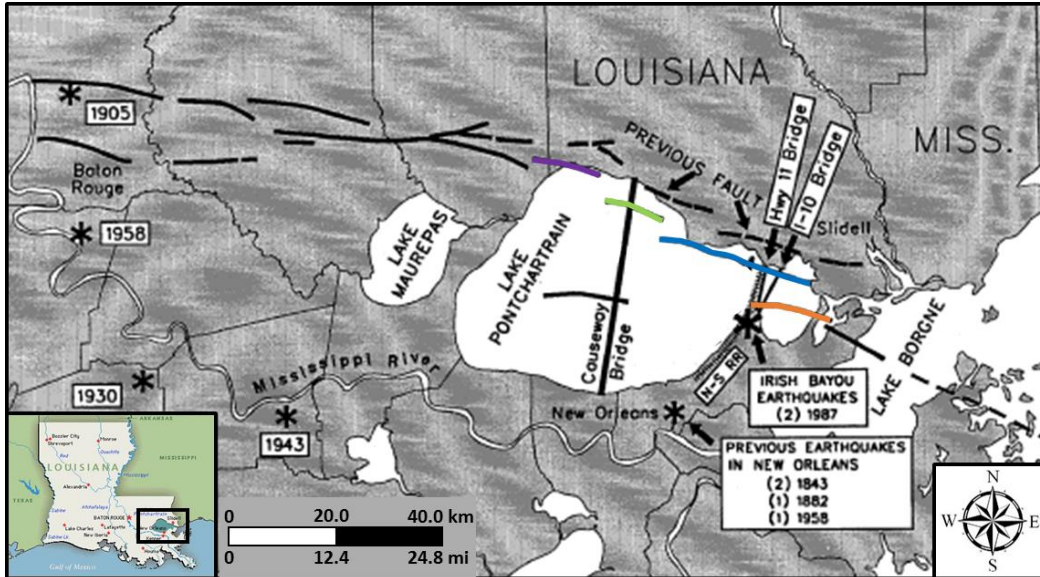


**Figure 2.** Map of fault segments identified by Lopez et al. (1997) as the Baton Rouge Fault System and named by Lopez and Connor (2001). The purple line, light green line, blue line, and orange fault represent the Madisonville Point, Causeway, Goose Point, and South Point faults, respectively. The dashed lines mark previous surface trace interpretations. The asterisks mark the locations of recorded earthquake events that are thought to be a result of BRFS motion (Lopez et al., 1997). The Highway 11 Bridge, I-10 Bridge, and Norfolk-Southern Railroad (labeled along the east side of Lake Pontchartrain) have all undergone local offset, proposed to be the result of recent fault motion.



**Figure 3.** The East Orleans Land Bridge refers to an area of brackish marsh and deltaic deposits that form an approximately 320 km<sup>2</sup> (~123 mi<sup>2</sup>) parcel of land separating the modern-day Lake Pontchartrain from Lake St. Catherine and Lake Borgne (red polygon).



**Figure 4.** The light blue, red, and light orange labeled lines indicate the Lake Borgne Fault System (modified from Frank, 2016).

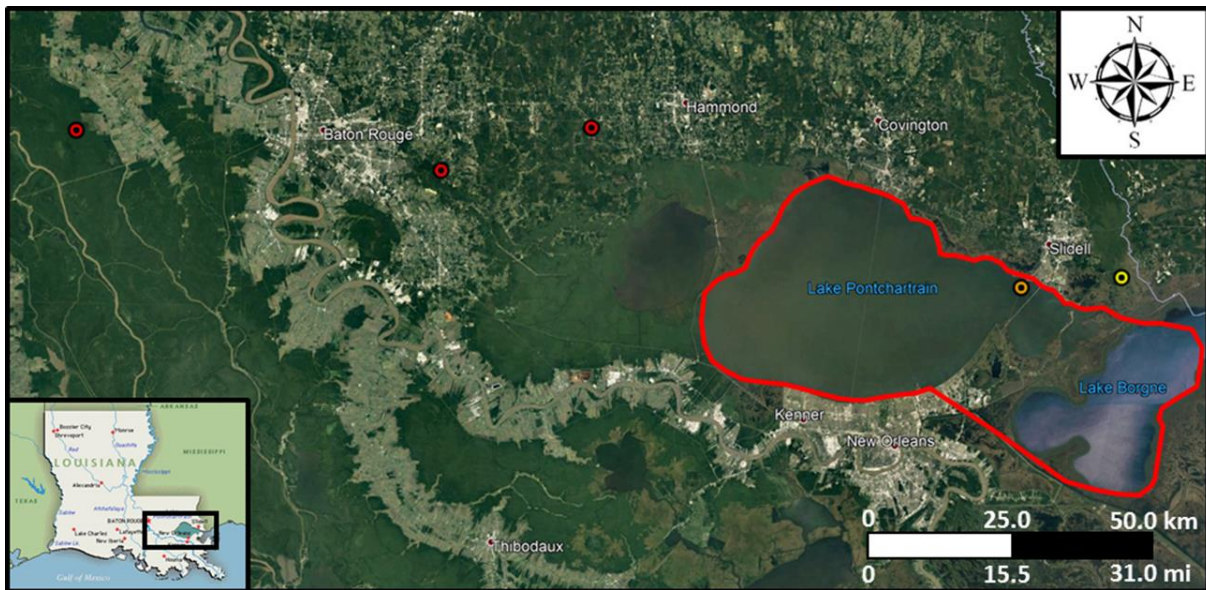


**Figure 5.** The area within the red polygon above marks the extent of the study area. This study area contains a 2-D seismic dataset, a combination of two, 3-D seismic datasets, a collection of vibracores that were collected, a collection of well logs provided by SONRIS, and a collection of Chirp seismic lines that were collected. The extent of previous studies that involved calculations of fault slip within the Baton Rouge Fault System are also shown in this map. The red circles, orange circle, and yellow circle mark the locations of studies including Shen et al. (2016), Lopez (1991), and Yeager et al. (2012), respectively.

An array of transportation infrastructure crosses the projected surface traces of faults of the BRFS. For example, the Highway 11 Bridge, Norfolk Southern Railroad and Highway 90 trend directly across suggested fault traces and constitute critical routes from the south shore to north shore of southeast Louisiana. The effect of fault motion has already been suggested for some of these structures. Lopez (1991) identified that fault movement beneath the Highway 11 Bridge caused a 15.2 cm (6.0 in.) offset in the guard-rail along the bridge, along the projected surface trace of the Goose Point Fault within Lake Pontchartrain (Lopez, 1991). The Norfolk-Southern railroad, which was rebuilt between 1986-1987, underwent 7.6-10.2 cm (3.0-4.0 in.) of offset where it crosses the southern fault (labeled the South Point Fault) of the BRFS in Lake Pontchartrain as well (Lopez et al., 1997).

Impacts to local geomorphology as a result of displacement along the BRFS have been documented in the past (Gagliano et al., 2003; Haggar, 2014; Lopez et al., 1997; Roland et al., 1981; Shen et al., 2016; McCulloh, 2001). Gagliano et al. (2003) suggested that fault displacement and fault-related subsidence can cause fragmentation of marsh and conversion of marsh to open water. Additionally, surface expressions such as distinct traces and scarps, broken marsh, channel alignments, and shoreline alignments along the surface traces of faults have been proposed as evidence of fault-related subsidence (Gagliano et al., 2003; Levesh, 2019; Frank, 2016; Haggar, 2014; Lopez et al., 1997). Marsh breakup and conversion to open water, as a result of fault motion, may progress through stages that occur during long intervals of time ( $10^3$ - $10^4$  yrs) such as the BRFS formation of the northern boundary of Lake Pontchartrain, or during short time intervals ( $10^1$ - $10^2$  yrs) such as the Empire Fault of the Golden Meadow Fault Zone, and include submergence of both coastal marshes and ridges (Gagliano et al., 2003; Lopez et al., 1997).

In this study, aerial imagery and light detection and ranging (Lidar) data are examined to investigate whether there exists evidence of fault influence on surface features at short time scales ( $10^1$ - $10^2$  yrs). Perhaps significant is that the EOLB and surrounding areas are characterized by brackish marshes that are poorly drained and ponded most of the time (Gagliano et al., 2003; Trahan, 1989; Sasser et al., 2008). This characterization is significant for mapping the extent of brackish marsh of the land bridge and identifying poorly drained marsh that may be submerged as a result of BRFS fault motion during the last 0.1 ky. The focus of this study is to evaluate the subsurface location of faults and whether there exists 1 (~last 0.1 ky) surface or subsurface expressions that are a result of motion along the BRFS.

## ***1.2 Problem Statement***

This research focuses on the following questions: 1) Is there lateral continuity between fault segments of the BRFS and LBFS across eastern Lake Pontchartrain and beneath the EOLB, 2) Have faults of the east Baton Rouge Fault System impacted latest Quaternary stratigraphic relationships and geomorphology, 3) What is the history of fault slip along the eastern Baton Rouge faults, and 4) Can rates of fault slip be quantified for pre-Late Quaternary stratigraphic units? To address these questions a variety of datasets are available (i.e. energy industry and State of Louisiana sources), namely 1) hydrocarbon industry standard 2-D and 3-D seismic data, 2) deep well log data, 3) shallow vibracores, and 4) shallow Compressed High-Intensity Radar Pulse (Chirp) seismic. Evidence of lateral continuity between fault segments of the BRFS and evidence of Holocene displacement, if any, are necessary to address the possible effects of fault induced subsidence on the local geomorphology. This study does not attempt to quantify the amount of subsidence caused by the faults, but rather attempts to identify whether there exists surface or near surface expressions as a result of fault-related subsidence.

### **1.3 Purpose**

Relative sea level rise (RSLR) contributes to most of the coastal land loss that shapes the Louisiana coastline today, and some of the 20<sup>th</sup> century RSLR is thought to be due to fault-driven subsidence in coastal Louisiana (e.g. Gagliano et al., 2003; Gagliano, 2005). Gagliano et al. (2003) also state that fault displacements may initiate geomorphologic changes and change depositional patterns such as the formation of crevasses, fluvial avulsions, submergence of natural levee ridges, barrier island fragmentation, and enlargement or disappearance of lakes and bays. Moreover, faults can affect local, surficial infrastructure such as bridges and roadways, as was documented by Lopez et al. (1991,1997) for transportation infrastructure crossing Lake Pontchartrain. To date, however, there has been no clear evidence as to whether the BRFS has had a direct effect on the geomorphology of the East New Orleans Land Bridge.

Wetland loss due to subsidence is widely documented as a geomorphologic issue in southern Louisiana (Haggar, 2014; Gagliano et al., 2003; Gagliano et al., 2005; Dokka, 2006; Kulp, 2000; Levesh, 2019; Yuill et al., 2009). Gagliano et al. (2003) state that approximately 46% of the total coastal Louisiana landloss (1908 km<sup>2</sup> of 4196 km<sup>2</sup>) has occurred in a triangular area south of New Orleans in the Terrebonne and Barataria Basins and Mississippi Birdfoot delta between 1932-1990. Gagliano et al. (2003) also propose that the primary cause of loss in this triangular area is fault-driven subsidence. Levesh (2019) determined one of the causes of landloss in his study area (Lake Delacroix) was due to slip of the Delacroix Island Fault System. Other studies (Kulp, 2000; Dokka, 2006; Yuill et al., 2009) highlight the importance of studies into the cause for areas of increased subsidence rates in order to better understand the effects of subsidence on Holocene geomorphology. Investigations into the primary cause of marsh landloss

in the Pontchartrain Basin as well as the possible relationship between marsh landloss and fault-driven subsidence in this study area have yet to be conducted.

## **Chapter 2. Geologic History of Baton Rouge Fault System**

### ***2.1 Paleocene- Middle Miocene History and Fault Activity***

The northern Gulf of Mexico (GoM) was the site of widespread Gulfward prograding fluvio-deltaic systems during the Cenozoic era (Galloway et al., 1991). This series includes six major offlapping progradational units: the lower Wilcox (Paleocene-early Eocene), upper Wilcox (early Eocene), Vicksburg/Frio (Oligocene), early-to-middle Miocene, late Miocene, and Pliocene-Pleistocene. These major units are further divided into 18 basin-margin sequences shown in figure 6. Galloway et al. (1991) state that these offlapping fluvio-deltaic systems are characterized by thick delta-front and shore-zone lithofacies, growth faulting, salt diapirism, and wide-spread development of geopressured intervals.

Each regressive progradational unit was a result of progradation of the major delta systems beyond the previously extant shelf margin and deposition of several well-defined, sand-rich stratigraphic units, bound by widespread transgressive marine shale wedges along the basin-ward margin of the northern GoM Basin (Galloway et al., 1991; Galloway et al., 2000; Galloway et al., 2010; Wu, 2004). Major deltaic offlap occurred in units of the lower Wilcox formation, beginning in the late Paleocene (Galloway et al., 1991). These fluvio-deltaic systems and the massive amount of associated sedimentation resulted in periods of substantial basin loading and growth faulting along rapidly advancing shelf margins as well as salt mobilization across the region (Galloway et al., 1991).

Cenozoic fault systems of the northern GoM are genetically different than regional Mesozoic fault systems that formed during the opening of the GoM basin by rifting (Shen et al., 2016; Nunn, 1985). Mesozoic faults in this study area became inactive with the waning of the

continental rift event that resulted in the formation of the Atlantic Ocean basin and Gulf basin (Worrall and Snelson, 1989). Cenozoic growth faults (including the BRFS) penetrate post-rift sediments (Nunn, 1985; Peel et al., 1995; Rowan et al., 2000; Worrall and Snelson, 1989). Galloway et al. (2000) mapped the location of Cenozoic shelf margins from Cretaceous through Pleistocene time intervals (Fig. 7). The proximity of the Cenozoic shelf margin in relation to sediment loading in the northern GoM presents a possible explanation for episodic fault-growth in the study area. Sediment loading along the continental shelf in the early Cenozoic along with the process of gravity slumping (Fig. 8) may have initiated fault slip in this study area (Galloway et al., 2000).

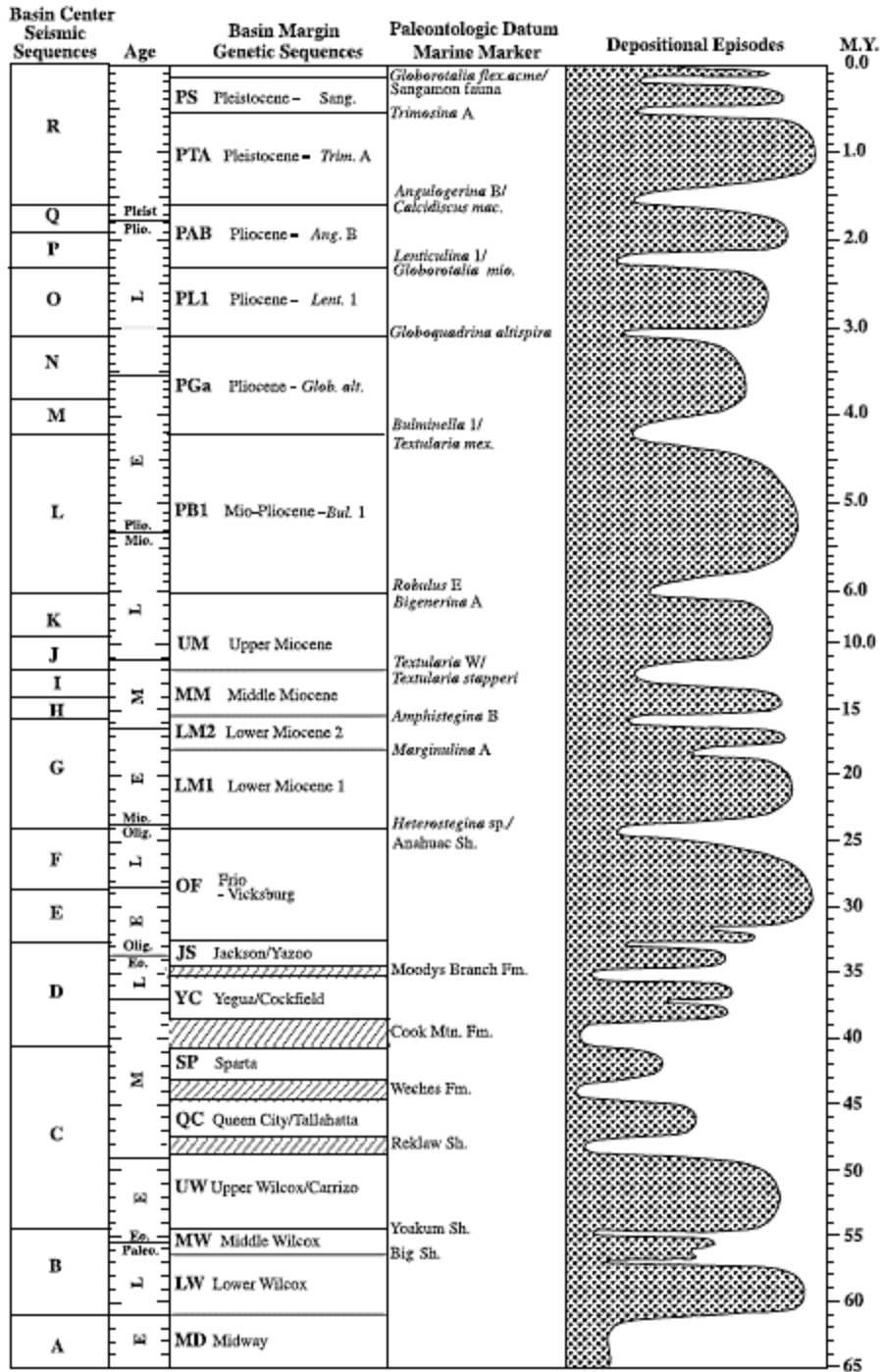


**Figure 6.** Diagram showing the division of Cenozoic depositional episodes into 18 basin center seismic sequences. These sequences are bound by marine shale units (visible as white peaks in the depositional episode column). Paleontological markers typically occur during these intervals between depositional episodes. These basin margin genetic sequences were further defined in Galloway et al. (2000). Basin-center seismic sequences were defined and mapped by Feng (1995). These basin margin genetic sequences and paleontological markers were used to interpret Cenozoic stratigraphy in the seismic datasets of this study.

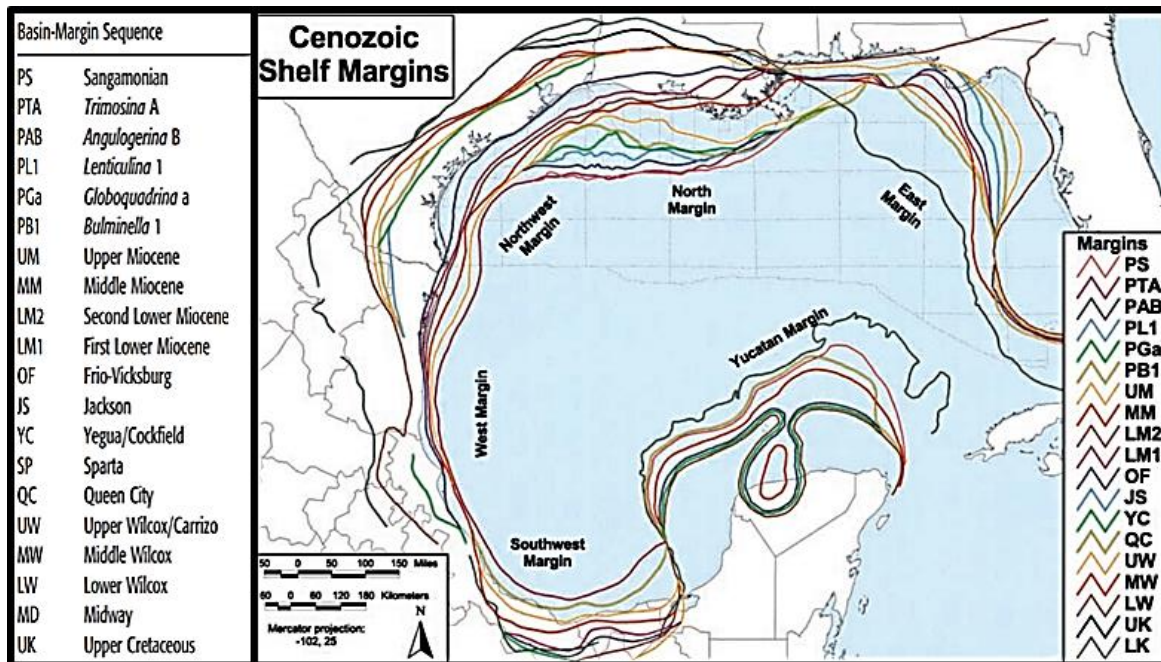


**Figure 7.** Map of the Cenozoic shelf margins at the termination of each basin-margin sequence and depositional episode (from Galloway et al., 2000). The proximity of Cenozoic shelf margins to the BRFS may have some relation to the amount of fault slip that took place during the Cenozoic.

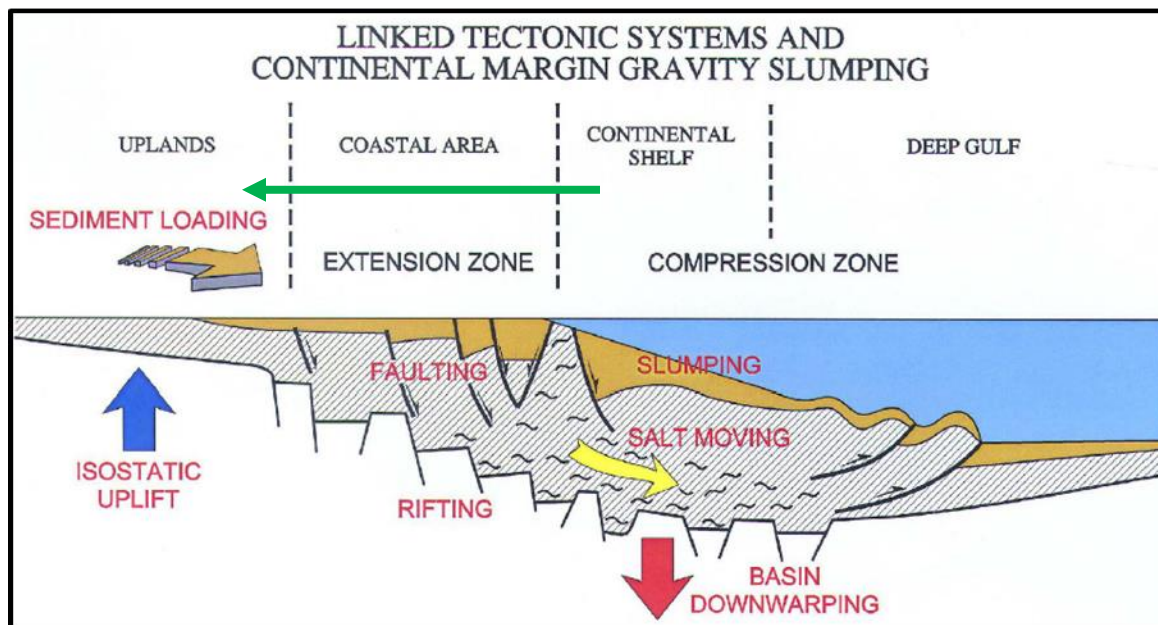


**Figure 8.** Conceptual model, proposed by Galloway et al. (2005), that shows the progradation of the continental margin as sediment loading and isostatic uplift took place. As the Cenozoic shelf margins prograded farther south into the GoM, the “Extension Zone” continued to prograde farther south as well. The green arrow represents a conceptual interpretation of the location of the BRFS during the deposition of the Upper Cretaceous-Sangamonian basin-margin sequences from figs. 6-7. As the proximity of the BRFS to the continental shelf and later the extension zone continued to increase, the BRFS experienced lessening effects of extension and rifting. Thus, the BRFS is subject to isostatic uplift and sediment loading, but lessening effects of extension cause the BRFS to experience less fault slip during the Cenozoic.

## ***2.2 Middle Miocene-Pliocene History and Fault Inactivity***

The middle to late Miocene through the Pliocene is characterized by growth fault quiescence along the north-central GoM (Galloway et al., 2010; McCulloh and Heinrich, 2012). The magnitude of fault quiescence varies across the northern GoM and depends on the proximity of the fault system to relict coast lines. The BRFS, ~100 km (~62 mi) from the GoM coast and ~120 km (~75 mi) away from the modern Mississippi River Delta, had an interval of relative stability or quiescence during the Miocene through Pliocene Epochs (Galloway et al., 2010; Rowan et al., 2000; Hanor, 1982; McCulloh and Heinrich, 2012; Nunn, 1985). The initiation of fault activity of the BRFS, suggested by Shen et al. (2016), occurred during shelf to upper continental slope sedimentation in the Paleocene to late Oligocene, and is marked by stratigraphic thickening of hanging-wall strata relative to footwall strata across segments of BRFS fault planes (Shen et al., 2016; Ocamb, 1961). Inactivity is marked by stratigraphic intervals with no evidence of thickening or an interval with very little stratigraphic offset along the fault detachment surface. Possible causes for growth fault inactivity in the northern GoM have been proposed to be a result of the: 1) reduction in sediment supply that can drive fault motion (Galloway et al., 2011), 2) a reversal of slope of the basal detachment due to sediment-load driven isostatic subsidence (Rowan et al., 2000), or 3) a change in the location of extension as fault systems evolve from the shelf margin to the coastal plain, as Cenozoic outbuilding continued (Winker, 1982).

Kindinger et al. (1997) proposed that the BRFS was activated in the Miocene, and seismic profiles crossing Lake Pontchartrain show offset in strata during the late Pleistocene, thus indicating that fault movement has remained active until at least the late Pleistocene.

Kindinger et al. (1997) did not identify a period of quiescence in segments of the BRFS. Eastern

BRFS segments were compared, by calculated rates of motion of BRFS segments during several Cenozoic, biostratigraphically established chronostratigraphic intervals to address whether a period of quiescence of fault-growth appears to exist in the study area.

### ***2.3 Pleistocene-Holocene Geologic History***

The Plio-Pleistocene is characterized by three allostratigraphic units north of Lake Pontchartrain including the Prairie Terrace, the Intermediate Terrace, and the Upland (High) Terrace (Flocks et al., 2009a; Otvos and Howatt, 1992; Autin et al, 1991; Fisk, 1944; Seed et al., 2006; Lopez et al., 1997; Autin, 1996). However, nomenclature, timing and stratigraphic correlation between units is a subject of controversy (Otvos and Howatt, 1992; Flocks et al., 2009a). The Upland Terrace graviliferous deposits are the oldest and thought to be a product of braided stream systems that occupied the region during the Pliocene (Saucier, 1994; Flocks et al., 2009a). Flocks et al. (2009a) states that this terrace is difficult to date but is thought to span a duration of approximately 1.7 Ma (Saucier, 1994). Timing and duration of formation of the Intermediate Terrace, though poorly constrained, is determined to have been deposited between 1.3 to 0.8 Ma. Kolb et al. (1975) state that the Intermediate complex consists of more than 100 m (~328 ft) of sand and gravel, overlain by oxidized sandy clays. The most recently formed terrace is the Prairie complex, deposited between 120 ka and the last glacial maximum at 18 ka (Autin, 1996; Fisk and McFarlan, 1955; Flocks et al., 2009a).

During the Holocene, steady lake sedimentation and subsidence continued to shape the geomorphology of the study area (Flocks et al, 2009a). Of importance during the Holocene are surface expressions that may be a result of BRFS displacement. McCulloh and Heinrich (2012) found that the BRFS consists of some fault segments with surface expressions, which show

distinctive offset in Quaternary and pre-Quaternary strata. This suggests that they may be or have been active in the Holocene and that the modern surface expressions may be the result of deep subsurface, older Cenozoic growth faults that have been reactivated following extended periods of quiescence (McCulloh and Heinrich, 2012; Gagliano et al., 2003). Extensions of the BRFS including the Madisonville Point Fault, the Causeway Fault, Goose Point Fault and South Point Fault were identified by Lopez and Connor (2001) (Fig. 2).

### **2.3.1 Pleistocene Fault Reactivation and Rates**

An array of previous work has focused on calculating the mean throw rates for the BRFS during the Holocene and Pleistocene epochs and form the foundation for developing an understanding of the geologic history of the BRFS. The rates calculated by these studies are listed in Table 1 and the corresponding study areas are shown in figure 5. Roland et al. (1981) calculated a mean Pleistocene throw rate of  $0.004 \text{ cm yr}^{-1}$  ( $0.0016 \text{ in. yr}^{-1}$ ) on the basis of offset of a Pliocene and Pleistocene stratigraphic contact across the fault. During the Pleistocene, reactivation of the Baton Rouge Fault occurred after a long interval of quiescence likely due to increased sedimentation rates (McCulloh and Heinrich, 2012; Nunn, 1985). Reactivation evidence is present southeast of Denham Springs where the Baton Rouge Fault crosses two, now abandoned, floodplains of the Amite River that were slightly entrenched in the Prairie surface during the last glacial maximum (Nunn, 1985; Durham and Peeples, 1956).

<b>Baton Rouge Fault System Rates</b>					
<b>Name:</b>	<b>Time Period:</b>	<b>Time (ka):</b>	<b>Throw Rate (cm/yr):</b>	<b>Study Authors:</b>	<b>Location:</b>
Study 1	Pleistocene	1800-11.7	0.004	Roland et al, 1981	Baton Rouge, LA
Study 2A	Late Holocene- Present	115 to Present (0)	0.022	Shen et al, 2016	Bennett Road, LA
Study 2B	Last Glacial- Present	32 to Present (0)	0.003	Shen et al, 2016	Paleo-Amite River, LA
Study 2C	Last Interglacial- Present	2.78 to Present (0)	0.007	Shen et al, 2016	Bayou Black, LA
Study 3A	Late Holocene- Present	3.7 to Present (0)	0.02	Yeager et al, 2012	West Middle River, lower Pearl River valley, LA
Study 3B	Late Holocene- Present	1.3 to Present (0)	0.12	Yeager et al, 2012	West Middle River, lower Pearl River valley, LA
Study 4	Late Holocene-Present	0.03 to Present (0)	0.25	Lopez, 1991	Highway 11 Bridge, LA
Study 5A	Late Holocene-Present	0.02 to Present (0)	0.8-1.0	Lopez et al, 1997	Norfolk Southern Railroad, LA
Study 5B	Post-Miocene to Present	5300 to Present (0)	0.0003	Lopez et al, 1997	Norfolk Southern Railroad, LA

**Table 1.** Previous studies of the Baton Rouge Fault System have yielded throw rates at different locations and for different time intervals. This table lists each study conducted, the time period represented by the calculated throw rate, the throw rate calculated in each study, the authors of the study, and the location where each study was conducted.

### 2.3.2 Pleistocene-Holocene Contact

Depth to the Pleistocene-Holocene contact has been investigated by several studies (Flocks et al., 2009a; Heinrich et al., 2015; United States Army Corps of Engineers, 1994; Kulp et al., 2002; Roth, 1999). A knowledge of the depth of the Pleistocene-Holocene contact is important during the process of interpreting shallow seismic data. Noticeable offset in the Pleistocene-Holocene contact may be evidence of fault slip during the Holocene. For the purposes of this study, the average depth subsea of the Pleistocene-Holocene contact in Lake Pontchartrain is 3-4 m (10-12 ft) derived from cross-sections(Fig. 9), by Dunbar et al. (1994) with data from Charbreck et al. (1988), Kolb et al. (1975), and Snead et al. (1984) (Figs. 10-11). These cross-sections were constructed using a few hundred out of the ~730 borings collected by the United States Army Corps of Engineers (USACE) and analyzed by Dunbar et al. (1994). Dunbar et al. (1994) also created a series of cross-sections in the Rigolets along with a map of their locations shown in figures 12-14. A cross section of the study area of this project was also created showing Pleistocene and Holocene boundaries (Fig. 15) (Flocks et al., 2009a). Roth (1999) contoured depth to the top of the Pleistocene surface (Fig. 16) and the Holocene thicknesses (Fig. 17) from shallow, high resolution seismic data and boring logs collected by Dunbar et al. (1994). These contours and cross-sections are used to estimate depth to the Pleistocene-Holocene contact in shallow seismic data and assess if displacement due reactivation of the BRFS in the Pleistocene remains constant into the Holocene strata by providing mappable horizons in the shallow seismic.

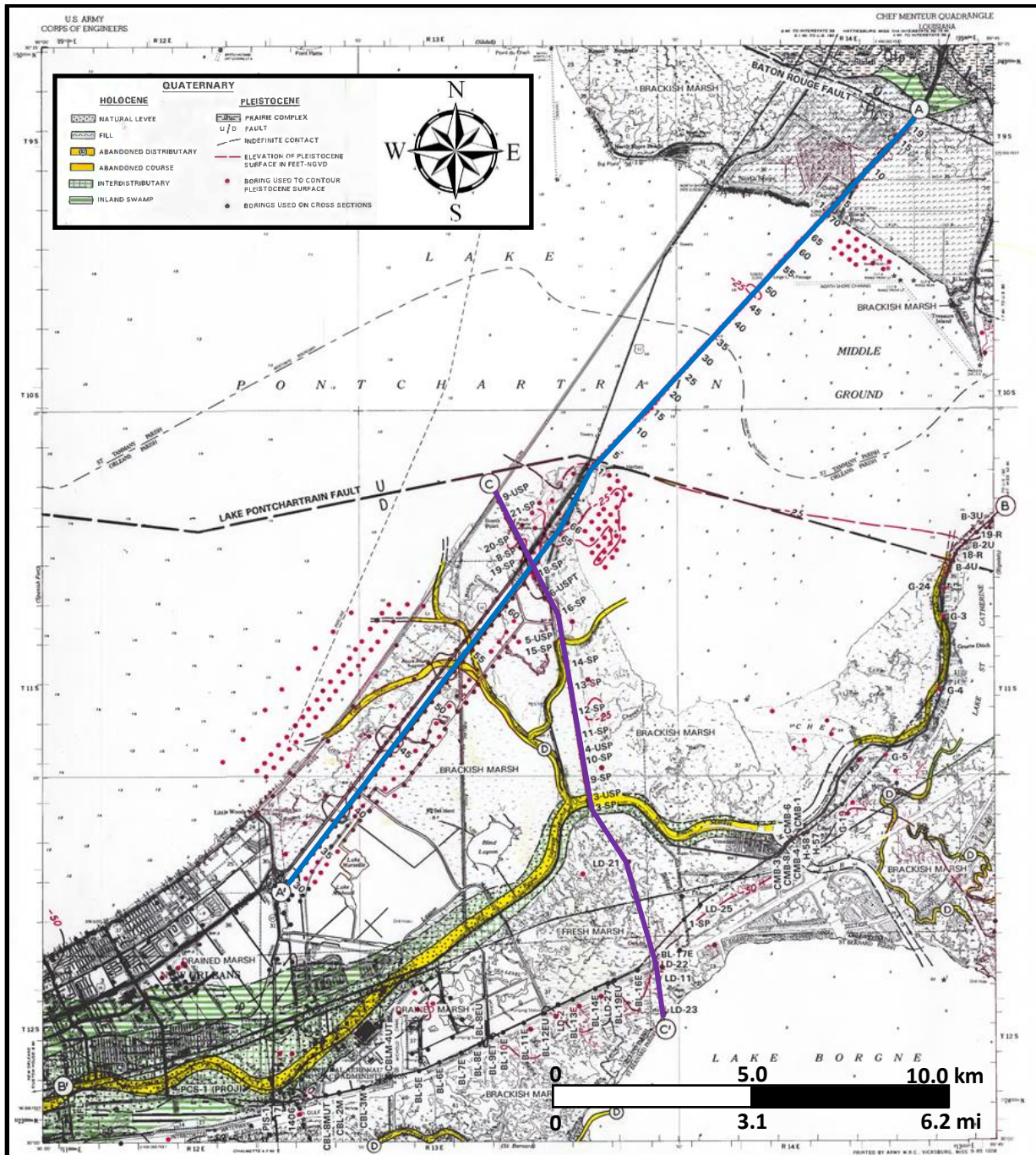


**Figure 9.** Cross-sections and contours were created using boring logs (red dots on map) collected and analyzed by Dunbar et al. (1994). Marsh environments and delineated marsh boundaries were mapped by Dunbar et al. (1994) using infrared photography and a vegetation map created by Chabreck and Linscombe (1988). Faults were mapped using information from Kolb et al. (1975) and Snead et al. (1984). In this study cross-sections A-A' (blue line) and C-C' (purple line) were used to identify the subsurface geology from collected vibracores in Lake Pontchartrain.

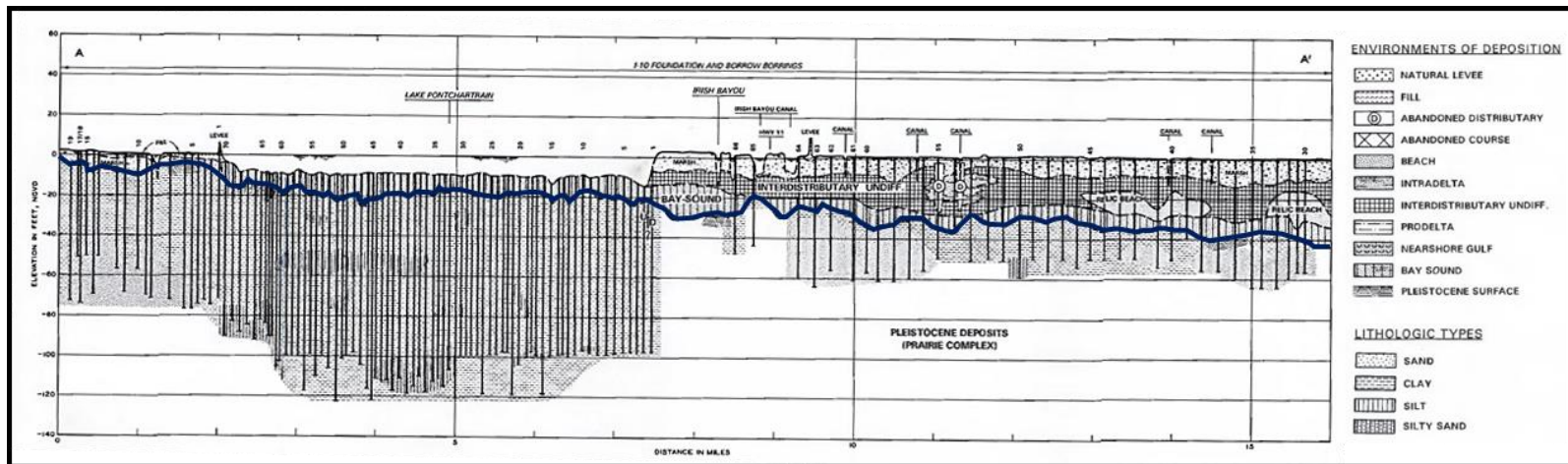


**Figure 10.** Cross-section A-A' Holocene and Pleistocene stratigraphic units showing the stratigraphic location of the contact, environments of deposition, and lithologies used to describe collected vibracores (modified from Dunbar et al., 1994). The Pleistocene-Holocene contact is shown as the dark blue line. The depth to the Pleistocene-Holocene contact was used along with contours by Roth (1999) to estimate the depth to the contact in Chirp seismic.

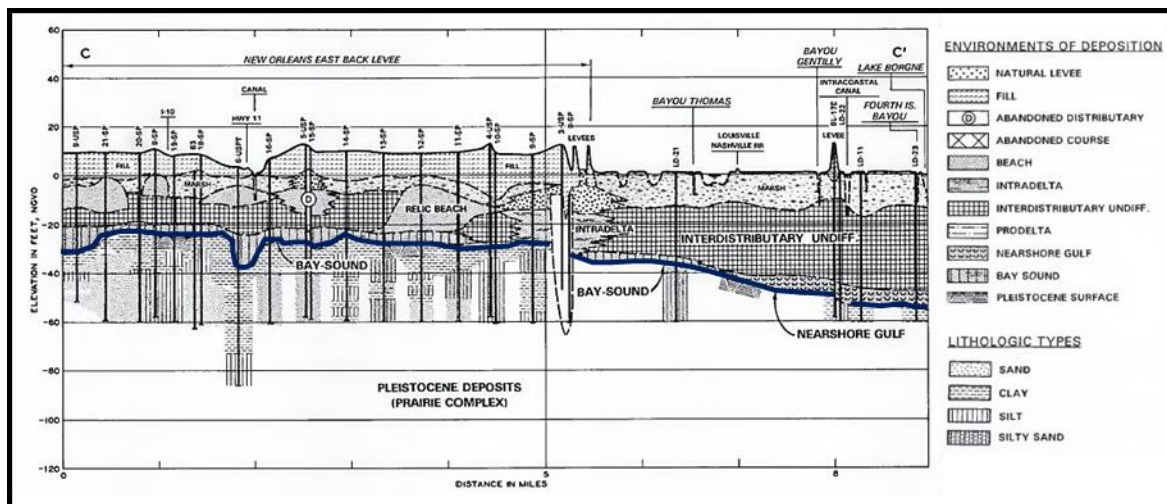


**Figure 11.** Cross-section C-C' Holocene and Pleistocene stratigraphic units showing the stratigraphic location of the contact, environments of deposition, and lithologies used to describe collected vibracores (modified from Dunbar et al., 1994). The Pleistocene-Holocene contact is shown as the dark blue line. The depth to the Pleistocene-Holocene contact was used along with contours by Roth (1999) to estimate the depth to the contact in Chirp seismic.

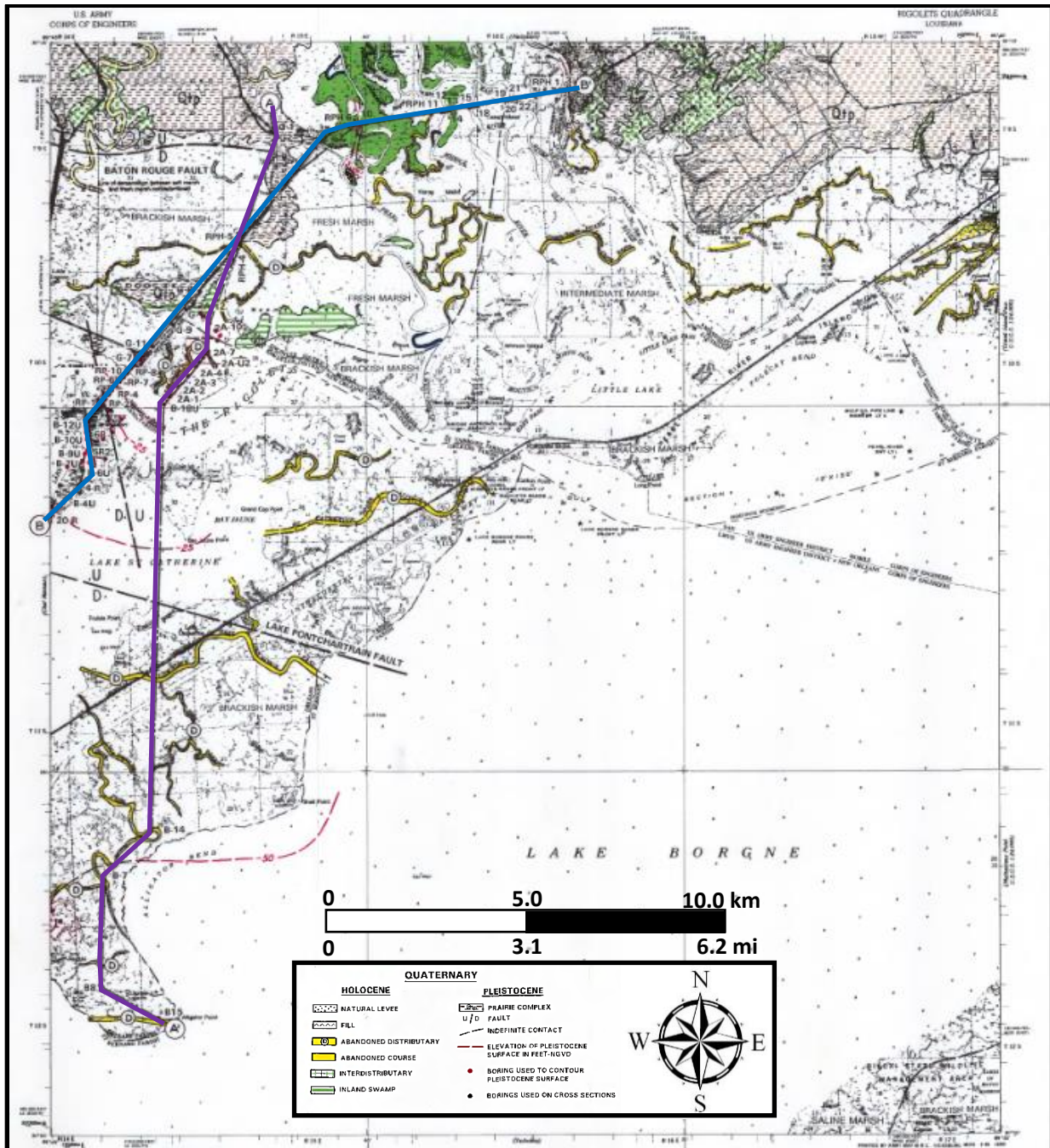


**Figure 12.** Cross-sections and contours were created using boring logs (red dots on map) collected and analyzed by Dunbar et al. (1994). Marsh environments and delineated marsh boundaries were mapped by Dunbar et al. (1994) using infrared photography and a vegetation map created by Chabreck and Linscombe (1988). Faults were mapped using information from Kolb et al. (1975) and Snead et al. (1984). In this study cross-sections A-A' (blue line) and B-B' (purple line) were used to identify the subsurface geology from collected vibracores in Lake St. Catherine and Lake Borgne.

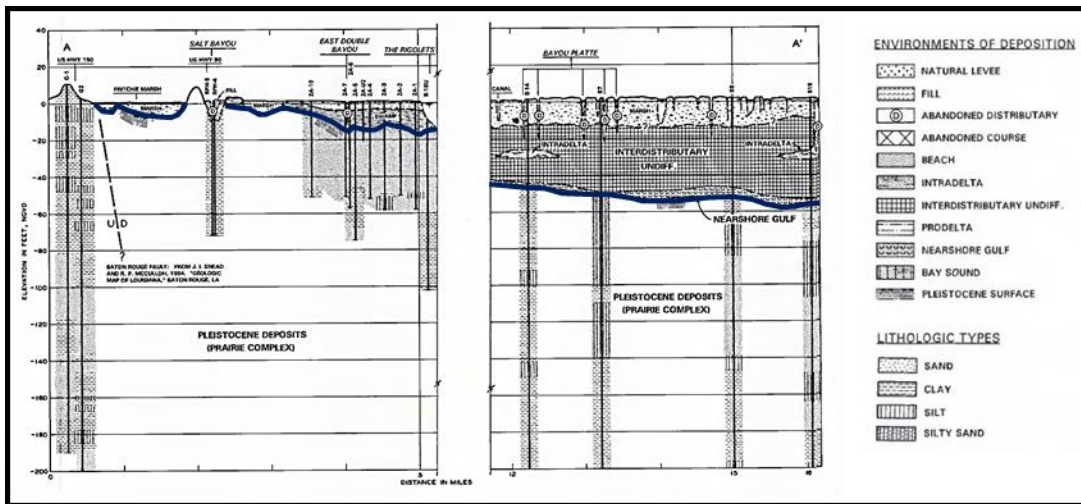


**Figure 13.** Cross-Section A-A' of Holocene and Pleistocene stratigraphic units showing the Pleistocene-Holocene contact depth, environments of deposition, and lithologies within vibracores (modified from Dunbar et al., 1994). The Pleistocene-Holocene contact is shown as the dark blue line.

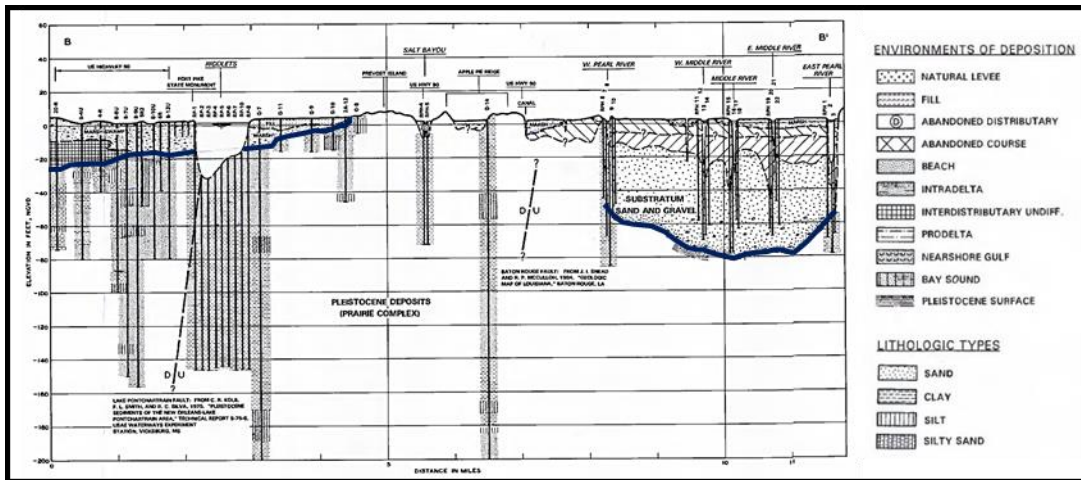


**Figure 14.** Cross-Section B-B' of Holocene and Pleistocene stratigraphic units showing the Pleistocene-Holocene contact depth, environments of deposition, and lithologies within vibracores (modified from Dunbar et al., 1994). The Pleistocene-Holocene contact is shown as the dark blue line.

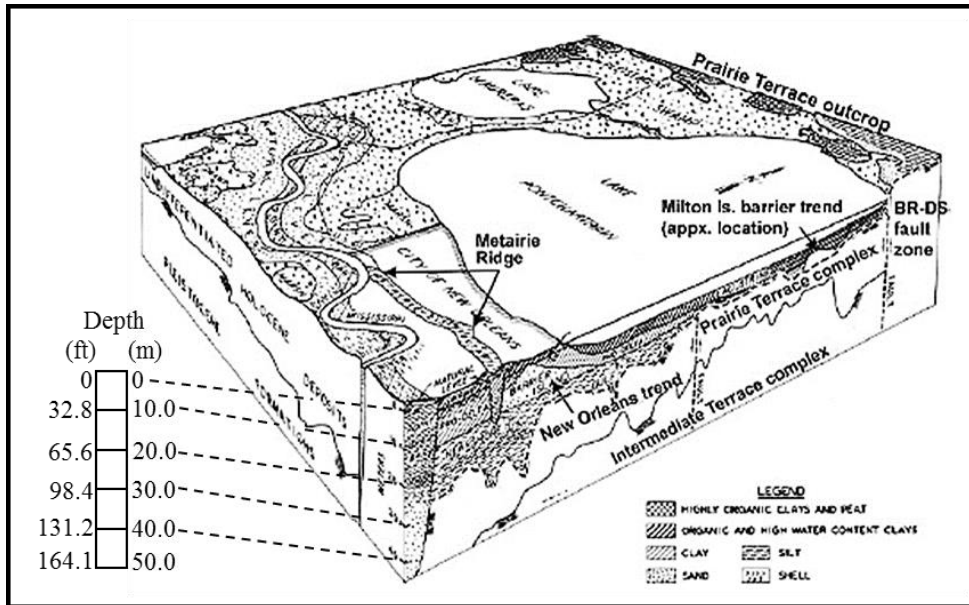


**Figure 15.** Cross-section of Lake Pontchartrain showing the Pleistocene-Holocene contact, the Prairie Terrace complex (Pleistocene age), and the Intermediate Terrace complex (Pleistocene age) (modified from Kolb et al. (1982), Seed et al. (2006), and Flocks et al. (2009a)). It also shows the location of two faults including a segment of the Baton Rouge-Denham Springs Fault Zone and a fault located near central Lake Pontchartrain (the Lake Pontchartrain Fault in this study).

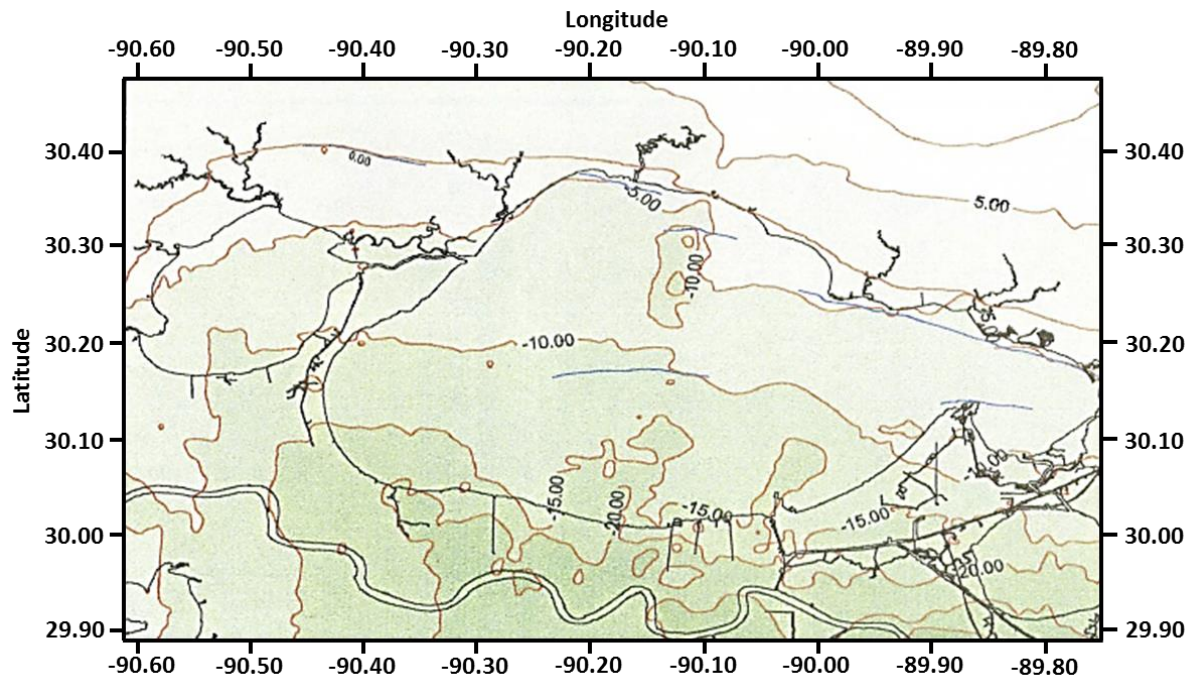


**Figure 16.** Structural contours on the top of the Pleistocene stratigraphy in meters below mean sea level (from Roth, 1999). Note the general south directed increase in depth on the top of the Pleistocene surface. These contours are used to identify the upper Pleistocene reflector in Chirp seismic collected in this study.

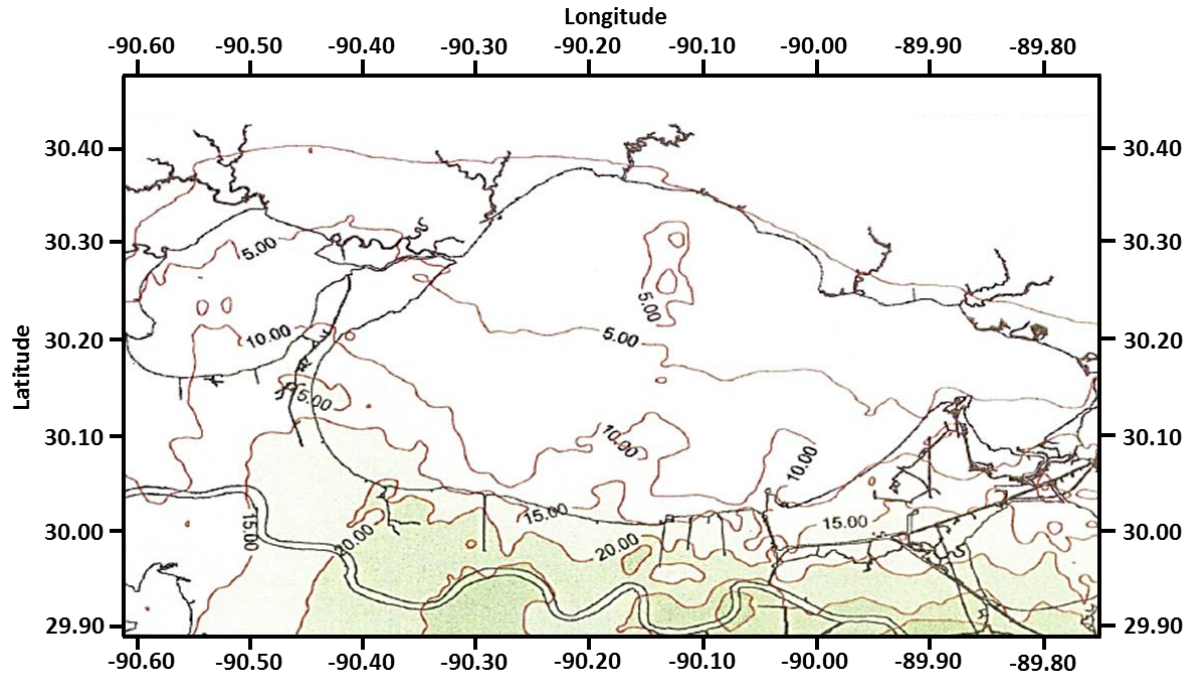


**Figure 17.** Isopach contours of the Holocene strata in 5 m intervals (from Roth, 1999). Thickness of Holocene strata helped accurate identification of the top of the Pleistocene surface in Chirp seismic. Holocene thickness increases southward.

### 2.3.3 Holocene Fault Activity and Displacement Rates

Recent studies have been completed that quantify Holocene displacement rates of the BRFS and relate newly discovered fault segments to the BRFS. The rates listed in these studies as well as the corresponding study areas are shown in figure 5 and Table 1. Shen et al. (2016) calculated mean throw rates during time scales spanning the last interglacial to the late Holocene using optically stimulated luminescence dating. The Shen et al. (2016) methodology yielded a mean throw rate of  $0.022 \text{ cm yr}^{-1}$  ( $0.009 \text{ in yr}^{-1}$ ) during the late Holocene,  $0.003 \text{ cm yr}^{-1}$  ( $0.0012 \text{ in yr}^{-1}$ ) during the last glacial, and at least  $0.007 \text{ cm yr}^{-1}$  ( $0.0028 \text{ in yr}^{-1}$ ) during the last interglacial for the BRFS. The time frame of each of these intervals is shown Table 1. Yeager et al. (2012) reported late Holocene throw rates of  $0.02\text{-}0.12 \text{ cm yr}^{-1}$  ( $0.008\text{-}0.047 \text{ in yr}^{-1}$ ) using lithostratigraphy, radiochemistry, radiocarbon dating and biostratigraphy of six cores from across a suspected fault segment of the BRFS in the West Middle Pearl River. Lopez (1991) reported

fault slip rates of a segment of the BRFS South Point Fault, of  $0.25 \text{ cm yr}^{-1}$  ( $0.1 \text{ in yr}^{-1}$ ) using high-resolution seismic data that imaged post late Pleistocene stratigraphy in combination with observations of deformation in the Highway 11, Interstate 10, and West Causeway Bridges along the fault traces shown in figure 2. Lopez et al. (1997) used high-resolution seismic and observations of the Norfolk-Southern Railroad bridge to calculate a rate of  $0.8\text{-}1.0 \text{ cm yr}^{-1}$  ( $0.3\text{-}0.4 \text{ in yr}^{-1}$ ) since the late Pleistocene as well.

### **2.3.4 Subsidence**

Existing rates, however, do not differentiate between rates of offset for different time intervals of measurement and differential subsidence across faults. Mechanisms of subsidence across coastal Louisiana has been separated by some into six different categories: 1) tectonics, including fault motion and halokinesis, 2) sediment compaction, 3) sediment loading, 4) glacial isostatic adjustment, 5) fluid withdrawal, and 6) surface water drainage and management (Yuill et al., 2009; Dokka, 2006). Subsidence, therefore, can be amplified in regions associated with active faulting. Dokka (2006) stated that releveling surveys measure nearly 12 cm of subsidence between 1969 and 1971 on the down-thrown side of the Michoud fault located east of New Orleans. In addition, between 1977 and 1995 the same locale subsided at  $2.0 \text{ cm yr}^{-1}$  ( $0.79 \text{ in yr}^{-1}$ ), whereas 5.0 km (3.1 mi) from the fault on either side the subsidence rates were closer to  $1.5 \text{ cm yr}^{-1}$  ( $0.59 \text{ in yr}^{-1}$ ). Thus, the amount of displacement observed in high-resolution, shallow seismic may be higher than the amount of displacement calculated at greater depths from 2-D/3-D seismic because of ongoing regional subsidence at the surface.

## ***2.4 Geologic History of the Pontchartrain Basin***

Since the Late Jurassic, basin subsidence, salt deformation, and development of growth faults around the periphery of sedimentary depocenters has occurred, especially during the Tertiary (Salvador, 1987). This includes the formation of deep-seated growth faults of the BRFS and Lake Borgne Fault System (LBFS) within the Pontchartrain Basin. Cenozoic strata also record the episodic progradation of clastic fronts building southward, supplied by sediment sourced from the Laramide and Appalachian uplifts (Bentley et al., 2015). Blum et al. (2014) collected detrital zircons (DZ) from several regions of the GoM coastal plain and suggest that during the Late Cretaceous sediment was sourced from only the southern United States and the Appalachian-Ouachita orogen. However, by the Paleocene, southern North America from the Western Cordillera to the Appalachian Mountains supplied sediment to the GoM. Blum et al. (2014) state that the assembly of the Mesozoic Western Cordillera resulted in west-derived rivers in the United States and likely includes an ancestral Mississippi River in the Mississippi embayment that continues to supply sediment to the GoM.

A series of three weathered, south-dipping Plio-Pleistocene terraces occupies the northern Pontchartrain Basin, whereas the Mississippi River delta plain forms the southern boundary (Flocks et al., 2009b). Holocene deltaic progradation, regional subsidence, and barrier-island formation (the Pine Island Barrier Trend locally) during sea-level regressions are the fundamental processes that have shaped the modern Pontchartrain Basin (Flocks et al., 2009b; Lopez et al., 1997). The terraces of the northern Pontchartrain Basin consist of a complex arrangement of fluvial and marine facies resulting from phases of sedimentation associated with contemporaneous glacial cycles (Autin et al., 1991; Kolb, Smith, and Silva, 1975; Otvos and Howatt, 1991). In this study area, the BRFS is the physiographic boundary between the Plio-

Pleistocene terraces characteristic of the northern Pontchartrain Basin and the Holocene sediment deposits of the Mississippi River Delta.

## ***2.5 Formation of Lake Pontchartrain and Lake Borgne***

This physiographic separation and resulting geologic variability formed by activity of the BRFS is evident in a geologic map of the Pontchartrain Basin (Fig. 1). Flooding of the southern Pontchartrain Basin formed an embayment that extended west at a longitude equivalent with modern Baton Rouge, closely following the BRFS located along the northern margin of the lakes (Fisk, 1947; Saucier, 1963). The Prairie Formation, an alloformation of the three Pleistocene terraces at the northern boundary of Lake Pontchartrain, is an example of this physiographic separation. Subsidence along the fault trend, where the Prairie Formation dropped to below present sea level, is proposed by Lopez (1991) to have formed Lakes Maurepas, Pontchartrain, and Borgne. As sea level rose and the Mississippi River Delta began to prograde to the southeast, shallow-marine and fluvial sediments were deposited on the late Pleistocene low-stand, oxidized ravinement surface (Saucier, 1994). Flocks et al. (2009a) proposed a conceptual model for the formation of Lake Pontchartrain (Fig. 18). This conceptual model includes the physiographic separation and resulting geologic variability formed as a result of BRFS activity.

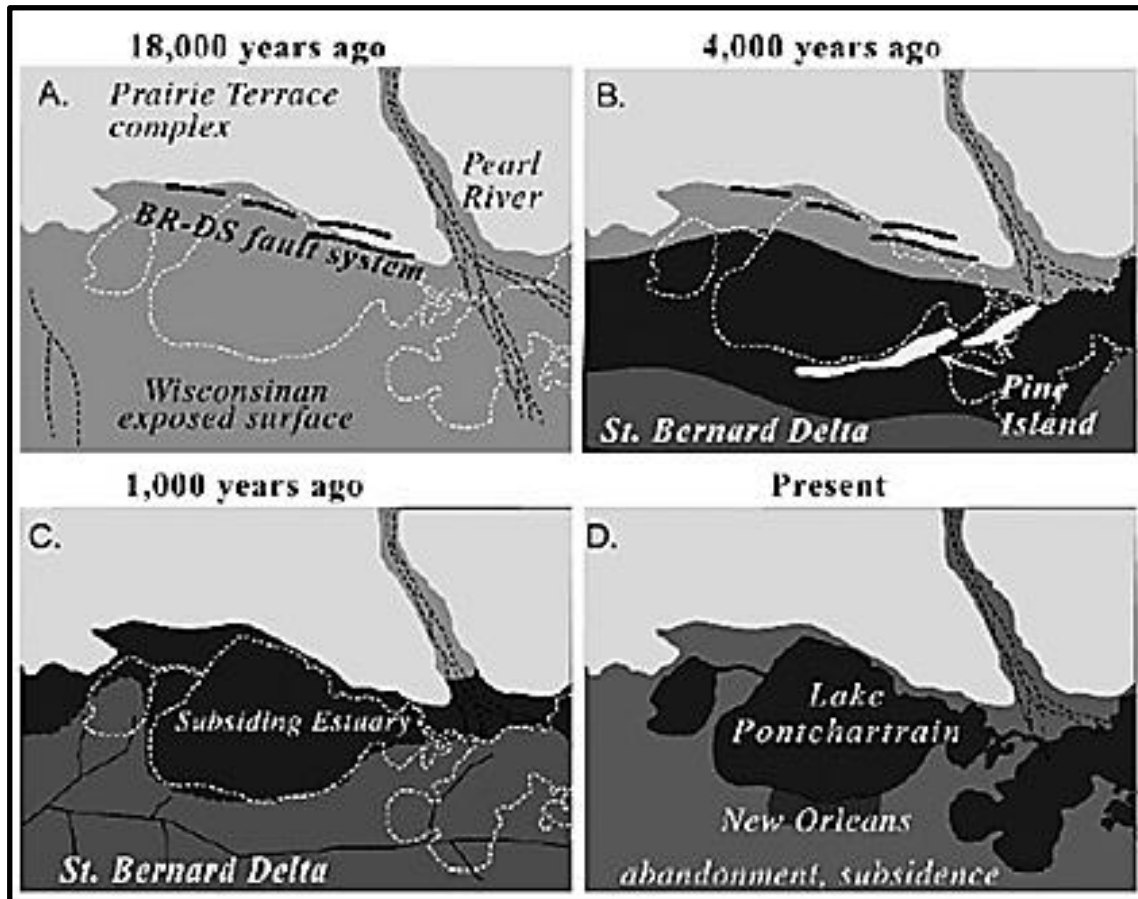


**Figure 18.** Flocks et al. (2009) proposed a 4-stage model for the formation of Lake Pontchartrain and the surrounding areas as depicted in this figure. Sea-level low-stand at the end of the Pleistocene exposed the Prairie Terrace complex at 18 ka. During a Holocene transgression, the Pine Island barrier trend formed by longshore transport ending about 4 ka. The third phase occurred as the St. Bernard Delta complex prograded across the Pontchartrain Basin from the west and buried the Pine Island barrier trend at approximately 1 ka, effectively closing the Lake Pontchartrain estuary from the GoM. The final phase of evolution includes subsidence and shoreline erosion that continue to shape the estuary and expand open waters today.

## **Chapter 3. Methodology**

### **3.1 *LDNR Well Log Data***

In order to characterize pre-Holocene stratigraphic relationships and to aid in the mapping of faults a total of 145 deep well logs were acquired from the Louisiana SONRIS database (Fig. 19). The deepest log penetrated to a depth of ~7,800 m (~25,600 ft) and the shallowest interval logged was ~2,350 m (~7,710 ft). Logging techniques primarily were spontaneous potential (SP) but locally other logs such as gamma ray, and resistivity were available. Each well log was examined to identify the primary lithologic units penetrated and tied to other wells to provide an understanding of the study area subsurface lithostratigraphic framework. Moreover, Paleo Data Inc. provided biostratigraphic data for 31 of the wells to define key biostratigraphic markers and provide chronologic control (Fig. 20).

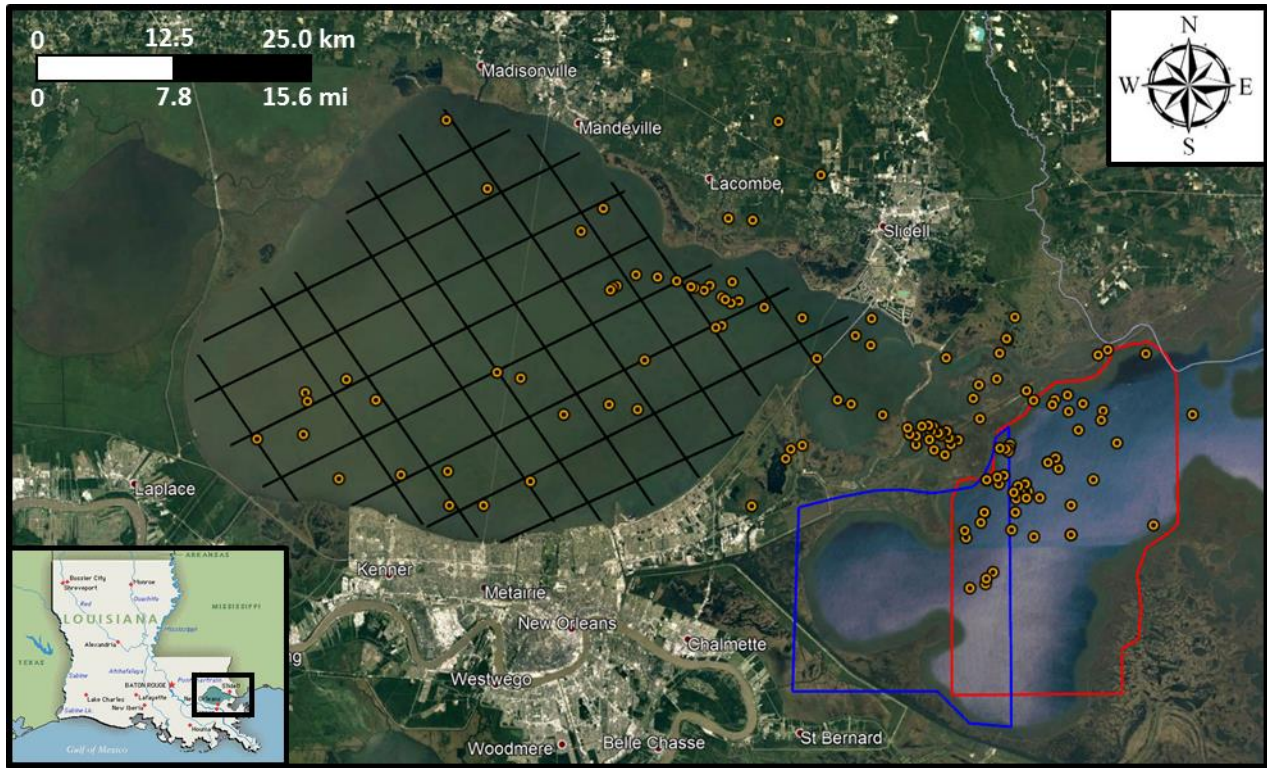


**Figure 19.** Map showing 145 well log locations collected from the SONRIS online database provided by the Louisiana Department of Natural Resources as well as seismic datasets used in this study. The black lines mark the positions of 18, 2-D seismic lines from Lake Pontchartrain, the blue polygon is the extent of the 3-D western Lake Borgne seismic survey, and the red line is the extent of the 3-D eastern Lake Borgne seismic survey. The well log identifiers were sent to Paleo Data Inc., which helped identify biostratigraphic data for 31 of the available well logs.



**Figure 20.** Maps showing the 31 well logs with available biostratigraphy data. The biostratigraphy data was donated by Paleo Data Inc. (2018). Purple arrows point to the two well logs with available velocity survey data (one in Lake Pontchartrain and one in Lake Borgne), provided by Velocity Databank (2019). Three cross-sections (white lines labeled with white numbers) were made from the well logs with available biostratigraphy to correlate chronostratigraphic intervals from ~1,219 m (4,000 ft) to ~4,572 m (~15,000 ft) in depth. These cross-sections are significant to determine if there is offset caused by fault slip, expansion caused by growth faulting, and relate the chronostratigraphy to seismic interpretations.

## **3.2 Integration of Seismic: Lake Borgne 3-D and Lake Pontchartrain 2-D Data**

Three seismic datasets were donated by WesternGeco for this study (Fig. 19). The Lake Pontchartrain dataset consists of 18, 2-D seismic lines that cover the entirety of Lake Pontchartrain for a total distance of 614 km (382 mi). The seismic data was collected in 1985 by WesternGeco using a *DigiSeis* airgun. The Lake Borgne data set consists of 2, 3-D seismic surveys collected by WesternGeco. One survey covers part of west Lake Borgne 367 km<sup>2</sup> (142 mi<sup>2</sup>), whereas the other covers 492 km<sup>2</sup> (190 mi<sup>2</sup>) of east Lake Borgne. The Lake Pontchartrain 2-D survey and the Lake Borgne western 3-D survey extend to a two-way travel time (twt) of 6 s, whereas the Lake Borgne eastern survey is clipped at 1.5 s twt.

### **3.2.1 Seismic Analysis**

Analysis of the three seismic data sets was undertaken in *IHS Kingdom* software. The data was loaded into the software using the following steps: create a new project, import the SEG-Y seismic data, load the wells, import time-depth charts, and create any well deviation surveys if necessary. Seismic analysis began with picking horizons (strata) that represent bold reflections in the data. The American standard defines reflections including a black peak as a hard or positive event, and a white trough as a soft or negative event (Avseth et al., 2010). On a near-offset stack section, a hard event will correspond to an increase in acoustic impedance with depth, whereas a soft event will correspond to a decrease in acoustic impedance with depth (Avseth et al., 2010). Seismic amplitudes, primarily representing contrasts in elastic properties between individual layers, contain information about lithology, porosity, pore-fluid type and saturation, as well as pore pressure (Avseth et al., 2010).

The boldest reflections, seismic soft or hard events, were used to map a layer (stratum) throughout a 2-D or 3-D dataset. Vertical offset visible as a break in the reflector typically

identifies the presence of a fault, unless there are noticeably visible “seismic footprints” that generally indicate acquisition issues. *IHS Kingdom* allows faults to be picked in the same procedure as picking reflections. After the faults are picked, *IHS Kingdom* depicts the resulting fault traces on a base map by displaying picked faults on the base map. This serves as quality control because if the fault abruptly splits or changes strike it is likely mapped incorrectly.

2-D seismic data in Lake Pontchartrain does not reliably image subsurface strata between 0 and approximately 0.25 s twt. Therefore, surface traces of faults were estimated by projecting faults to the surface at constant dip rates on seismic lines where faults were well defined deeper than approximately 0.25 s twt. These fault segments were exported to form a map of surface fault traces (Fig. 21). Estimates of error in measurements or possible changes in dip angle are represented by calculations in Table 2. In order to quantify rates of fault displacement, age-dated horizons were picked in the deep seismic data as well.

Fault Dip Angle Estimates from 2D Seismic				
Fault Name	TVD of Lowest Point Along Fault Surface (ft)	Distance Between Lowest Point and Projected Surface Trace (ft)	Dip Angle Estimate (°)	Distance Between Estimates (ft)
Lake Pontchartrain	10176	5280	61	N/A
Lake Pontchartrain	10176	6516	56	1236
Lake Pontchartrain	10176	4301	66	979
Goose Point	9660	3960	69	N/A
Goose Point	9660	4963	64	1003
Goose Point	9660	2918	74	1042

**Table 2.** The fault segments that were mapped in the 2-D seismic dataset in Lake Pontchartrain include the Lake Pontchartrain Fault and the Goose Point Fault. Listed are data for 3 separate traverses across the Lake Pontchartrain fault and 3 across the Goose Point fault. On each traverse the fault is characterized by, 1) deepest reliable identification of fault on 2-D seismic, 2) horizontal distance between the deepest interpreted fault and its estimated surface trace, 3) dip of the fault plane, and 4) lateral uncertainty of the surface trace of the fault using +/- 5 degree change in fault dip from its shallowest interpreted position on 2-D seismic. Distance values must be positive, so the absolute value of the result was input into the final column. Not Applicable (N/A) was assigned to the original fault pick in 2-D seismic in the final column.

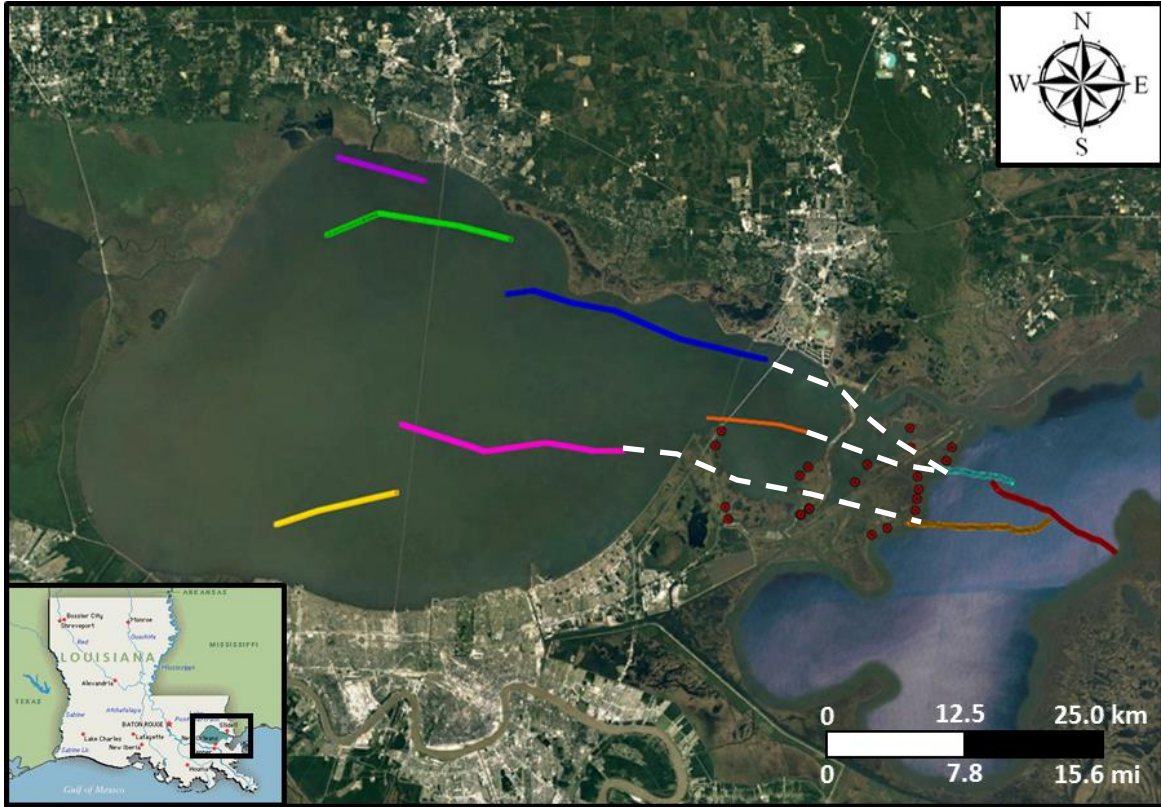


**Figure 21.** Map of the study area showing the surface projected fault traces from available data and literature. The dark orange fault in Lake Pontchartrain was mapped by Lopez et al. (1998). The light blue, red, and light orange surface fault traces in Lake Borgne were projected up to the surface using the eastern Lake Borgne 3-D survey. The purple, light green, blue, pink, and yellow labeled faults were projected to the surface using the 2-D seismic lines in Lake Pontchartrain. The white dashed lines indicate possible surface traces of the fault segments that may show lateral continuity beneath the EOLB. The vibracore locations (red circles) were positioned to attempt to collect two vibracores on each side of the projected surface fault traces.

### 3.2.2 Biostratigraphic Tie to Seismic

Horizons were age-constrained by tying biostratigraphic markers to seismic data. This process began with loading the well logs with available biostratigraphy into *IHS Kingdom*. Then, the well logs were depth-converted into seismic so that each horizon matched with the biostratigraphy listed at that interval as well as to confirm the biostratigraphy data was properly picked in the seismic. Depth-conversion was completed by well to seismic tie in two different ways: 1) creating a seismic synthetic and 2) importing a velocity survey for a known well log. In the Lake Pontchartrain 2-D data, a velocity survey, provided by Velocity Databank Inc., was imported to depth convert the well logs (Fig. 22). A seismic synthetic, however, was created for

the Lake Borgne 3-D surveys (Fig. 23). Frequency histograms were also created for both Lake Borgne 3-D surveys as well as the Lake Pontchartrain 2-D line, WGLP 85-15, at two intervals (Fig. 24).

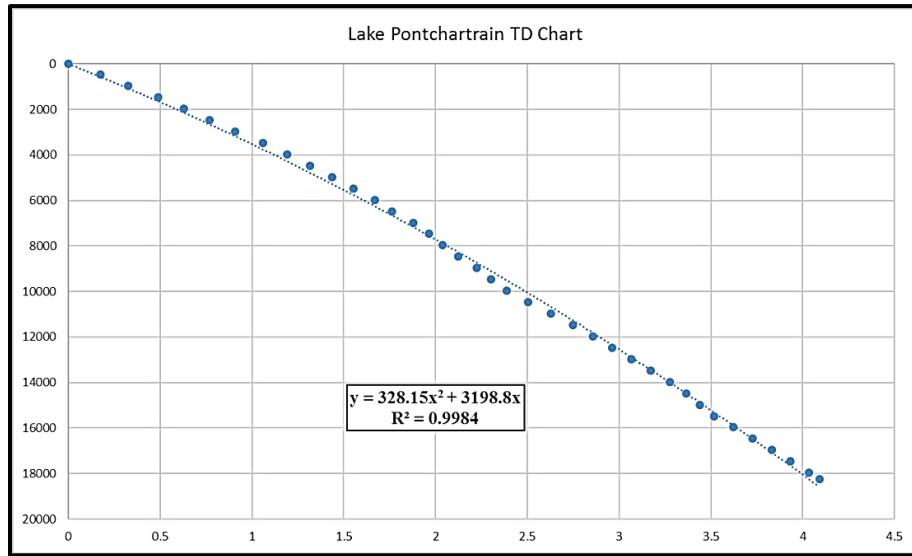


**Figure 22.** Time-depth curve calculated from a check-shot velocity survey provided by Velocity Databank Inc. for use in this study. The check-shot data was collected from Well #1 Block 7 (API: 171032002000) labeled as Well #157558 in figure 20. This time-depth chart was used in *IHS Kingdom* to depth convert the well logs located in Lake Pontchartrain with available biostratigraphy data.

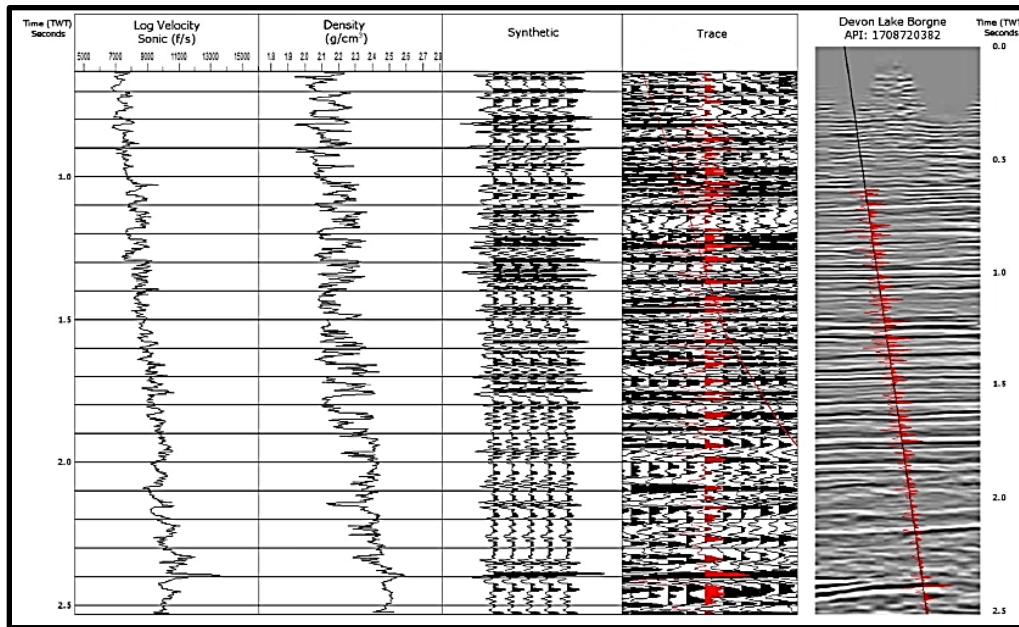


**Figure 23.** A synthetic seismogram was created using sonic and density well log inputs from a Devon Energy Well (Well# 132621 in figure 20). The trace section shows the synthetic trace overlain with the actual seismic trace. The resulting synthetic ties well with the seismic amplitudes on the right side of the figure (from Frank, 2016).

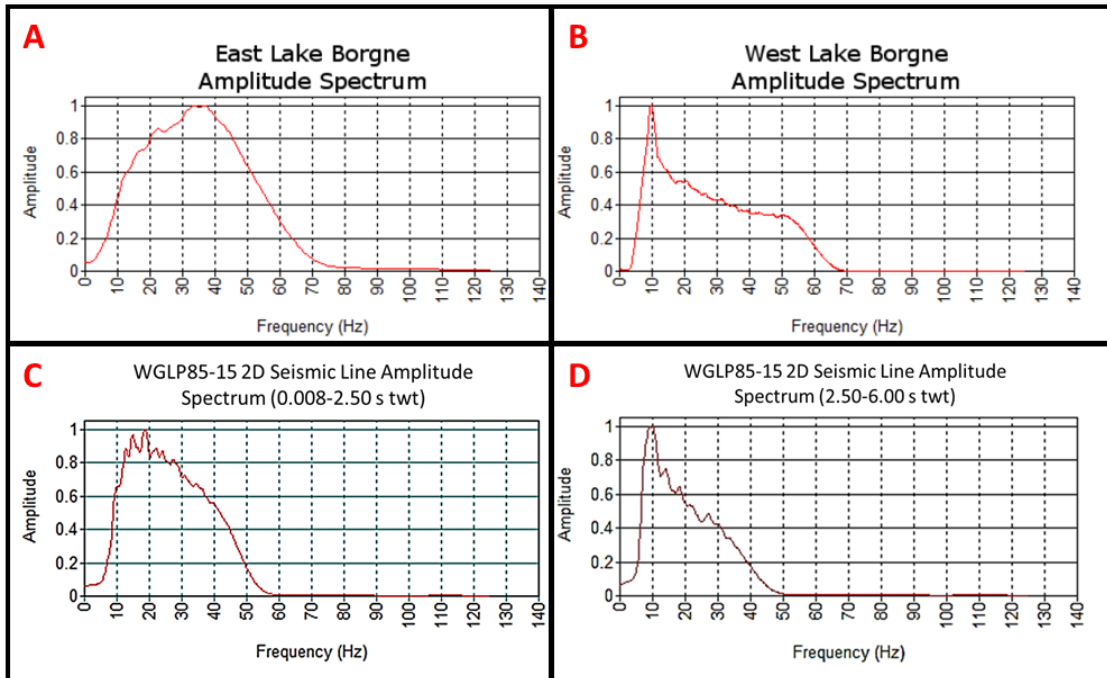


**Figure 24.** Plots of amplitude survey spectrums generated in *IHS Kingdom* for (A) the eastern Lake Borgne 3-D survey (from Frank, 2016), (B) the western Lake Borgne 3-D survey (from Frank, 2016), (C) WesternGeco Lake Pontchartrain (WGLP) 2-D line 85-15 from 0.008 to 2.500 s twt, and (D) WGLP 2-D line 85-15 from 2.500 to 6.000 s twt. The dominant frequency corresponds to the highest peak amplitude value. The dominant frequencies of these surveys are 35 Hz, 10 Hz, 19 Hz, and 10 Hz, respectively.

Structure maps are another useful tool to assess the accuracy of fault and biostratigraphy picks in *IHS Kingdom*. A top depth structure map of the biostratigraphic marker *Heterostegina SP* was created from the Lake Pontchartrain 2-D seismic dataset using available identified *Heterostegina SP* picks from the 31 well logs. The picks were depth-converted to true vertical depth (TVD) in ft onto the seismic using a velocity survey (Fig. 20). The bold reflection closest to the *Heterostegina SP* marker was picked in each of the 2-D lines and then a grid was made across Lake Pontchartrain. Abrupt changes in depth that are noticeably higher than regional dip indicate fault slip. In a 3-D dataset there are many more seismic traces, so it is useful to grid the data in cell sizes of 25 traces or so in order to create structure maps. A seismic synthetic was used to build twt structure maps in the 3-D datasets (Fig. 23). Biostratigraphic picks were also depth-converted using a velocity survey in Lake Borgne (located in figure 20) to build depth

structure maps in the 3-D datasets. Therefore, 3-D depth structure maps and twt structure maps were built to assess the accuracy of mapped faults in IHS Kingdom.

Shallow horizons above ~1,219 m (~4,000 ft) were also picked using estimations of biostratigraphic horizons. Due to the lack of available shallow biostratigraphy in the 2-D dataset, shallow horizons above the *Robulus L* pick were estimated. Galloway et al. (2000) state that bounding marine shale sequences contain biostratigraphic foraminifera along the northern coast of the GoM. These marine shales would appear as a bold reflection in the seismic data. Therefore, with the assumption of a steady accumulation rate, intervals were estimated by splitting the sediment deposited above the *Robulus L* horizon in true vertical depth and two-way-time into the intervals predicted by Galloway et al. (2000) using the age of the correlated biostratigraphic foraminifera. A bold reflection that may be mapped within 0.2 s twt of the estimates made from the Galloway (2000) predictions was mapped as a potential shallow biostratigraphic marker and was used in order to generate graphs of offset during each time period.

### **3.2.3 Fault Displacement Rates**

After the biostratigraphic markers were picked, displacement rates were calculated by measuring the offset in twt between the up-thrown and down-thrown depth of each biostratigraphic horizon, converting the offset from twt to feet, and dividing the result by the age of the biostratigraphic foraminifera. Expansion indices were then calculated by dividing the thickness of sediment accumulation on the down-thrown side of the fault between two biostratigraphic markers by the amount of sediment accumulation on the up-thrown side between the same two biostratigraphic markers. The duration of time elapsed in this period of sediment accumulation was compared to the expansion indices that occurred during that period. Rate of

offset for time increments was calculated by measuring the fault offset (in twt) of two biostratigraphic horizons (up-thrown subtracted from down-thrown for each pick) and dividing this value by the elapsed time between the two horizons. This was used to estimate a rate of offset caused by the fault during a defined interval of time. These analyses of the industry seismic datasets provide insight into the following: possible timing for the initiation of the faults, possible surface traces of the applicable BRFS and LBFS segments from picked faults (with estimates of error), displacement rates of known biostratigraphic horizons, identification of fault quiescence periods (if any), and lateral continuity between identified faults.

### ***3.3 BasinMod Burial History Diagrams***

An important part of this project is to understand the timing of activation of Baton Rouge Fault System displacement in order to better understand the geologic history of the BRFS. *BasinMod* is software that uses biostratigraphy data from well logs to create a model of the burial history for a defined basin. Flocks et al. (2009a) state that geologic processes that formed the Pontchartrain Basin began approximately 60 Ma. Therefore, burial history plots were created using wells which penetrated horizons as old as 69 Ma, one burial history representing the up-thrown side of the Goose Point fault and the other representing the down-thrown side.

Lithology is also needed to run the Burial History model. Spontaneous Potential (SP) logs were used to estimate a clean shale (100% shale) line and a clean sand (100% sand) line, where clean shales represent the highest values in millivolts (mv) and clean sands represent the lowest values in mv. Shales were defined as intervals where the magnitude of the SP was greater than 60% of the difference between the 100% sand and shale baselines. SP values less than 60% were defined as sands. *BasinMod* software also uses calculations of decompaction to create the burial

history diagrams and estimate the original thicknesses of each bed during the time of deposition. In this case, the Baldwin-Butler decompaction method was used in the model. This method is based on compaction curves created by Baldwin et al. (1985).

After the burial history diagrams for both wells were generated, the base of the oldest horizon in the down-thrown well was plotted overlying the bottom horizon from the up-thrown well in order to determine when possible initiation of fault motion on the down-thrown side of the fault occurred. *BasinMod* also allows the user to download the mathematical estimations used to generate the diagram, so the change in slope due to increased sediment accumulation or subsidence was calculated. Burial history diagrams were used to identify periods of increased fault displacement or quiescence. This assessment is based on changes in sediment accumulation or differential subsidence during the burial of sediments in the Pontchartrain Basin, along with other evidence of displacement found in deep seismic or well log cross-sections.

### ***3.4 Shallow Vibracore Data***

In order to examine the shallow stratigraphic relationships adjacent to the projected trend of faults a total of 22 vibracores were acquired across the EOLB (Fig. 25) for chronostratigraphic and lithostratigraphic correlations. Vibracoring is a widely used technique for examining the 3-D framework of shallow strata and was completed by vibrating 3-inch diameter, aluminum irrigation tubing into the subsurface. Each core was logged in detail using standard logging techniques that focused on documenting the lithology, identifiable sedimentary structures, percentage of sand in the matrix, and samples for radiocarbon dating. Descriptions of vibracores from this study, including those collected by Flocks et al. (2009b) and Dunbar et al. (1994), were used to lithologically correlate Pleistocene-Holocene strata and the Pleistocene-Holocene contact

(if penetrated). The results of this analysis were used to make structural cross-sections to investigate lateral continuity between the fault segments and the potential for those fault segments, if active through the Holocene, to cause land loss.

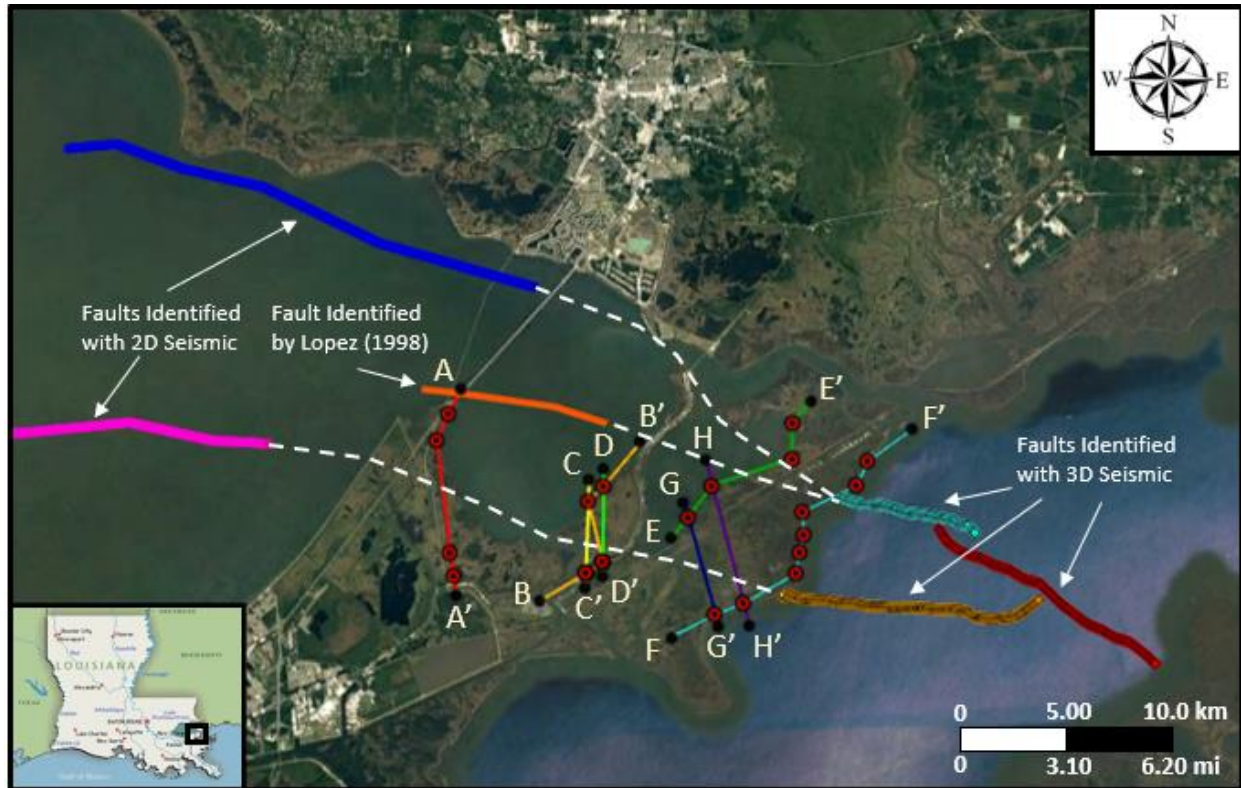


**Figure 25.** 22 locations (red circles) of vibracores collected for this study. Also shown are the projected surface traces of identified faults, potential surface traces of faults (dashed lines), cross-section lines (colored lines), and cross-section endpoints (labeled by tan letters). These cross-sections were used to assess offset of shallow stratigraphy as a result of fault slip.

### 3.4.1 Chronostratigraphic Correlation

Vibracores may also be chronostratigraphically correlated using radiocarbon dating of appropriate samples. In order to determine fault displacement, structural cross-sections were made along with estimates of isochrons (lines of equal age) calculated from radiocarbon dated samples. Radiocarbon samples including *Rangia cuneata* shells and relict marsh organics were collected and  $C^{14}$  dated, only where available samples met the minimum standards set by the radiocarbon dating company. In this case, the samples were sent to Direct AMS for  $C^{14}$  dating.

Direct AMS required samples to be dried, weighed to make sure the minimum requirements were fulfilled (20-50 g of organic sediments and at least 20 mg of carbonate shell), wrapped in tin foil, sealed in two separate zip-lock bags, and packaged for shipping. Direct AMS then returned the samples along with the uncalibrated radiocarbon age before present (BP) and units of percent modern carbon (pMC). These dates were used in the structural cross-sections of the vibracores.

Radiocarbon dates were also used to estimate depths of isochrons in 500 yr BP intervals. This was accomplished by calculating the accumulation rate from the depth and age of the radiocarbon sample. Then, assuming a steady accumulation rate, the accumulation rate was multiplied by 500 yr BP intervals to estimate the depths of the isochrons in each vibracore. These isochrons were contoured to determine offsets across the faults in the structural cross-sections. Fault displacement rates were calculated by dividing the difference between down-thrown & up-thrown isochron depth by the isochron age. This resulted in displacement rates of each fault segment during 500 yr BP intervals in situations where available radiocarbon samples were present in vibracores on each side of the fault segment. However, these estimates are made under the assumption that accretion rates in the region have remained relatively stable during 500 yr BP time intervals and that the effects of erosion or differential subsidence are negligible.

### **3.4.2 Lithostratigraphic Correlation**

Lithostratigraphic correlations were made using shallow vibracore samples in order to see if the BRFS and LBFS segments are causing offset in recent time (Holocene), because most well logs collected by the petroleum industry do not record SP and Resistivity until reaching depths below a few hundred feet or more of true vertical depth. Figure 25 shows a map of proposed faults that were projected up to the surface within the study area and lithostratigraphic correlation

of vibracores across these faults may provide evidence of fault displacement in the Holocene. This map, using analysis of the deep seismic data, led to the 22 vibracore locations sampled (Fig. 25). These vibracores were then described and used to create 22 composite logs. The composite logs were correlated based on lithostratigraphy. Then, structural cross-sections were made that identify lithologic boundaries in the vibracores.

### **3.4.3 Pleistocene-Holocene Sediment Analysis**

Pleistocene-Holocene sedimentation in Lake Pontchartrain and Lake Borgne is limited with sediments consisting of a grain size less than 63  $\mu\text{m}$  in 70% of sediments indicating low energy environments (Flocks et al., 2009b). Lake Pontchartrain is restricted from high rates of sedimentation because bed load influx from major rivers (Mississippi and Pearl) has been minimal since the Holocene (Flocks et al., 2009b). Most of the shallow sediments were derived from erosion of the Pleistocene terraces to the north and Holocene delta plain to the South (Flocks et al., 2009b). Figure 26 shows a generalized composite log from Flocks et al. (2009b) used to correlate shallow stratigraphy in this study. The upper 3 m (10 ft) of sediments are generally massive muds, with bioturbation and shell material throughout (Flocks et al., 2009b). In some locations a lithologically distinct Holocene stratum near the middle of the Holocene section is as much as 70 cm (27 in) thick and consists of a heavily bioturbated, brownish-gray mud with sand-filled burrows and shell lags. Shell lags within the core are bold acoustic layers that appear as bold reflectors on high-resolution seismic surveys (Flocks et al., 2009b). These strata along with the Pleistocene-Holocene contact were useful for correlating vibracores and making interpretations of possible Holocene offset by the BRFS. Pleistocene sediments, below the unconformable Pleistocene-Holocene contact (Saucier, 1994), consist of stiff, olive-gray, silty clays with oxidized organic material and sand-filled burrows (Flocks et al., 2009b). These

sediment descriptions were used to identify important lithologic horizons within the shallow vibracores. Structural cross-sections of vibracores (from the up-thrown fault block to the down-thrown fault block) that show abrupt vertical displacement of Holocene shell lag strata or the Pleistocene-Holocene contact along strike of the fault segments likely indicate the presence of fault displacement.

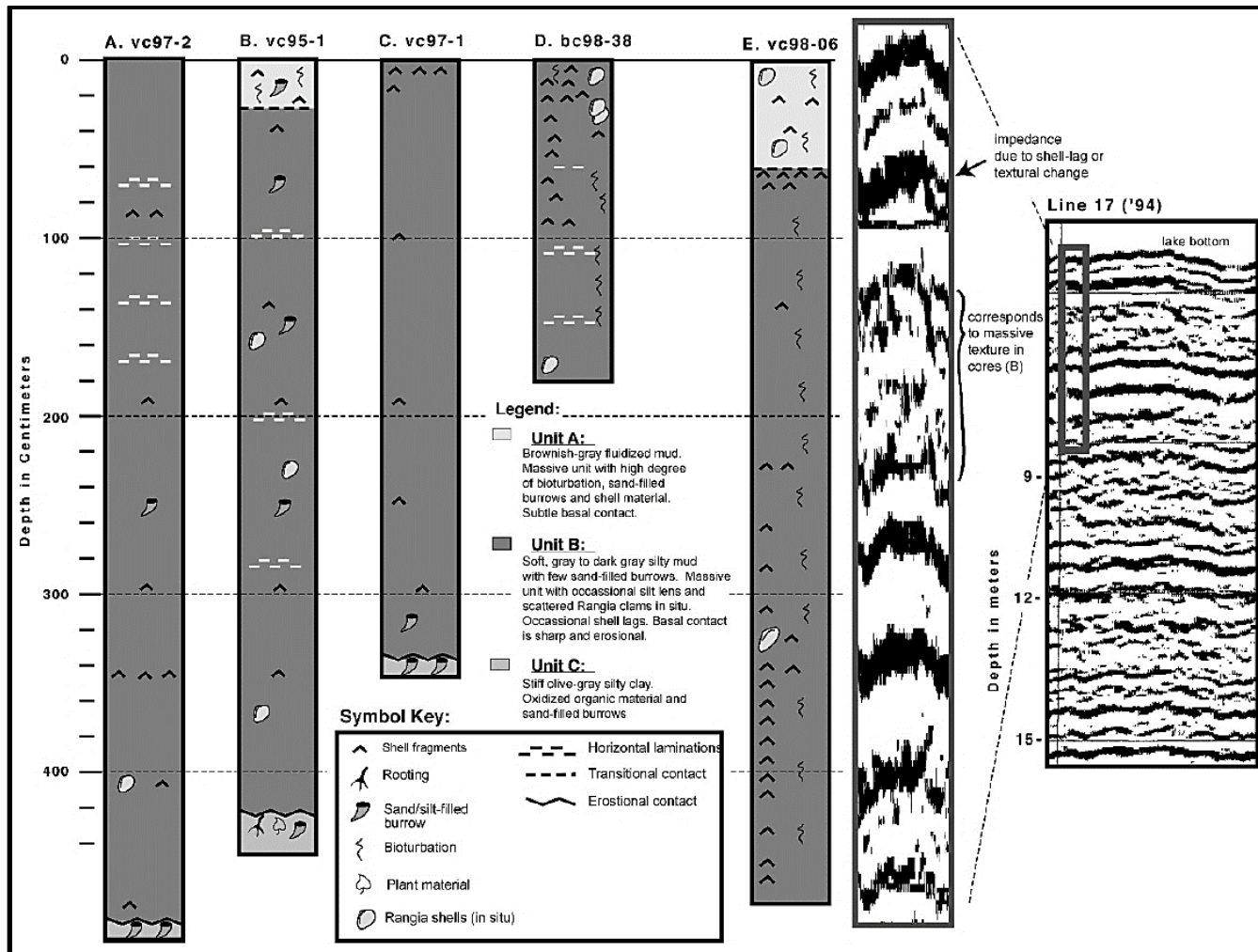


**Figure 26.** Composite logs from Flocks et al. (2009b) show the massive bedded silts and clays typical of Lake Pontchartrain stratigraphy. Logs were constructed from a collection of vibracores (vc97-2, vc95-1, vc97-1, vc98-06) and a box core (bc98-38). A high-resolution seismic profile line (HRSP line 17) was compared with vibracore 98-06, and it was determined that acoustic reflectors coincide with textural variability recorded in the vibracores. These composite logs were used in combination with composite logs from Roth (1999) and cross-sections made by Dunbar et al. (1994) to identify and correlate shallow stratigraphy within the study area.

#### **3.4.4 Pleistocene-Holocene Stratigraphic Analysis**

Stratigraphic analysis is necessary to identify the shallow stratigraphy in vibracores associated with the Pleistocene-Holocene strata and contact. Roth (1999), Flocks et al. (2009), and Dunbar et al. (1994) show composite logs or cross-sections that may be used to compare shallow lithology in the study area. Roth (1999) interpreted Chirp seismic and boring logs from the Dunbar et al. (1994) cross-sections and formulated a composite log (Fig. 27) consisting of the following layers: Unit A, a brownish gray liquid mud with a shell lag common at the base; Unit B, a gray to dark gray silty mud with sand filled burrows; and Unit C, a massive olive gray, very stiff, silty clay with oxidation and oxidized organics. Unit A was interpreted by Roth (1999) as dredge spoil and newly deposited lacustrine sediments, whereas in Unit B coarsening texture, increasing stiffness, and increasing burrowing with depth led to the conclusion that Unit B is a Holocene interdistributary and lacustrine (regressive) mud grading downward into silty to sandy nearshore gulf and bay sound (transgressive) deposits at the base. Unit C, however, contains in place rooting, sand filled burrows, and diagenetic nodules, which led Roth (1999) to define it as Pleistocene deposits. The Dunbar et al. (1994) cross-sections (Figs. 10-11) also mention sandy deposits from a relic beach environment that exist near the Lake St. Catherine region, which was used for describing vibracores collected in this locality.

The composite log from Roth (1999) and cross-sections from Dunbar et al. (1994) were used to correlate shallow stratigraphy in the study area. Offset of shallow stratigraphy across the projected fault trace indicates the presence of faults, unless the amount of offset is close to the regional dip of the stratum. The results of this analysis were correlated with shallow Chirp seismic data to determine if similar rates of offset are evident. If there is visual evidence of stable marsh on the up-thrown side of the projected fault trace and surface expressions such as marsh

break-up areas or open water on the down-thrown side shown in aerial photography, this study would further support the hypothesis that fault-related subsidence impacts local geomorphology as suggested by Gagliano et al. (2003).

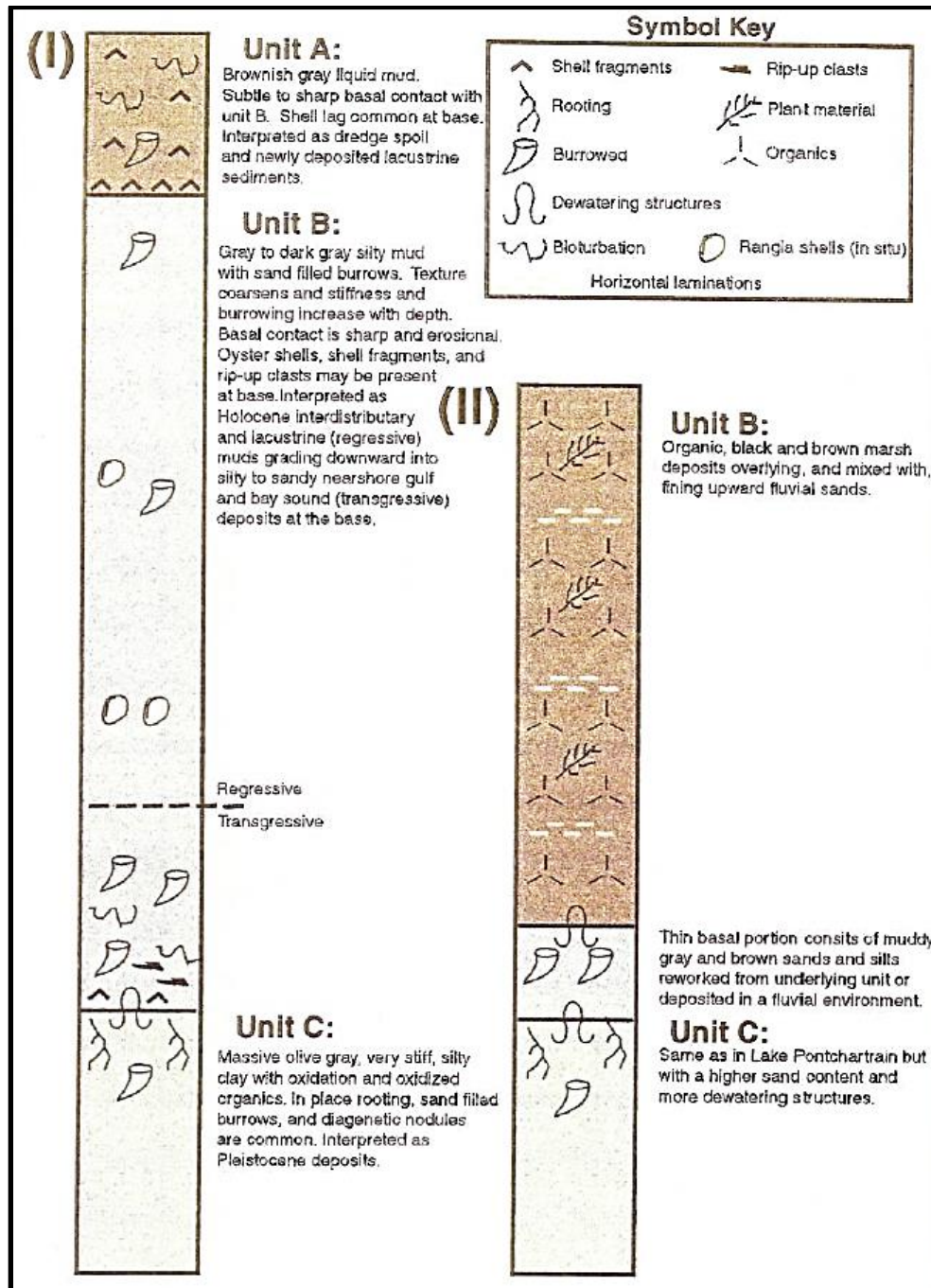


**Figure 27.** Generalized composite logs of (I) Lake Pontchartrain and (II) Bayou Lacombe from analysis of vibracores and Dunbar et al. (1994) boring logs (from Roth, 1999). These logs were used to identify the shallow stratigraphy of collected vibracores from Lake Pontchartrain.

### ***3.5 Chirp Seismic Data***

High resolution, shallow seismic data was collected in the study area (Fig. 28) using an *Edgetech* SB-216 Compressed High Intensity Radar Pulse (Chirp) system, which consists of a tow fish and a 3100-p topside processor. Geographic locations of the lines collected are recorded using a combination of *HYPACK* software, *Discover 3100* software, and connections to a Trimble Pro XRS Global Positioning System, which map proposed Chirp lines, record sub-surface seismic data, and record location in real time, respectively. The *Edgetech* SB-216 tow fish contains a singular transducer for emitting the acoustic signal and two receiver arrays. The system operates in the frequency range of 2-16 kHz providing penetration depths of as much as 91 m (300 ft) depending on the sediment characteristics (Avseth et al., 2010). Typical vertical resolution is about 6.0 cm (2.4 in.) assuming a 2-15 kHz bandwidth (EdgeTech, 2015). Depths of acoustic penetration may reach down to 80.0 m (262 ft) in soft clays but may only reach depths of about 6.0 m (19.7 ft) or less in coarse and calcareous sands (EdgeTech, 2015). Adjustments to the gain or bandwidth were made in order to attain a better depiction of the subsurface within the *Discover 3100* software. Collection information about weather conditions and important *Discover 3100* settings used in the field were recorded in Appendix B. Therefore, this system is considered reliable for creating accurate depictions of the subsurface strata.

Chirp data collected in this study was used to detect offset of near-surface strata, quantify near-surface fault displacement rates, and map structure below the Pleistocene-Holocene contact. Offset of near-surface strata along the proposed fault traces will confirm the presence of fault segments. If noticeable offset of strata was visible in the Chirp data located in proximity of collected vibracore data (within ~914 m or ~3000 ft), displacement rates were calculated from offsets of C14 age-dated vibracore strata (organic horizons and shells). The Chirp seismic data

was collected, then loaded into *IHS Kingdom* for processing and interpretation. The seismic lines were processed using a frequency filter in *IHS Kingdom*. This was accomplished by processing multiple traces in the trace calculator from within the software. Horizons in vibracores were converted to twt using a value of  $1500 \text{ ms}^{-1}$  (EdgeTech, 2015), so that horizons could be identified on Chirp data. This value was also used to calculate the resolution of the data, using the same method as in the deep seismic resolution calculations.

After the vibracore lithology and isochron depths were converted to twt, they were tied to Chirp seismic data to make age-constrained lithologic correlations as well. Structural cross sections were then made from vibracore composite logs and radiocarbon dated samples to confirm the rate of offset in Chirp seismic sub-surface strata. The combination of these correlations to Chirp seismic allows for the calculation of fault displacement rates for segments of the BRFS and LBFS between relative age-dated lithologies or isochrons.

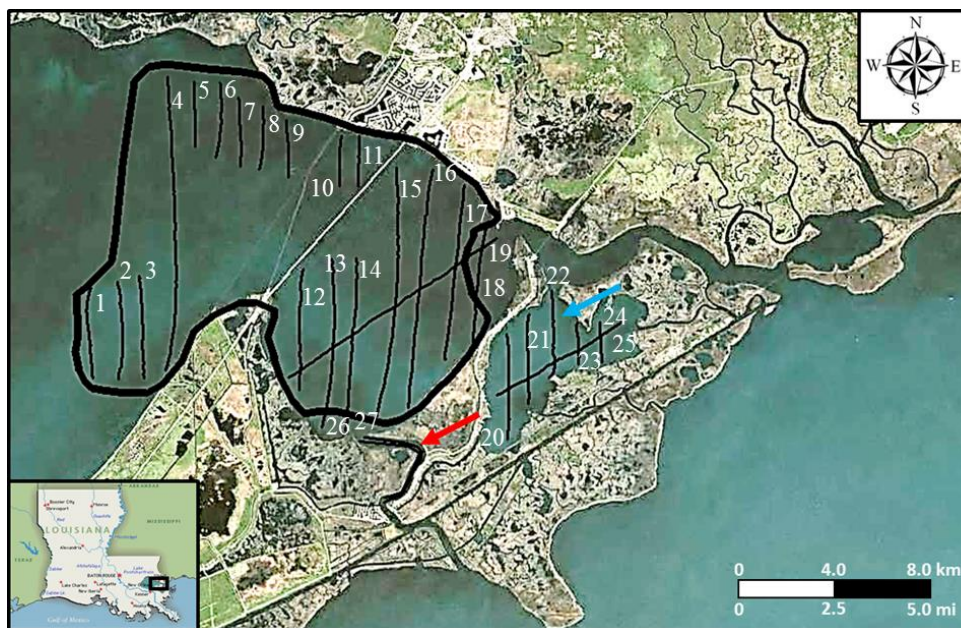


**Figure 28.** Map of the 27 Chirp lines collected and processed in this study (labeled with white numbers). These lines were positioned to attempt to capture any offset in subsurface strata in the easternmost portion of Lake Pontchartrain, the entirety of Lake St. Catherine (labeled by a blue arrow), and the northern portion of Chef Menteur Pass (labeled by the red arrow). The thick black polygon represents the extent of the area where Chirp data were used to generate a twt structure map on the top of the Pleistocene horizon.

### ***3.6 Aerial Imagery and Lidar Data***

Evidence of recent fault slip may be found in the form of surface expressions or abrupt changes in elevation at the surface along the fault trace. Gagliano et al. (2003) suggest that an active fault system will cause surface expressions such as ballooned channels, open water on the down-thrown side of the fault, broken marsh on the down-thrown side of the fault, and stream alignment. The United States Geological Survey (USGS) LandSat Look Viewer Tool provides imagery of a defined area in Louisiana dated any time after 1982. Images of the study area were analyzed in two-year intervals until the 2018 image was reached. Any surface expressions visible along the projected surface fault traces were noted.

A key tool that is also used to identify surface fault traces is Light Detection and Ranging (Lidar). Lidar uses light from pulsed lasers to generate 5x5 meter grid of digital elevation models (DEMs). A surface trace, therefore, was identified by an abrupt change in elevation on the surface. Two datasets were available for use in this study, including a 2003 dataset as part of the “Louisiana Statewide Lidar Project” with a margin of error in vertical resolution of  $\pm 0.1$  m ( $\pm 3.9$  in) taken from Cunningham et al. (2004) and a tile of the 2018 3-D Elevation Program (3-DEP) collected by USGS in 2017 to provide basic elevation information for the “National Map” with a margin of error in vertical resolution of  $\pm 0.1$  m ( $\pm 3.9$  in) as well (USGS, 2018). These datasets were loaded into ArcMap 10.4.1 software, and the symbology was set to increments of 0.25 m (0.82 ft) in order to determine if any change in elevation as a result of faulting occurred above the margin of error for the datasets.

## Chapter 4. Results

### 4.1 *LDNR Well Log Correlations*

A component of this research involved analysis of 145 wells obtained through the Louisiana Department of Natural Resources (sonris.com). Of these wells, 31 had available biostratigraphy marker information provided by Paleo Data Inc. Chronostratigraphic correlations were then made using age-constrained biostratigraphy as well as lithostratigraphic correlations between strata with similar spontaneous potential (SP) values between well logs on the up-thrown side and down-thrown side of potentially faulted regions. Three correlation cross-sections hung on a sea-level datum were made (Fig. 20) to assess lateral continuity of faults in the study area. These three cross-sections (Figs. 29-31) show differences in depths to chronostratigraphic markers greater than differences caused by regional dip or increases in expansion with depth. The depth differences and/or expansion with depth suggest the presence of fault offset between wells on the cross-sections. Furthermore, fault displacement beneath the EOLB is evident as these well log cross-sections continue across the land bridge. However, whether individual segments are in lateral communication along the same fault trace or split into separate fault segments cannot be determined from the available data.

The biostratigraphy markers from those cross-sections were also used to generate a depth vs. expansion indices graph (Fig. 32), a depth vs. throw graph (Fig. 33), and an expansion index vs. time graph (Fig. 34) for the Goose Point Fault. The resulting graphs show two abrupt increases in fault throw and expansion indices values which correspond to periods of initial fault displacement like those hypothesized by McCulloh and Heinrich (2012).

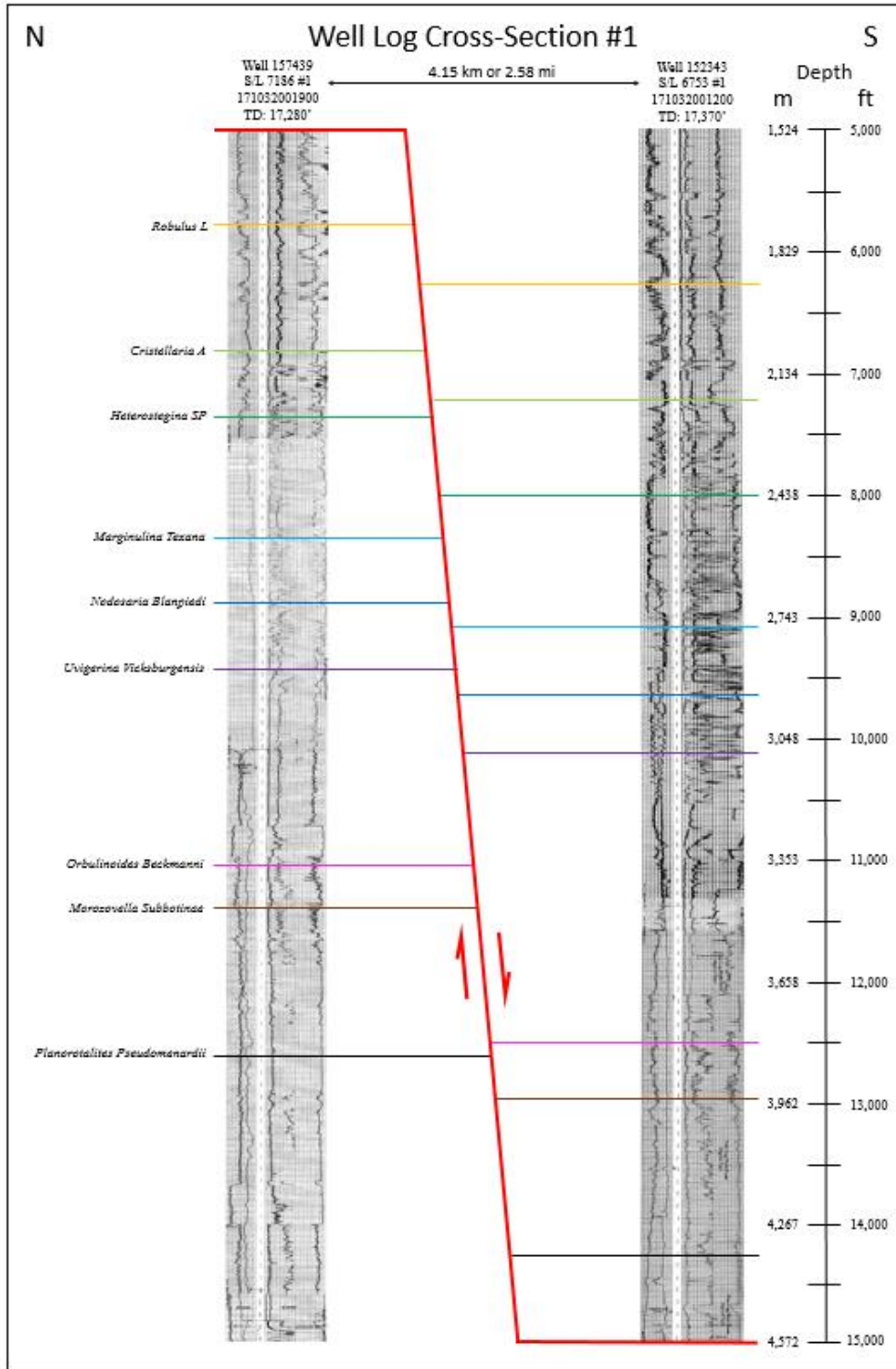


**Figure 29.** Cross-section constructed with biostratigraphic data from Paleo Data Inc. (2018) and well logs from SONRIS. Clear vertical offset of biostratigraphic horizons is visible. Expansion and fault throw were calculated for each biostratigraphic interval. The offset caused by the fault is greater than the regional dip between the two wells in the cross-section.

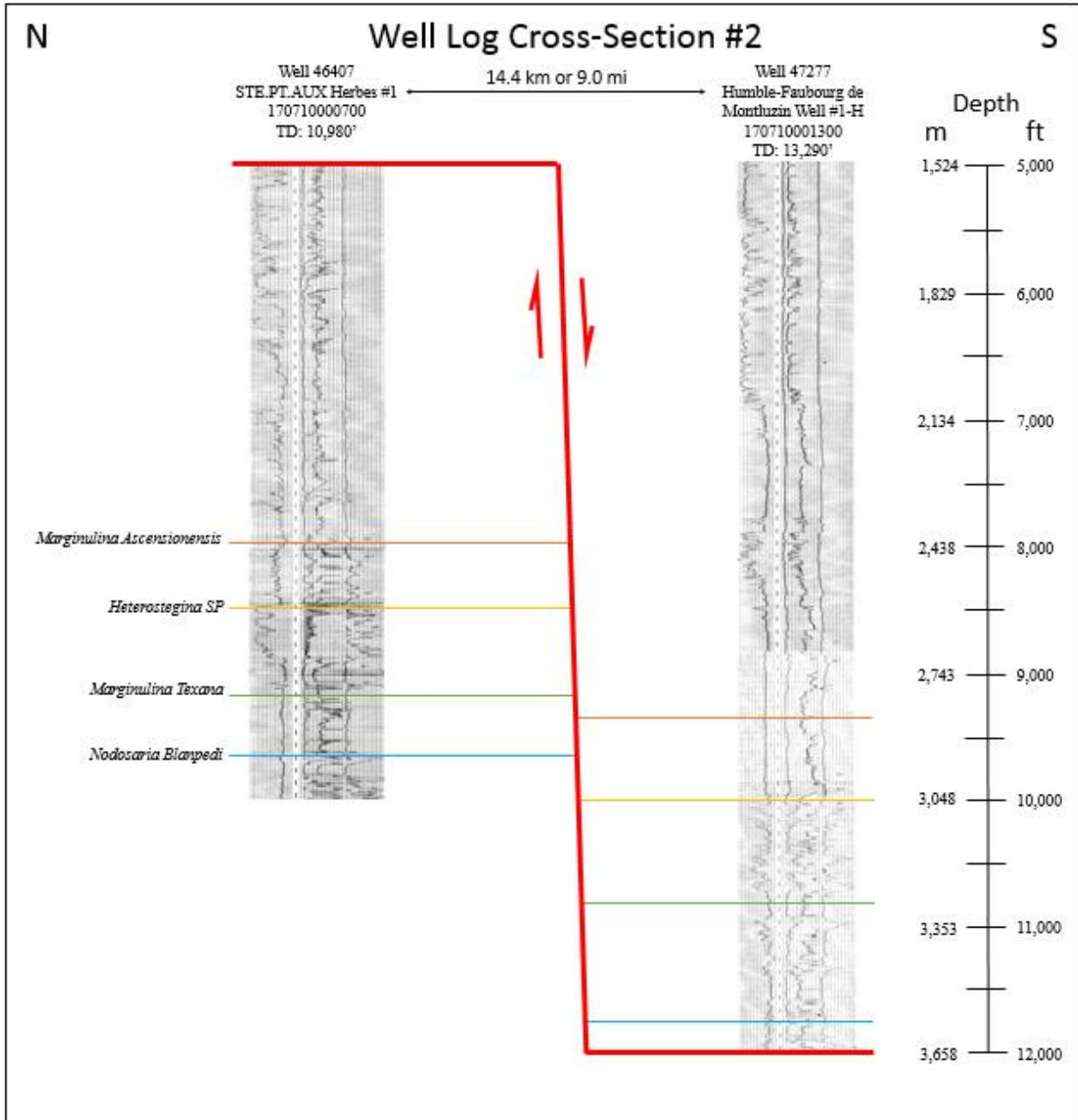


**Figure 30.** Cross-section constructed with biostratigraphic data from Paleo Data Inc. (2018) and well logs from SONRIS. Clear vertical offset of biostratigraphic horizons is visible. Expansion and fault throw were calculated for each biostratigraphic interval. The offset of the biostratigraphy is close to the regional dip of the strata, however, expansion increases with depth indicating fault motion.

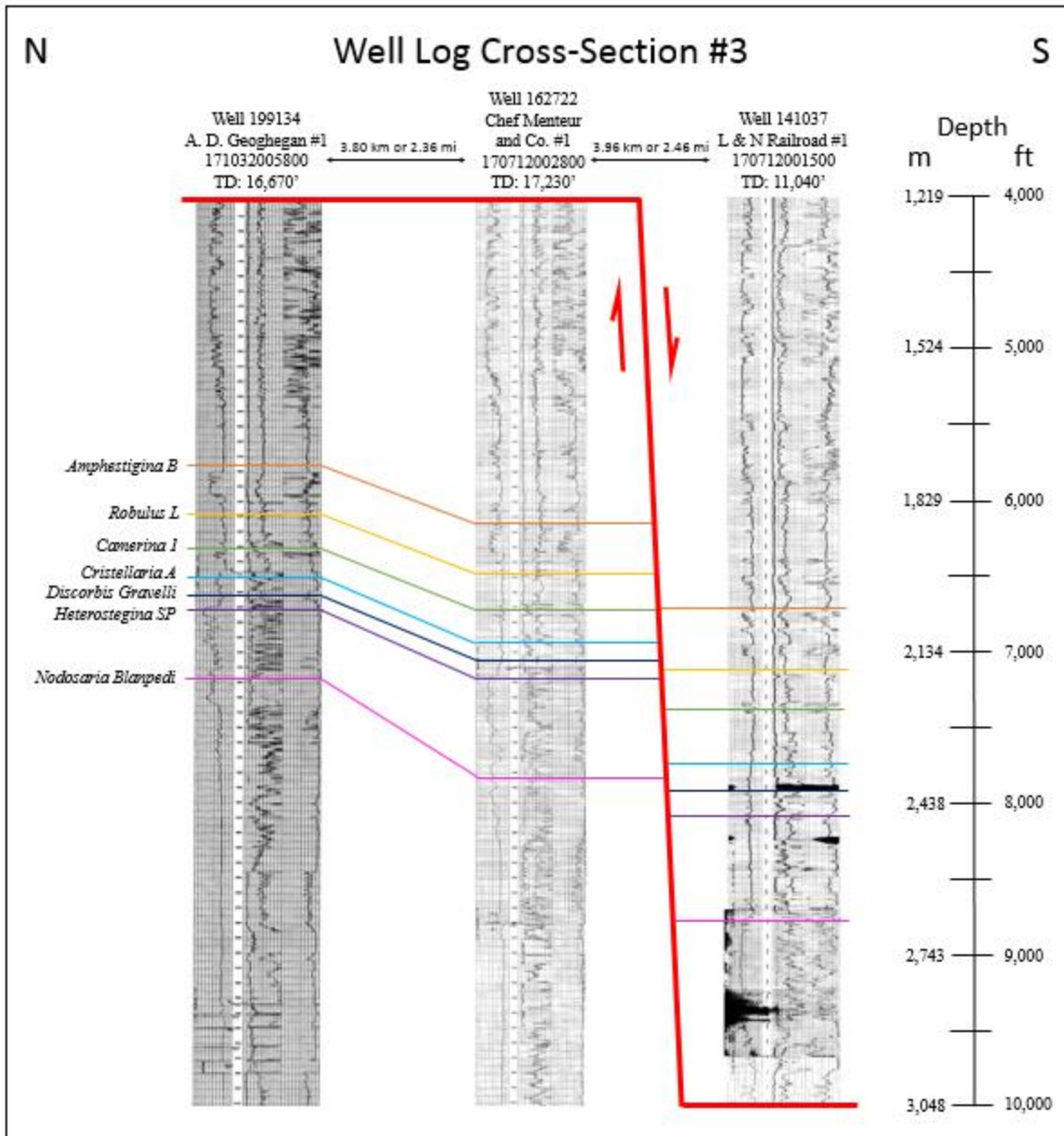


**Figure 31.** Cross-section constructed with biostratigraphic data from Paleo Data Inc. (2018) and well logs from SONRIS. Clear vertical offset of biostratigraphic horizons is visible. Expansion and fault throw were calculated for each biostratigraphic interval. The offset caused by the fault is greater than the regional dip between the first two wells in the cross-section.

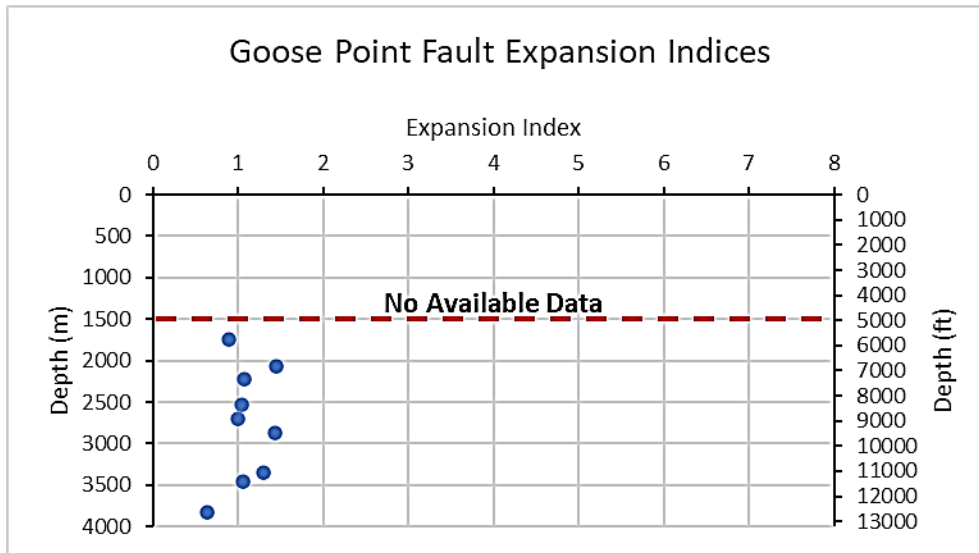


**Figure 32.** Plot of expansion indices for the identified biostratigraphic intervals from correlated well logs. Points were plotted by comparing the calculated expansion index for a biostratigraphic marker against the depth of the up-thrown depth of the biostratigraphic marker. Note the presence of low expansion indices at depth, followed by two peaks in expansion between 2,591-3,505 m (8,500-11,500 ft) and 1,829-2,286 m (6,000-7,500 ft), but then a subsequent decrease above 1,829 m (6,000 ft). No data were available above the dashed red line.

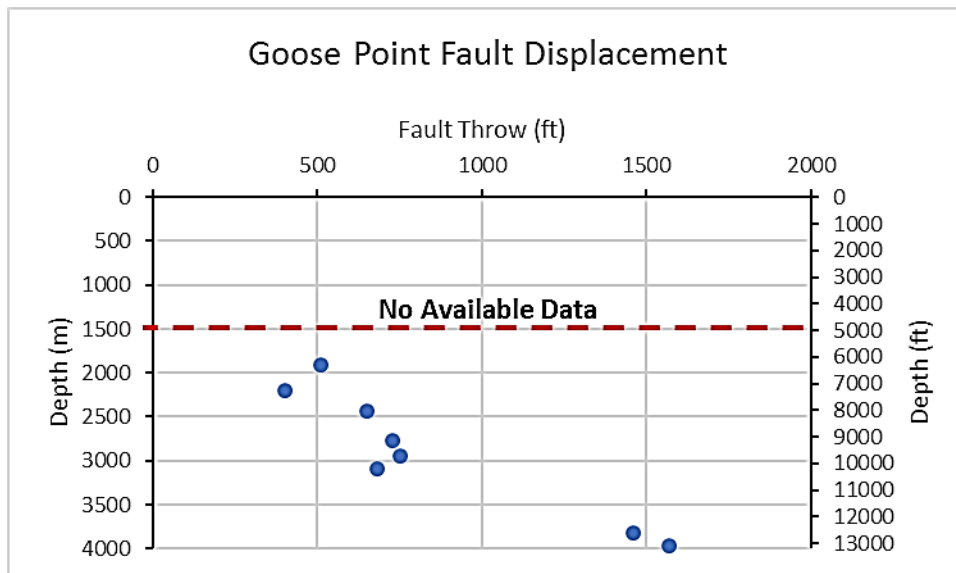


**Figure 33.** Plot comparing fault throw of biostratigraphic horizons (in ft) to the upthrown depth of the biostratigraphic horizon. A trend of increasing fault throw with depth is observable. Exceptions at approximately 3,050 m (10,000 ft) and 2,130 m (7,000 ft) may indicate correlation and/or measurement errors.

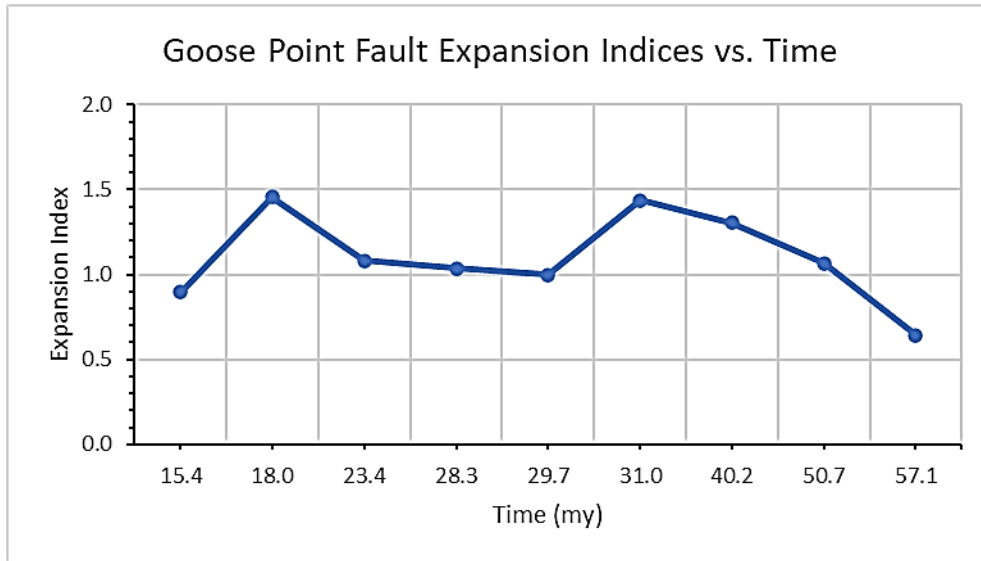


**Figure 34.** Graph of expansion indices for available biostratigraphic horizons compared to the time period associated with the biostratigraphic horizon. There is an increase in expansion (index > 1) beginning after 50.7 my, reaching a peak at approximately 31.0 my, followed by another increase at 23.4 my, reaching a peak at 18.0 my. These suggest there was an initiation of the Goose Point Fault displacement and accommodation during the Early Eocene, a peak of fault expansion during the Early Oligocene and Middle Miocene, and declining expansion after the Middle Miocene.

#### ***4.2 Lake Pontchartrain and Lake Borgne Seismic Interpretation***

Fault offset of horizons is not visible above 0.08 s twt on the 2-D seismic data in Lake Pontchartrain due to acquisition and processing parameters. Chirp seismic data was collected in areas near the projected surface trace of identified faults (Table 2) to image the shallow subsurface. The identified faults (Fig. 21) appear to be syndepositional with Holocene strata. The fault labeled in dark orange (Fig. 21) in Lake Pontchartrain is a fault previously identified by Lopez et al. (1997) that could be active in the Holocene, but the fault is located outside the scope of the 2-D dataset. In the 2-D dataset, the Lake Pontchartrain and Goose Point Faults show offset to depths of at least 3.0 s twt with resolution declining at approximately 2.5 s twt. A top structure map of *Heterostegina SP* was created (Fig. 35) and shows the Lake Pontchartrain and Goose Point Faults extend to depth, offsetting the *Heterostegina SP* pick at approximately 2,800 m (9,200 ft) and 2,300 m (7,550 ft), respectively. The western 3-D dataset, which extends to a

depth of 6 s twt captures the edge of a segment of the Lake Borgne Fault system (the red fault in figure 21). This segment continues to a depth of at least 3.5 s twt and likely into deeper strata, but resolution declines below 3.5 s twt. Therefore, the fault can be defined as deep-seated, but the period of initial fault slip cannot be determined with the available biostratigraphy data. The 3-D eastern dataset in Lake Borgne has 3 previously identified faults (Fig. 21) that have been projected up to the surface. The goal of this project, however, is to determine if these faults continue stratigraphically upward through the land bridge geomorphology as faults of the larger Baton Rouge Fault System.

Rate of fault offset for time increments was calculated for the Lake Pontchartrain and Goose Point Faults. Rate of fault offset for time increments defined by *Robulus L* and older foraminifera are constrained by biostratigraphy from Paleo Data Inc. Rate of fault offset for time increments younger than *Robulus L* required estimating depths to shallower biostratigraphic markers (i.e. “pseudo-biostratigraphy picks”). Estimates of “pseudo-picks” were made by assuming a constant rate of sediment accumulation from *Robulus L* to present at wells (Table 3), and then correlating the “pseudo-picks” laterally on 2-D seismic to fault locations. Therefore, rates of fault offset for time increments younger than *Robulus L* have high uncertainty. Rates of fault offset through time show a similar trend for the faults (Fig. 36). Estimates of shallow biostratigraphic horizons necessary to assess these trends are listed in True Vertical Depth (TVD) in Table 3. Earliest documented fault offset occurs between 29.7-18.0 Ma (this period may have begun earlier than the available data), followed by a brief, abrupt increase in the rate of offset for time increments between 18.0-15.0 Ma, then a period of “quiescence” whereby the rate declines sharply between 15.0-6.0 Ma, and finally a period of increasing rate of offset from 6.0 Ma through modern day.

Shallow Seismic Biostratigraphy Estimates for Example Well # 66438				
Biostratigraphy Pick	Depth to Pick (ft)	Depth to Pick (m)	Biostratigraphy Age (My)	Sedimentation Rate (cm/yr)
Angulogerina B	856	261	1.6	0.0163
Globoquadrina Altispira	1604	489	3.0	0.0163
Bulminella 1	2300	701	4.3	0.0163
Robulus E	3209	978	6.0	0.0163
Bigenerina A	3958	1206	7.4	0.0163
Discorbis 12	4920	1500	9.2	0.0163
Textularia W	6418	1956	12.0	0.0163
Robulus L	8250	2516	15.4	0.0163

**Table 3.** Biostratigraphic picks younger than *Robulus L* are not available in the study area. Shallow biostratigraphy was estimated by assuming constant sedimentation rate from *Robulus L* to present at the wells. Example calculations for Well# 66438 are shown above.

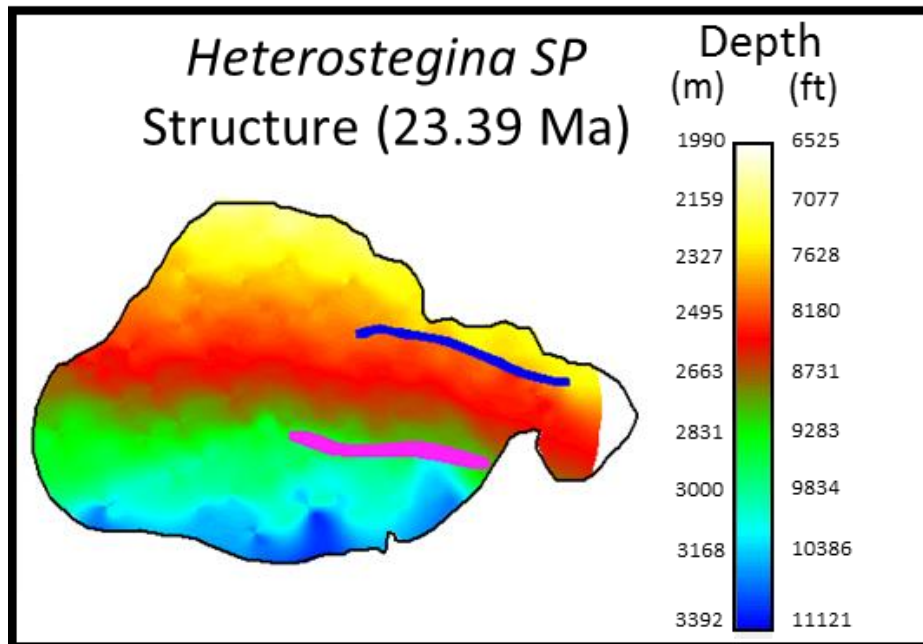


**Figure 35.** Structure map of the *Heterostegina SP* biostratigraphic pick generated in *IHS Kingdom*. The map shows regional south dip, the Goose Point Fault (in blue), and the Lake Pontchartrain Fault (in pink). The faults are down-to-the-south normal faults.

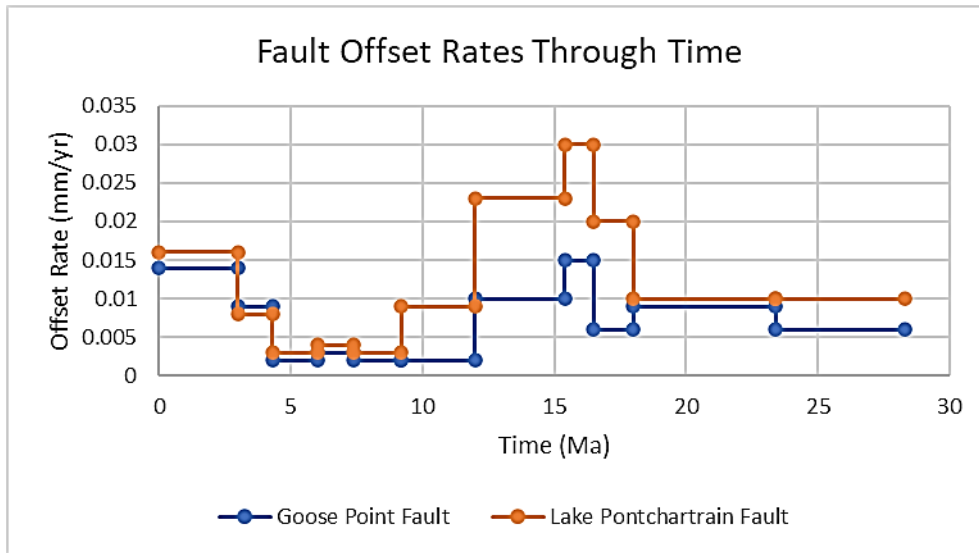


**Figure 36.** Time-averaged rates of fault offset (mm/yr) are constrained by biostratigraphy data for 15.4 Ma and older (*Robulus L* and older) time increments. Time-averaged rates of fault offset (mm/yr) for time increments younger than 15.3 Ma were based on age assignments assuming constant rate of sedimentation from 15.4 Ma to present (see Table 3). Movement on both faults likely began prior to the oldest available biostratigraphic picks, which are tied to 2-D seismic. Rates of offset were highest approximately 16 Ma, declined to near 0 between approximately 9.2 and 4.3 Ma, and have been increasing since approximately 4.3 Ma.

### 4.3 BasinMod Burial History

Burial history curves for two wells were created using BasinMod software and are shown in figure 55. Well# 152343 is on the down-thrown side of the Goose Point Fault and Well# 157439 is on the up-thrown side of the fault. Percent sand calculations for intervals in the wells are shown in Table 4. The red lines on both diagrams in figure 37 represent burial depth through time of *Rosita fornicata* for Well# 152343. The diagrams show an interval of time from 69 Ma to 38 Ma where the up-thrown well has thicker accumulations of sediment followed by an interval of time from 38 Ma to present where there are thicker accumulations of sediment on the down-thrown well. This may be a result of initiation of growth fault movement in the study area during the Late Eocene (~38 Ma).

BasinMod Net-to-Gross Inputs							
Well ID#	Horizon A	Horizon B	Gross Sediment (ft)	Gross Sediment (m)	Net Sand (ft)	Net Sand (m)	Net-to-Gross (%Sand)
152343	5,000 ft (1,524 m)	<i>Robulus L</i>	1250	381	890	271	71
152343	<i>Robulus L</i>	<i>Cristellaria A</i>	950	290	350	107	37
152343	<i>Cristellaria A</i>	<i>Heterostegina SP</i>	800	244	210	64	26
152343	<i>Heterostegina SP</i>	<i>Marginulina Texana</i>	1080	329	680	207	63
152343	<i>Marginulina Texana</i>	<i>Nodosaria Blanpiedi</i>	570	174	70	21	12
152343	<i>Nodosaria Blanpiedi</i>	<i>Uvigerina Vicksburgensis</i>	550	168	30	9	5
152343	<i>Uvigerina Vicksburgensis</i>	<i>Orbulinoides Beckmanni</i>	2330	710	200	61	9
152343	<i>Orbulinoides Beckmanni</i>	<i>Morozovella Subbotinae</i>	470	143	0	0	0
152343	<i>Morozovella Subbotinae</i>	<i>Planorotalites Pseudomenardii</i>	1300	396	30	9	2
152343	<i>Planorotalites Pseudomenardii</i>	<i>Rosita Fornicata</i>	700	213	160	49	23
157439	5,000 ft (1,524 m)	<i>Robulus L</i>	740	226	600	183	81
157439	<i>Robulus L</i>	<i>Cristellaria A</i>	1060	323	280	85	26
157439	<i>Cristellaria A</i>	<i>Heterostegina SP</i>	550	168	220	67	40
157439	<i>Heterostegina SP</i>	<i>Marginulina Texana</i>	1000	305	690	210	69
157439	<i>Marginulina Texana</i>	<i>Nodosaria Blanpiedi</i>	550	168	220	67	40
157439	<i>Nodosaria Blanpiedi</i>	<i>Uvigerina Vicksburgensis</i>	550	168	0	0	0
157439	<i>Uvigerina Vicksburgensis</i>	<i>Orbulinoides Beckmanni</i>	1620	494	630	192	39
157439	<i>Orbulinoides Beckmanni</i>	<i>Morozovella Subbotinae</i>	360	110	300	91	83
157439	<i>Morozovella Subbotinae</i>	<i>Planorotalites Pseudomenardii</i>	1220	372	1060	323	87
157439	<i>Planorotalites Pseudomenardii</i>	<i>Rosita Fornicata</i>	1090	332	390	119	36
47277	5,000 ft (1,524 m)	<i>Marginulina Ascensionensis</i>	5040	1536	1860	567	37
47277	<i>Marginulina Ascensionensis</i>	<i>Heterostegina SP</i>	420	128	130	40	31
47277	<i>Heterostegina SP</i>	<i>Marginulina Texana</i>	690	210	280	85	41
47277	<i>Marginulina Texana</i>	<i>Nodosaria Blanpiedi</i>	460	140	20	6	4
47277	<i>Nodosaria Blanpiedi</i>	10,000 ft (3,048 m)	390	119	20	6	5
46407	5,000 ft (1,524 m)	<i>Marginulina Ascensionensis</i>	2980	908	1010	308	34
46407	<i>Marginulina Ascensionensis</i>	<i>Heterostegina SP</i>	520	158	30	9	6
46407	<i>Heterostegina SP</i>	<i>Marginulina Texana</i>	690	210	420	128	61
46407	<i>Marginulina Texana</i>	<i>Nodosaria Blanpiedi</i>	490	149	90	27	18
46407	<i>Nodosaria Blanpiedi</i>	10,000 ft (3,048 m)	320	98	60	18	19
141037	4,000 ft (1,219 m)	<i>Amphestigina B</i>	3250	991	1520	463	47
141037	<i>Amphestigina B</i>	<i>Robulus L</i>	290	88	50	15	17
141037	<i>Robulus L</i>	<i>Camerina 1</i>	320	98	40	12	13
141037	<i>Camerina 1</i>	<i>Cristellaria A</i>	130	40	30	9	23
141037	<i>Cristellaria A</i>	<i>Discorbis Gravelli</i>	60	18	10	3	17
141037	<i>Discorbis Gravelli</i>	<i>Heterostegina SP</i>	70	21	20	6	29
141037	<i>Heterostegina SP</i>	<i>Nodosaria Blanpiedi</i>	740	226	240	73	32
141037	<i>Nodosaria Blanpiedi</i>	10,000 ft (3,048 m)	1140	347	860	262	75
162722	4,000 ft (1,219 m)	<i>Amphestigina B</i>	2130	649	950	290	45
162722	<i>Amphestigina B</i>	<i>Robulus L</i>	330	101	130	40	39
162722	<i>Robulus L</i>	<i>Camerina 1</i>	250	76	10	3	4
162722	<i>Camerina 1</i>	<i>Cristellaria A</i>	210	64	10	3	5
162722	<i>Cristellaria A</i>	<i>Discorbis Gravelli</i>	60	18	0	0	0
162722	<i>Discorbis Gravelli</i>	<i>Heterostegina SP</i>	130	40	10	3	8
162722	<i>Heterostegina SP</i>	<i>Nodosaria Blanpiedi</i>	670	204	130	40	19
162722	<i>Nodosaria Blanpiedi</i>	9,000 ft (2,743 m)	1180	360	280	85	24
199134	4,000 ft (1,219 m)	<i>Amphestigina B</i>	1740	530	780	238	45
199134	<i>Amphestigina B</i>	<i>Robulus L</i>	320	98	140	43	44
199134	<i>Robulus L</i>	<i>Camerina 1</i>	240	73	20	6	8
199134	<i>Camerina 1</i>	<i>Cristellaria A</i>	190	58	30	9	16
199134	<i>Cristellaria A</i>	<i>Discorbis Gravelli</i>	120	37	10	3	8
199134	<i>Discorbis Gravelli</i>	<i>Heterostegina SP</i>	90	27	5	2	6
199134	<i>Heterostegina SP</i>	<i>Nodosaria Blanpiedi</i>	460	140	250	76	54
199134	<i>Nodosaria Blanpiedi</i>	<i>Parasubbotina Pseudobulloides</i>	3110	948	1000	305	32

**Table 4.** This table lists all the well log data used to run BasinMod. This includes the Well ID #, the two horizons used to calculate a net-to-gross (Horizon A and Horizon B), the gross sediment between the two horizons (in ft and m), the net amount of sand in the rock column (in ft and m), and the percentage of net-to-gross calculated by dividing the net sand by the gross sediment that was input into the stratigraphy used to run the BasinMod burial history model.

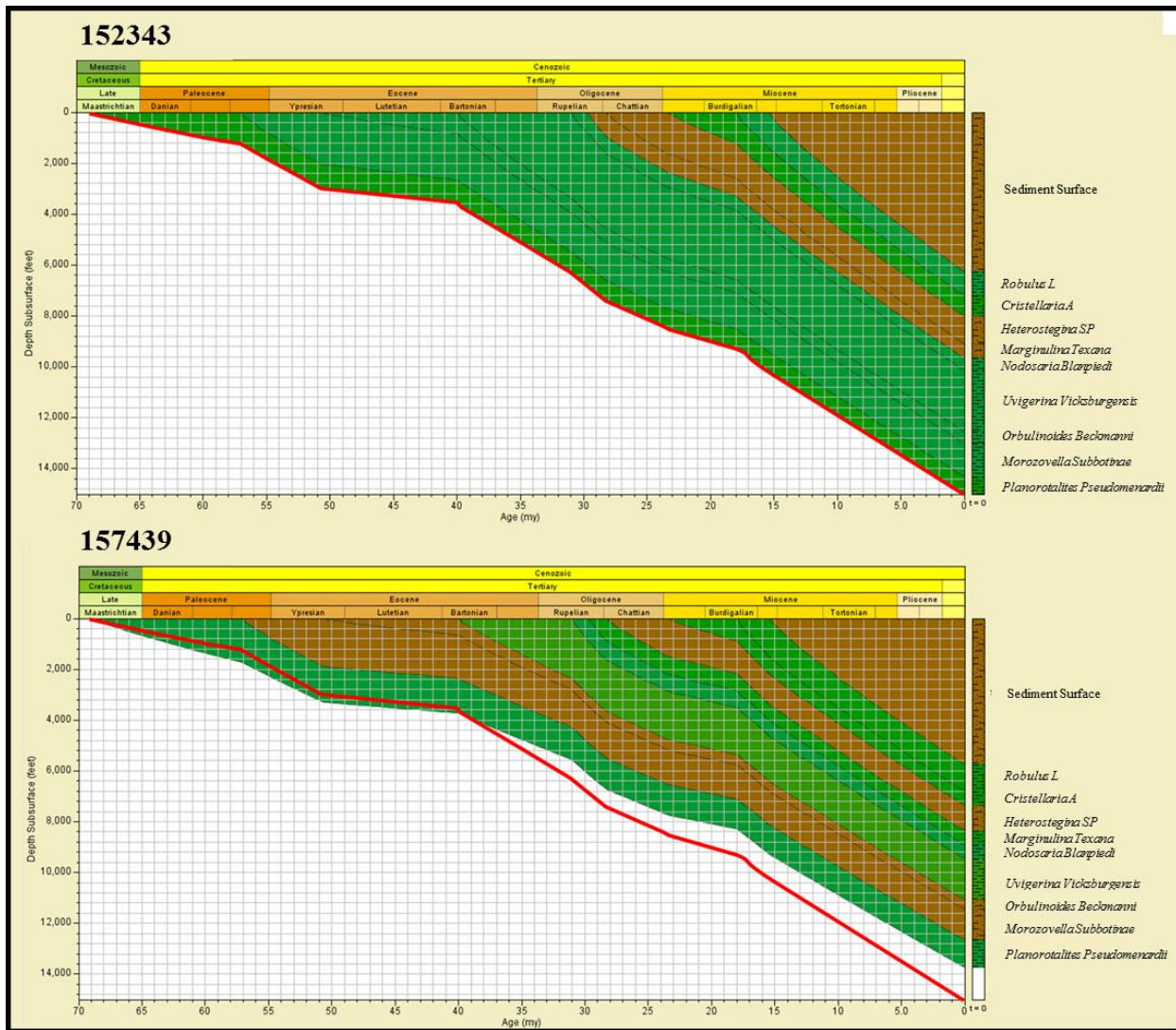


**Figure 37.** A burial history diagram for Well #157439, up-thrown side of the Goose Point Fault, and Well #152343, down-thrown side of the Goose Point Fault, generated using *BasinMod* software. Biostratigraphy data from well logs were input into the model beginning at 69 Ma. Olive green represents 45-55% sand, dark green 0-44% sand, and brown 56-100% sand. The red line in Well #152343 represents the bottom biostratigraphic horizon (*Rosita fornicata*) and was plotted overlaying Well #157439. The result is an interval of time from 69 Ma to 38 Ma where the up-thrown well has thicker accumulations of sediment followed by an interval of time from 38 Ma to present where there are thicker accumulations of sediment on the down-thrown well. This may be a result of initiation of growth fault movement in the study area during the Late Eocene (~38 Ma).

#### **4.4 Shallow Vibracore Correlations**

Vibracores were collected from the upthrown and downthrown sides of the projected surface traces of potentially active faults to litho- and chronostratigraphically assess recent fault history. A total of 22 vibracores were collected (Fig. 25). Core descriptions are provided in Appendix A. In this study the average depth of penetration was 4.76 m (15.62 ft) with the deepest penetration at 6.69 m (21.95 ft) and the shortest at 1.96 m (6.43 ft). From this set of cores, 8 cross-sections (Fig. 25) were created in order to lithostratigraphically and chronostratigraphically correlate shallow strata (Figs. 38-50). *Rangia cuneata* and bulk organic material from relict marshes were collected from 17 core samples and sent to DirectAMS for radiocarbon dating. The resulting radiocarbon information from DirectAMS is listed in Table 5.

Radiocarbon Sample Information										
N	Sample ID	Material	Site, Location	Feature, Stratigraphy Description	Water Depth (cm)	Water Depth (ft)	Total Depth (cm)	Total Depth (ft)	Age (BP)	Age 1 $\sigma$ Error
1	VC-LP-01T	wood	Lake Pontchartrain	silty clay, massive bedding	280	9.19	308	10.10	878	32
2	VC-LP-03S	shell	Lake Pontchartrain	bioturbation, massive bedding	50	1.64	534	17.52	3532	26
3	VC-LP-03B	shell	Lake Pontchartrain	bioturbation, massive bedding	50	1.64	558	18.31	3870	30
4	VC-LP-04B	shell	Lake Pontchartrain	bedding	70	2.30	286	9.38	364	24
5	VC-LP-08B	shell	Lake Pontchartrain	sandy clay, massive bedding	80	2.62	542	17.78	3709	29
6	VC-LB-16T	shell	Lake Borgne	Clay-sand, massive bedding	70	2.30	140	4.59	Modern	N/A
7	VC-LP-02T	sediment (bulk)	Lake Pontchartrain	silty clay, massive bedding	150	4.92	184	6.04	426	29
8	VC-LC-05AT	sediment (bulk)	Lake St. Catherine	silty clay, massive bedding	210	6.89	330	10.83	472	33
9	VC-LC-06AT	sediment (bulk)	Lake St. Catherine	silty clay, massive bedding	280	9.19	348	11.42	305	25
10	VC-LP-07B	sediment (bulk)	Lake Pontchartrain	silty clay, massive bedding	80	2.62	212	6.96	2500	35
11	VC-LB-09T	sediment (bulk)	Lake Borgne	silty clay, massive bedding	80	2.62	213	6.99	1468	35
12	VC-LB-10B	sediment (bulk)	Lake Borgne	silty clay, massive bedding	90	2.95	302	9.91	2124	30
13	VC-LB-11T	sediment (bulk)	Lake Borgne	silty clay, massive bedding	90	2.95	130	4.27	2291	27
14	VC-LB-13T	sediment (bulk)	Lake Borgne	silty clay, massive bedding	80	2.62	212	6.96	1708	27
15	VC-LB-13B	sediment (bulk)	Lake Borgne	silty clay, massive bedding	80	2.62	256	8.40	2047	28
16	VC-LB-14T	sediment (bulk)	Lake Borgne	bedding	130	4.27	235	7.71	2448	25
17	VC-LB-15T	sediment (bulk)	Lake Borgne	silty clay, massive bedding	170	5.58	254	8.33	2105	25

**Table 5.** This table describes vibracore samples used for radiometric dating by DirectAMS. DirectAMS states that all results have been corrected for isotopic fractionation with an unreported  $\delta^{13}\text{C}$  value measured on the prepared carbon by the accelerator and the uncalibrated radiocarbon age was given.

The vibracores collected contained similar stratigraphy to cores collected by Roth (1999) and Dunbar et al. (1994). Note that in every lithostratigraphic cross-section with a projected fault the boundary between older interdistributary/bay sound deposits and younger lacustrine/marsh deposits is structurally higher on the upthrown side of projected fault trace than on the downthrown side of the projected fault trace. (Figs. 38-45). None of the vibracores in this study penetrated deep enough to encounter lithologies matching documented Pleistocene descriptions. However, radiocarbon samples taken from *Rangia cuneata* shells and relic marsh organics were available to date portions of strata and calculate isochrons for some of the cores (Table 6).

Isochron Calculations									
Sample ID	Sediment Accumulation Rates (cm/yr)	500 yr Isochron (cm)	1000 yr Isochron (cm)	1500 yr Isochron (cm)	2000 yr Isochron (cm)	2500 yr Isochron (cm)	3000 yr Isochron (cm)	3500 yr Isochron (cm)	4000 yr Isochron (cm)
VC-LP-01T	0.032	296	312	328	344	360	376	392	408
VC-LP-03S	0.137	119	187	256	324	393	461	530	598
VC-LP-03B	0.131	116	181	247	313	378	444	509	575
VC-LP-04B	0.593	367	663	960	1257	1554	1850	2147	2444
VC-LP-08B	0.125	142	205	267	329	391	454	516	578
VC-LB-16T	N/A	N/A	N/A	N/A	N/A	N/A	N/A	N/A	N/A
VC-LP-02T	0.080	190	230	270	310	350	389	429	469
VC-LC-05AT	0.254	337	464	591	718	846	973	1100	1227
VC-LC-06AT	0.223	391	503	614	726	837	949	1060	1172
VC-LP-07B	0.053	106	133	159	186	212	238	265	291
VC-LB-09T	0.091	125	171	216	261	306	352	397	442
VC-LB-10B	0.100	140	190	240	290	340	389	439	489
VC-LB-11T	0.017	99	107	116	125	134	142	151	160
VC-LB-13T	0.077	119	157	196	235	273	312	350	389
VC-LB-13B	0.086	123	166	209	252	295	338	381	424
VC-LB-14T	0.043	151	173	194	216	237	259	280	302
VC-LB-15T	0.040	190	210	230	250	270	290	310	330

**Table 6.** Isochron calculations were necessary to attempt to quantify rates of displacement in shallow stratigraphy across identified fault segments. Each sample is listed along with the calculated sedimentation rates (in  $\text{cm yr}^{-1}$ ). These sedimentation rates were calculated by dividing the accumulation of sediment (the water depth subtracted from the depth of the sample) by the age of the sample. This sediment accumulation rate was then multiplied by intervals of 500 yr to yield values of depth for each isochron estimate from 500 yr to 4000 yr BP.

Comparisons of isochrons were made under several assumptions including: (1) the stratigraphy in vibracores was originally deposited horizontally, (2) cores collected from channels have been in place with steady sediment supply during the Holocene, (3) no unconformities are present in the cores. These assumptions are supported by previous work by Roth (1999) and Flocks et al. (2009b). Isochron depths were then calculated between cores (one up-thrown and one down-thrown for each projected fault) and divided by the age of the isochron to estimate rates of fault offset (Figs. 46-50). The average rate of fault offset of the Lake Pontchartrain Fault ranged from  $0.07 \text{ cm yr}^{-1}$  ( $0.028 \text{ in yr}^{-1}$ ) to  $0.31 \text{ cm yr}^{-1}$  ( $0.122 \text{ in yr}^{-1}$ ), while the South Point Fault average rate ranged from  $0.01 \text{ cm yr}^{-1}$  ( $0.0039 \text{ in yr}^{-1}$ ) to  $0.05 \text{ cm yr}^{-1}$  ( $0.0197 \text{ in yr}^{-1}$ ). Chronostratigraphic cross-sections also indicate consistent penetration of older strata ( $>2,000 \text{ yr BP}$ ) on the northern or up-thrown side of projected fault traces (Figs. 46-50). However, fault interpretations do not imply the presence of active fault slip, because these relationships can also be explained by regional south dip and/or the presence of a regional scour surface. Further investigation is necessary to determine if these rates are a result of active fault slip.

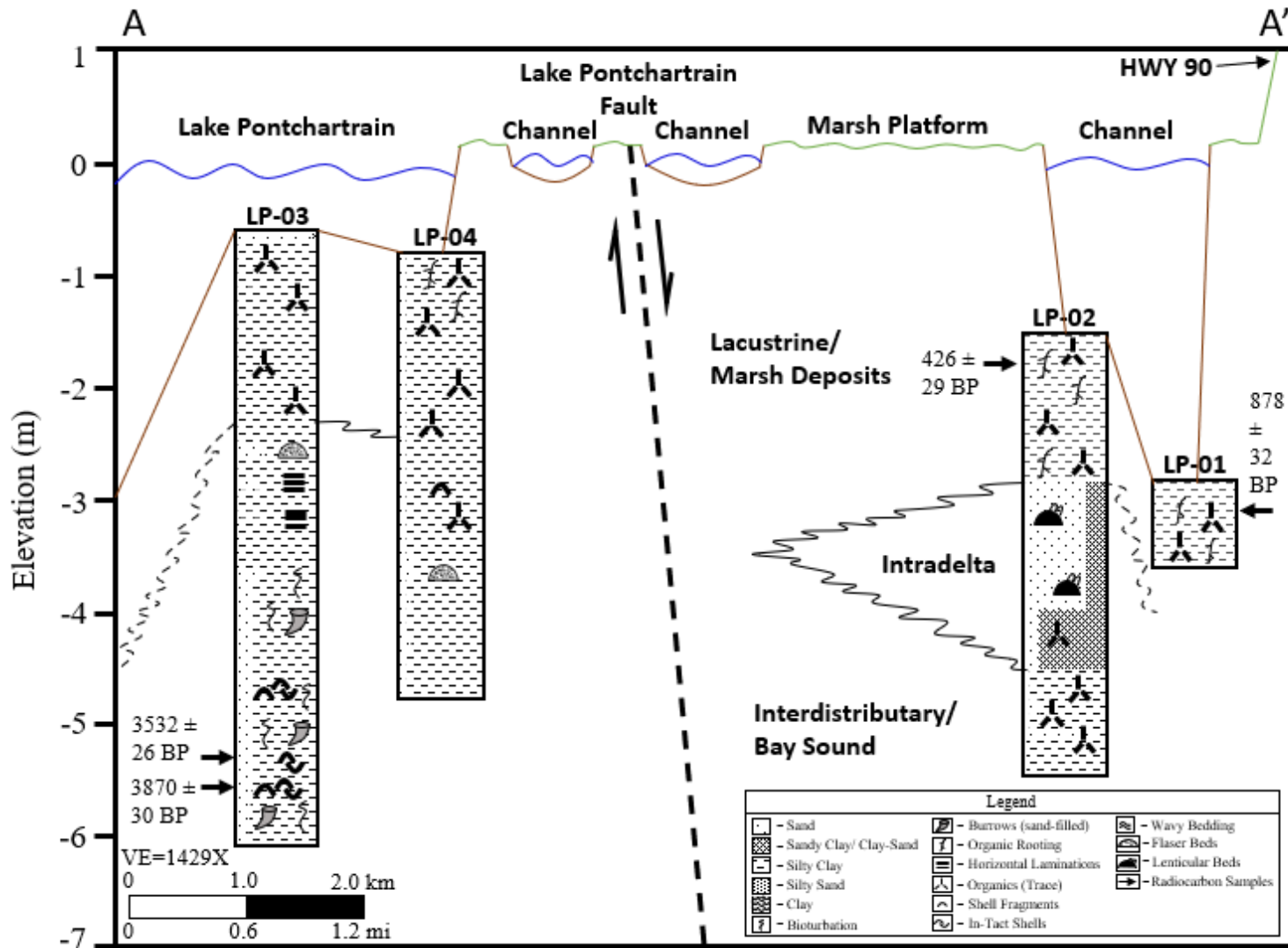


**Figure 38.** Lithostratigraphic cross-section A to A' (location in figure 25). Deeper depth to boundary between Lacustrine/Marsh and Interdistributary/Bay at southern vibrocore consistent with but not proof of recent offset across shallow fault. Radiocarbon sample ages and error estimates are labeled next to the black arrows marking positions of radiocarbon samples. Vertical Exaggeration (VE) is 1429x.

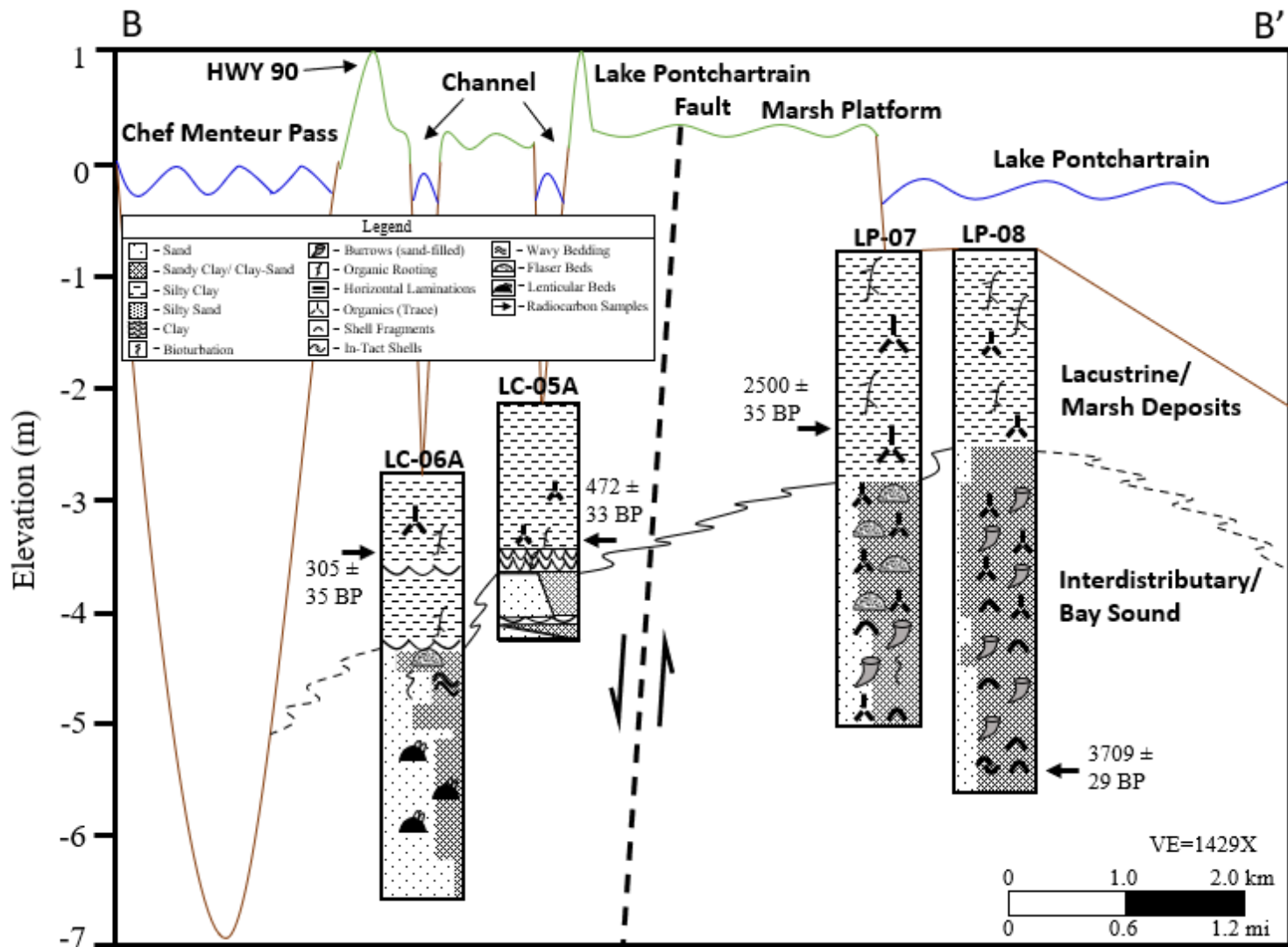


**Figure 39.** Lithostratigraphic cross-section B to B' (location in figure 25). Deeper depth to boundary between Lacustrine/Marsh and Interdistributary/Bay at southern vibracore consistent with but not proof of recent offset across shallow fault. Radiocarbon sample ages and error estimates are labeled next to the black arrows marking positions of radiocarbon samples. VE is 1429x.

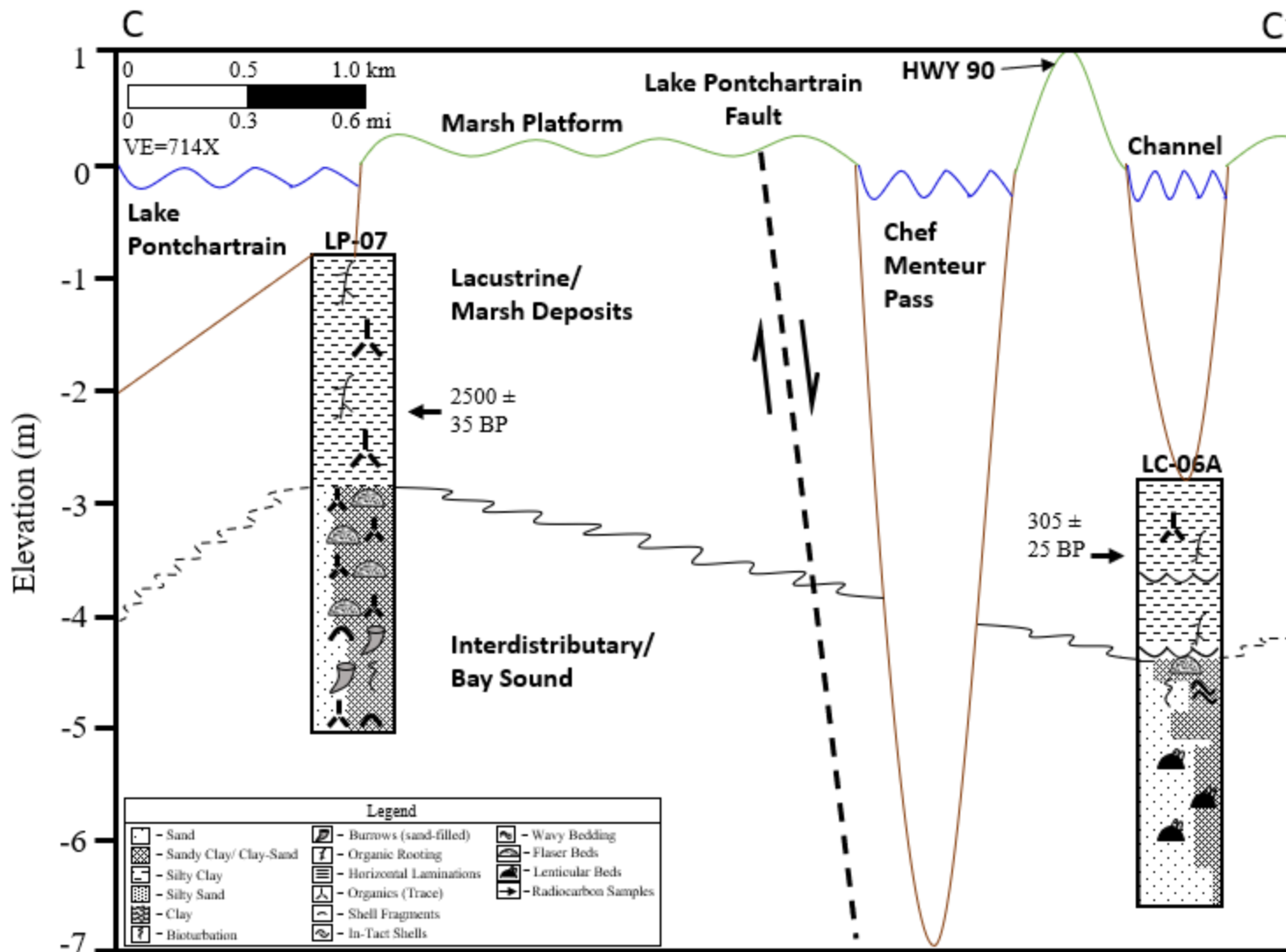


**Figure 40.** Lithostratigraphic cross-section C to C' (location in figure 25). Deeper depth to boundary between Lacustrine/Marsh and Interdistributary/Bay at southern vibracore consistent with but not proof of recent offset across shallow fault. Radiocarbon sample ages and error estimates are labeled next to the black arrows marking positions of radiocarbon samples. VE is 714x.

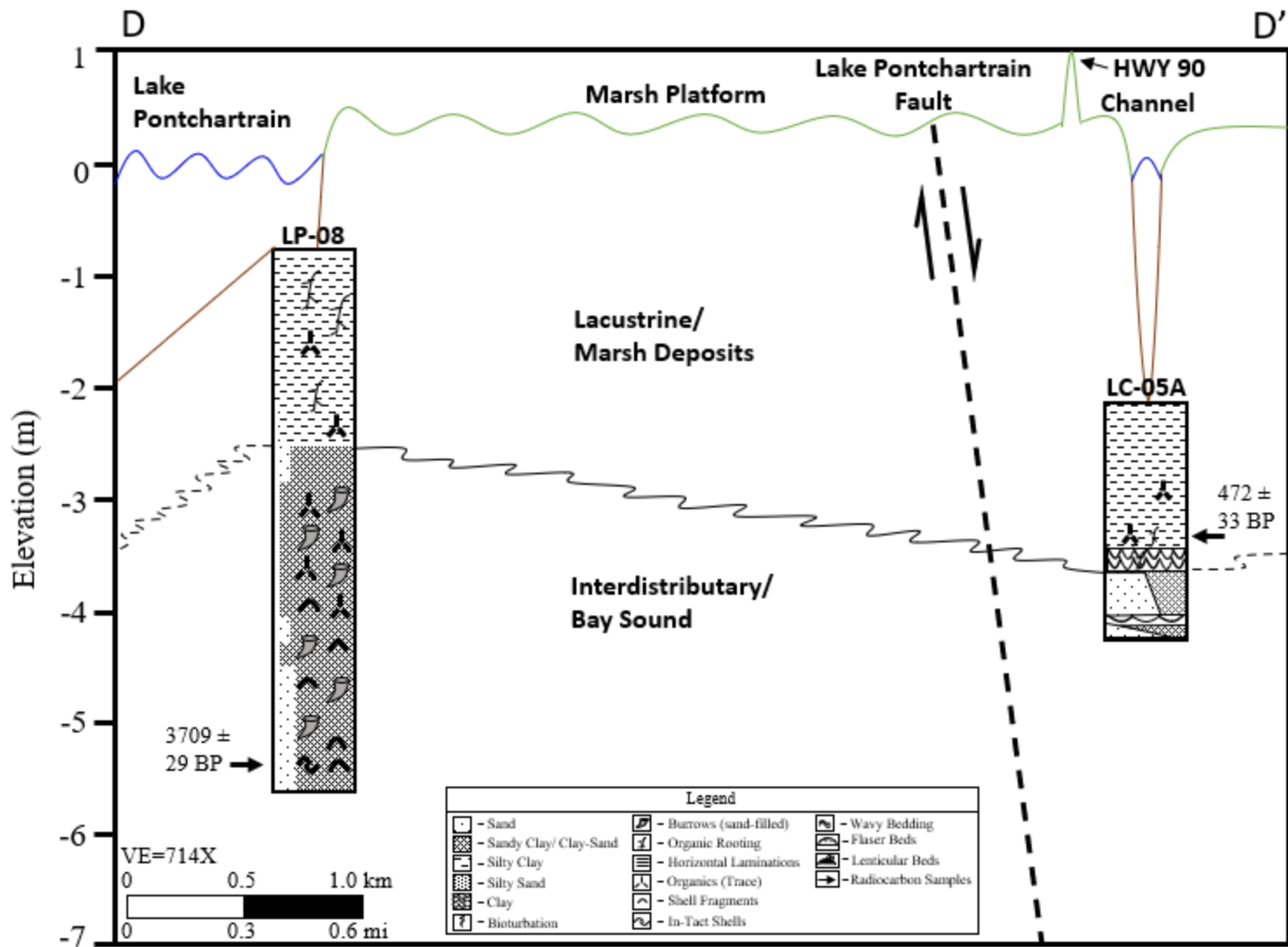


**Figure 41.** Lithostratigraphic cross-section D to D' (location in figure 25). Deeper depth to boundary between Lacustrine/Marsh and Interdistributary/Bay at southern vibracore consistent with but not proof of recent offset across shallow fault. Radiocarbon sample ages and error estimates are labeled next to the black arrows marking positions of radiocarbon samples. VE is 714x.

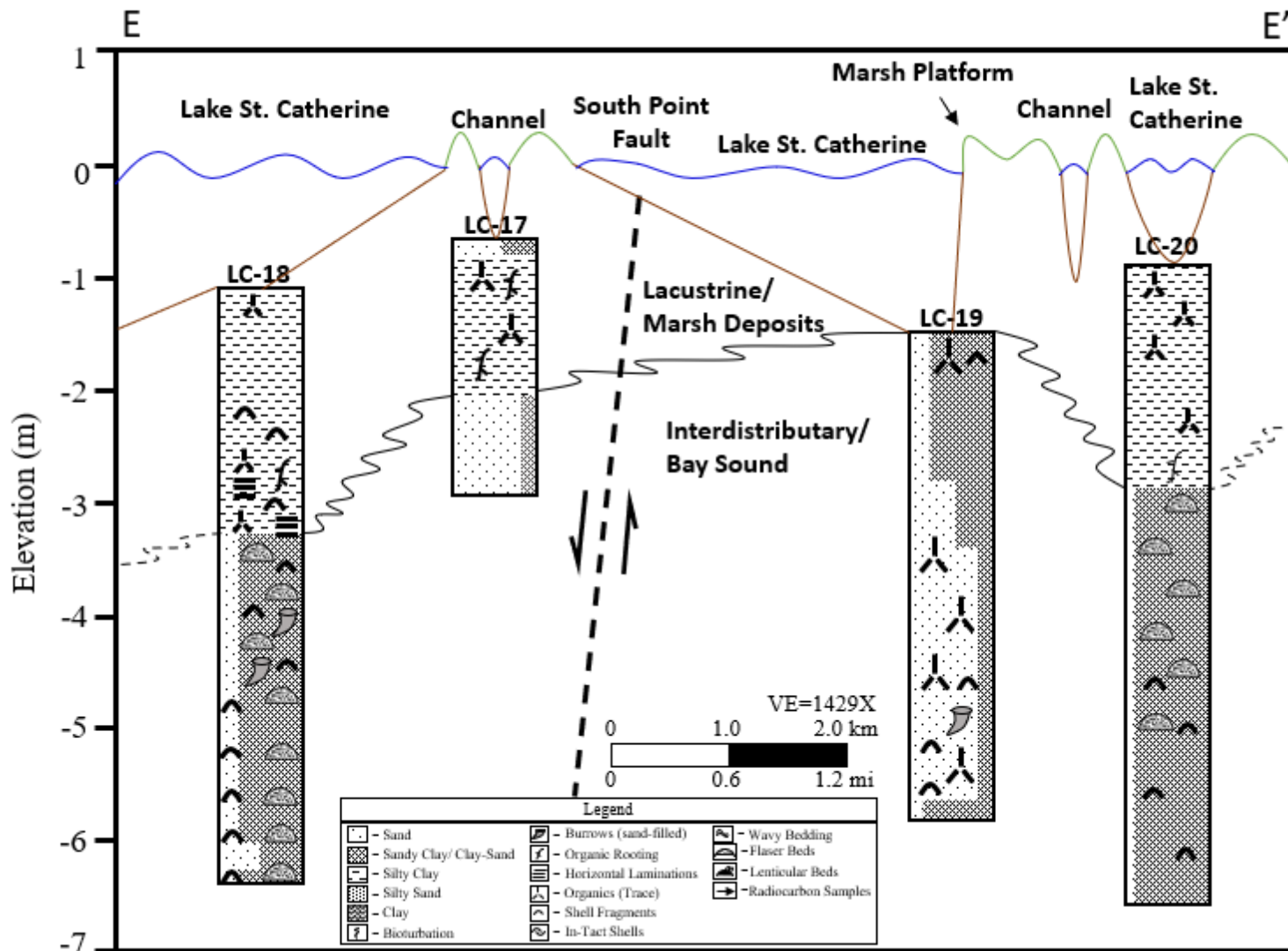


**Figure 42.** Lithostratigraphic cross-section E to E' (location in figure 25). Deeper depth to boundary between Lacustrine/Marsh and Interdistributary/Bay Sound at southern vibracore consistent with but not proof of recent offset across shallow fault. Radiocarbon sample ages and error estimates are labeled next to the black arrows marking positions of radiocarbon samples. VE is 1429x.

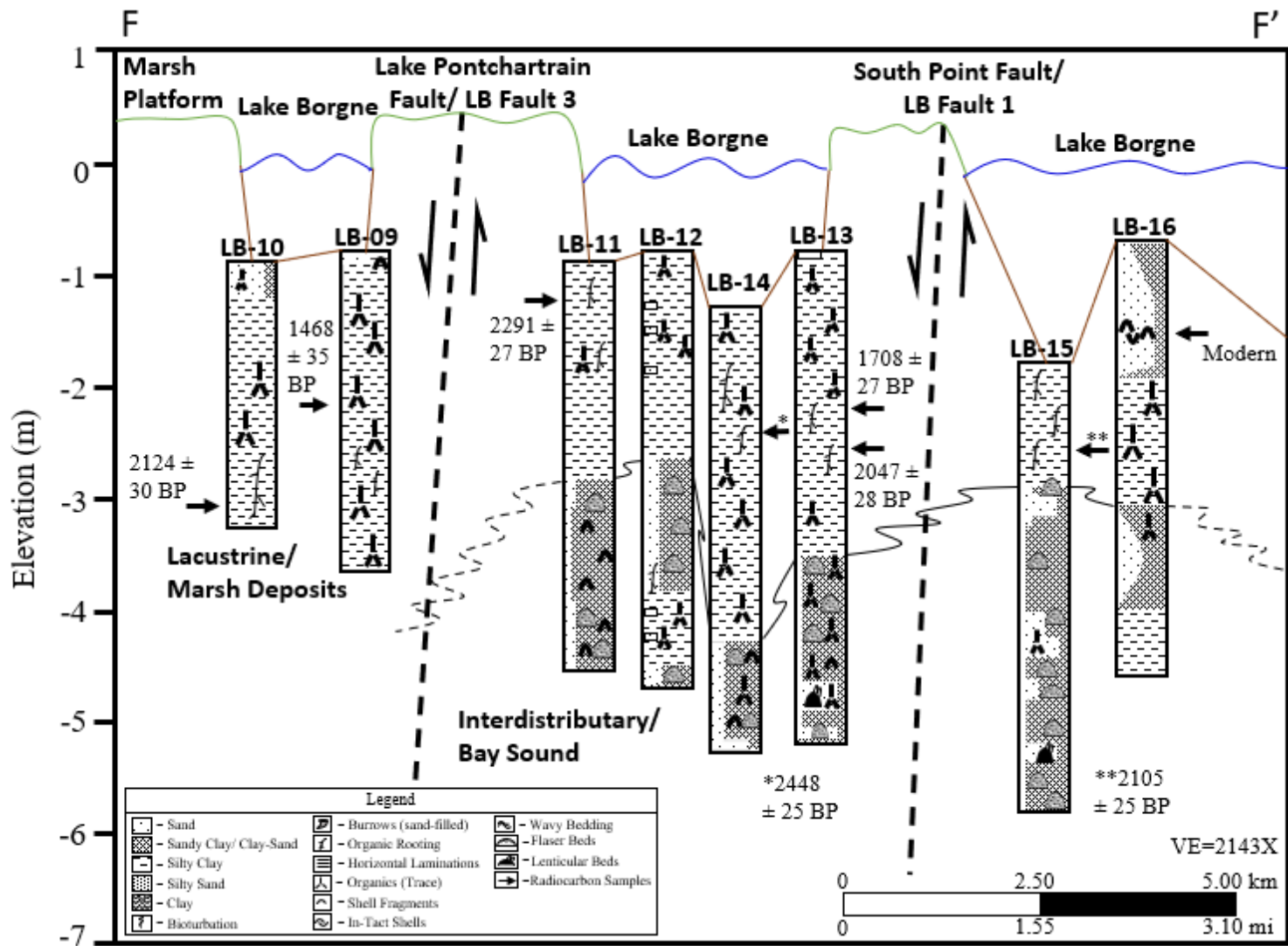


**Figure 43.** Lithostratigraphic cross-section F to F' (location in figure 25). Deeper depth to boundary between Lacustrine/Marsh and Interdistributary/Bay Sound at southern vibracore consistent with but not proof of recent offset across shallow fault. Radiocarbon sample ages and error estimates are labeled next to the black arrows marking positions of radiocarbon samples. VE is 2143x.

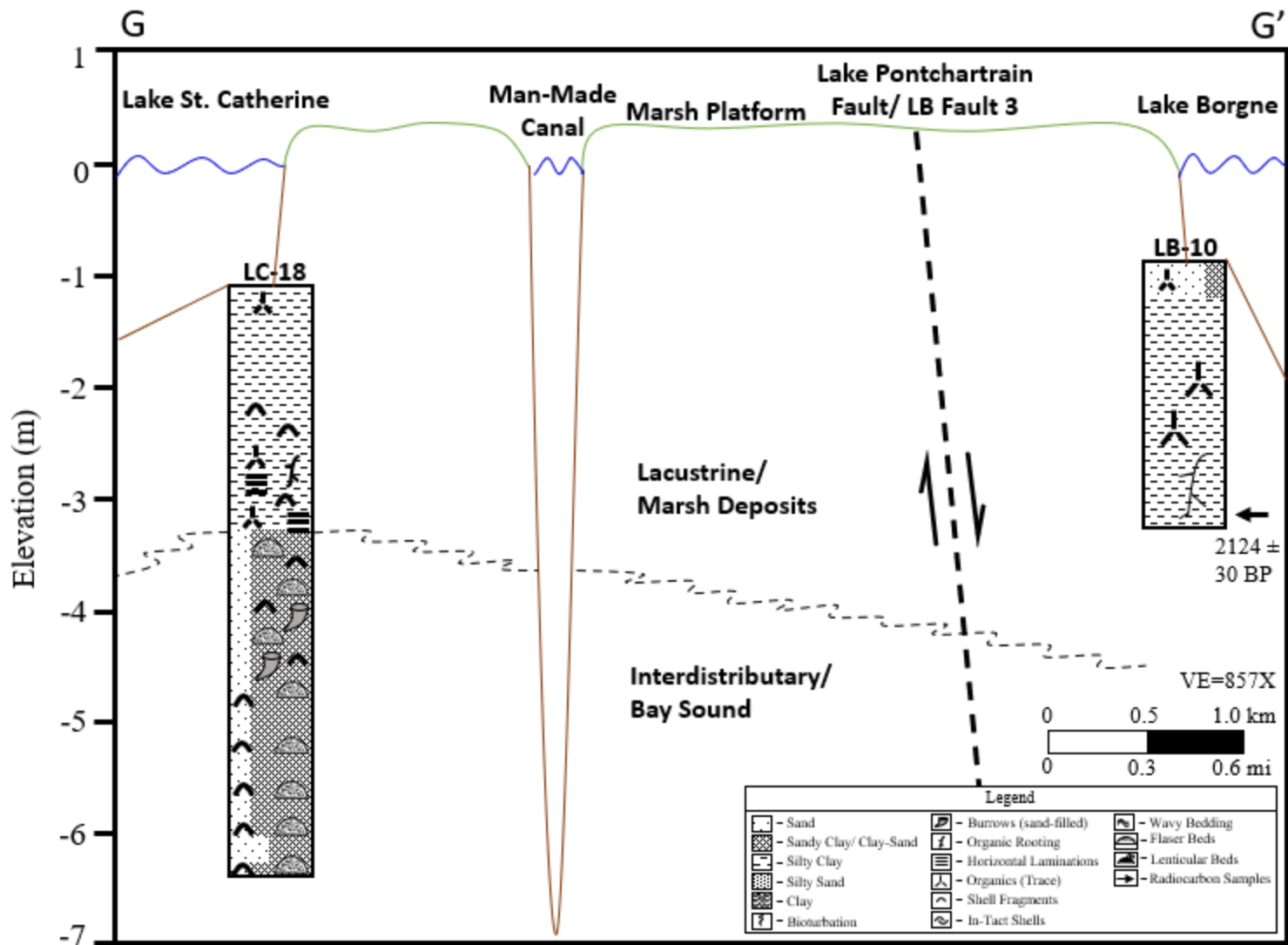


**Figure 44.** Lithostratigraphic cross-section G to G' (location in figure 25). Radiocarbon sample ages and error estimates are labeled next to the black arrows marking positions of radiocarbon samples. VE is 857x.

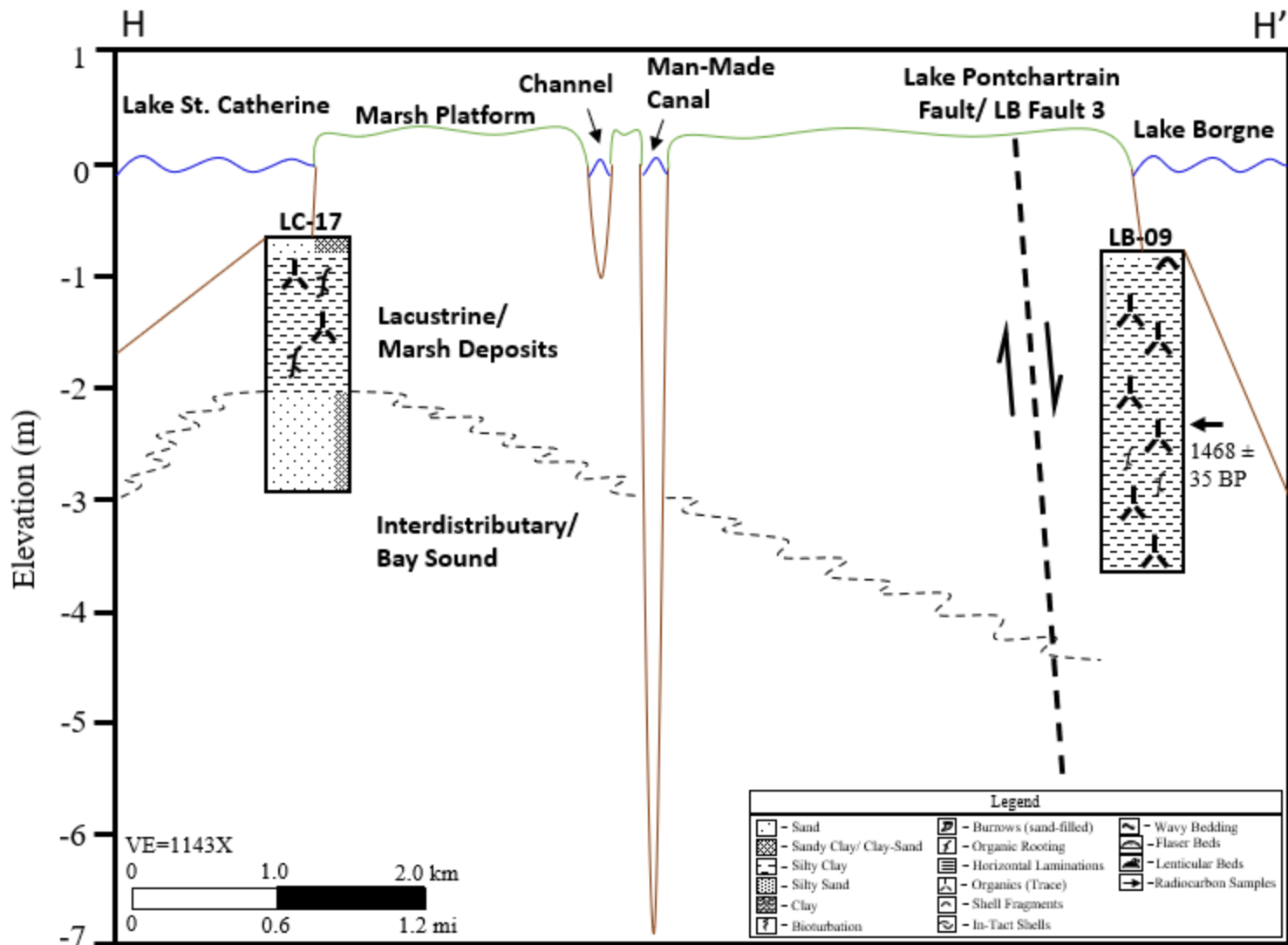


**Figure 45.** Lithostratigraphic cross-section H to H' (location in figure 25). Radiocarbon sample ages and error estimates are labeled next to the black arrows marking positions of radiocarbon samples. VE is 1143x.

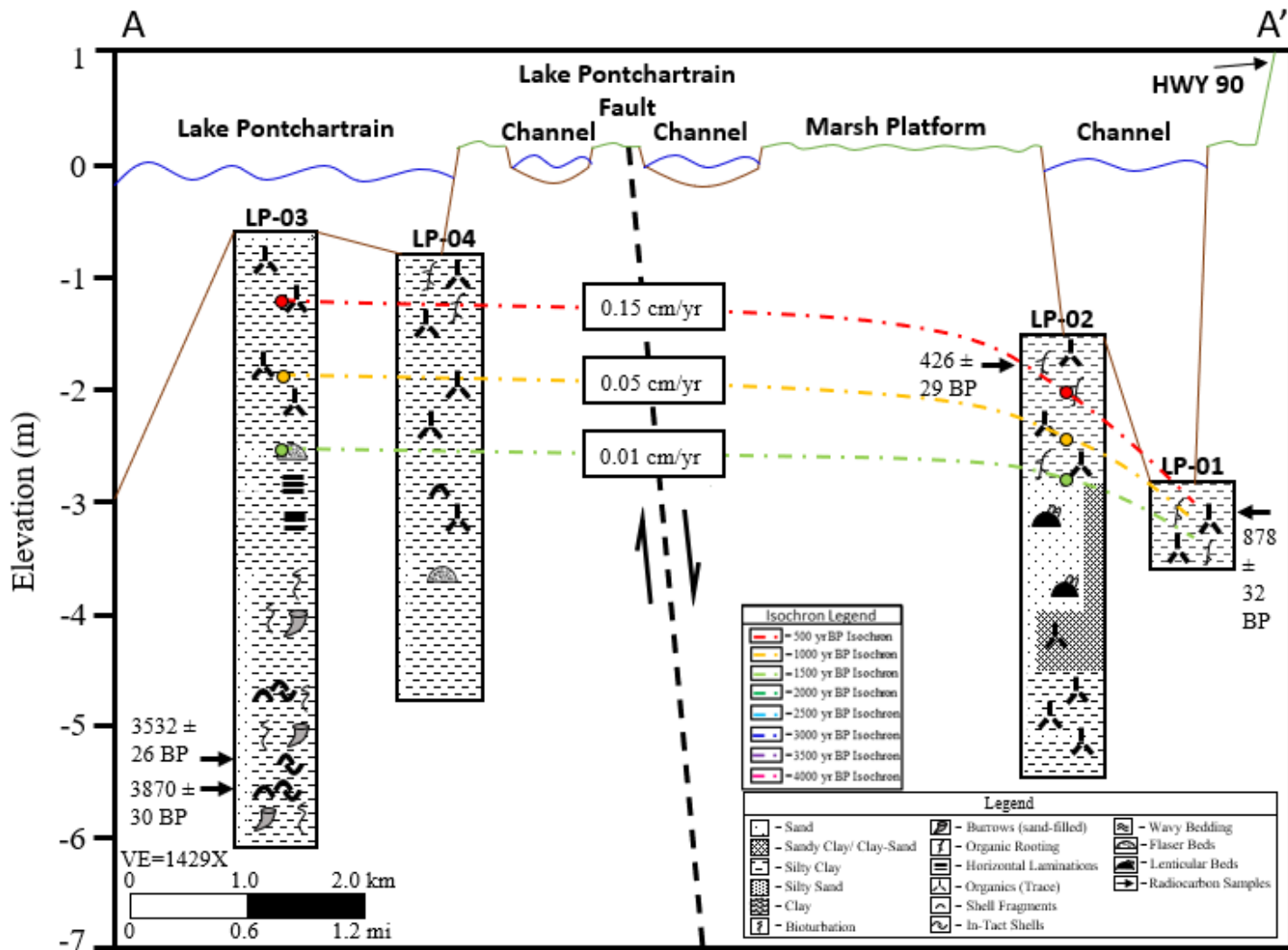


**Figure 46.** Chronostratigraphic cross-section A to A' (location in figure 25). Shallow depth to relatively older sediments in northern vibracore consistent with but not proof of recent offset across shallow fault. Boxes with values indicate the calculated fault displacement rate of that isochron. Radiocarbon sample ages and error estimates are labeled next to the black arrows marking positions of radiocarbon samples. Radiocarbon estimates positions are marked by colored circles according to age of estimate. VE is 1429x.

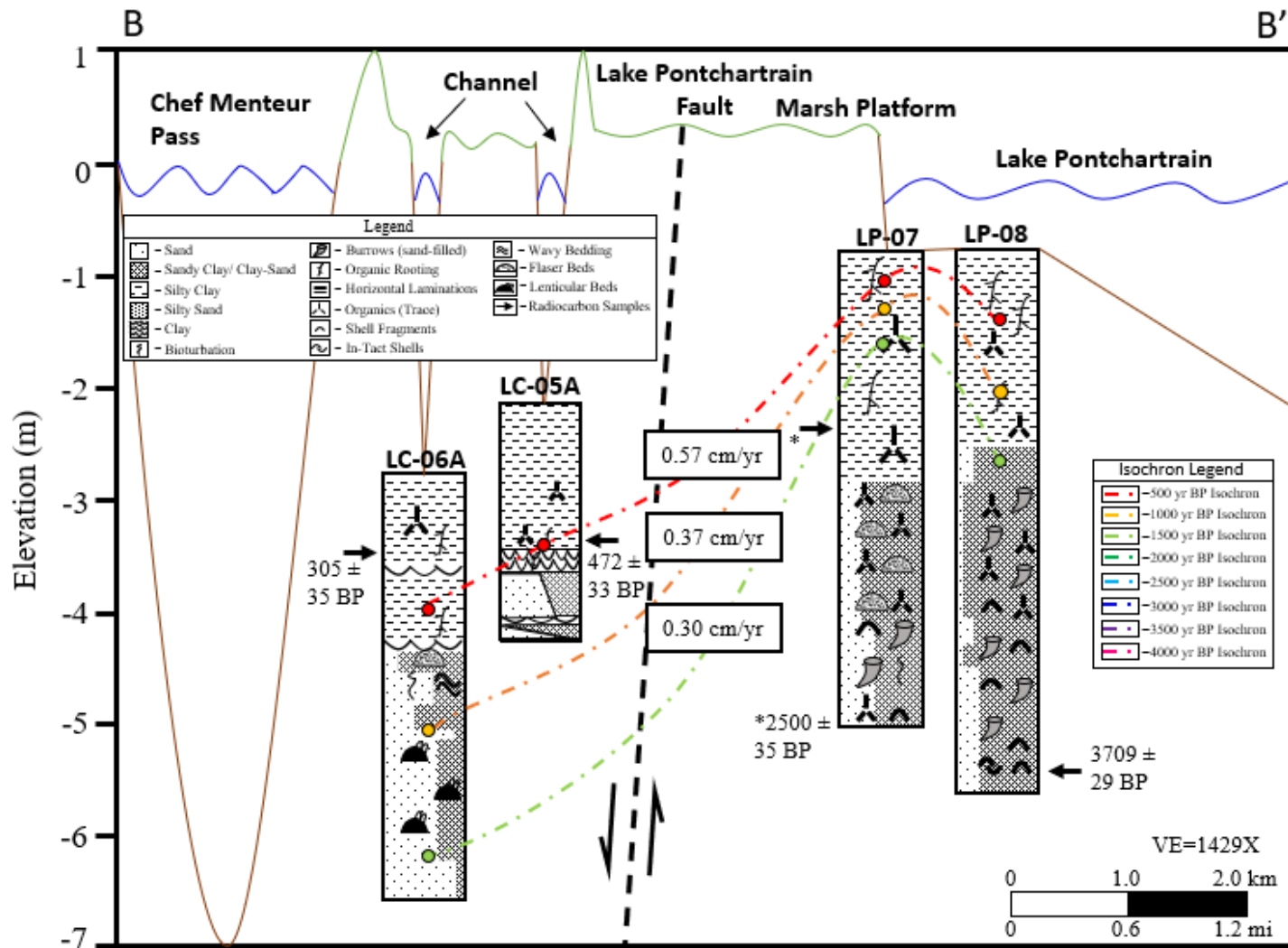


**Figure 47.** Chronostratigraphic cross-section B to B' (location in figure 25). Shallow depth to relatively older sediments in northern vibracore consistent with but not proof of recent offset across shallow fault. Boxes with values indicate the calculated fault displacement rate of that isochron. Radiocarbon sample ages and error estimates are labeled next to the black arrows marking positions of radiocarbon samples. Radiocarbon estimates positions are marked by colored circles according to age of estimate. VE is 1429x.

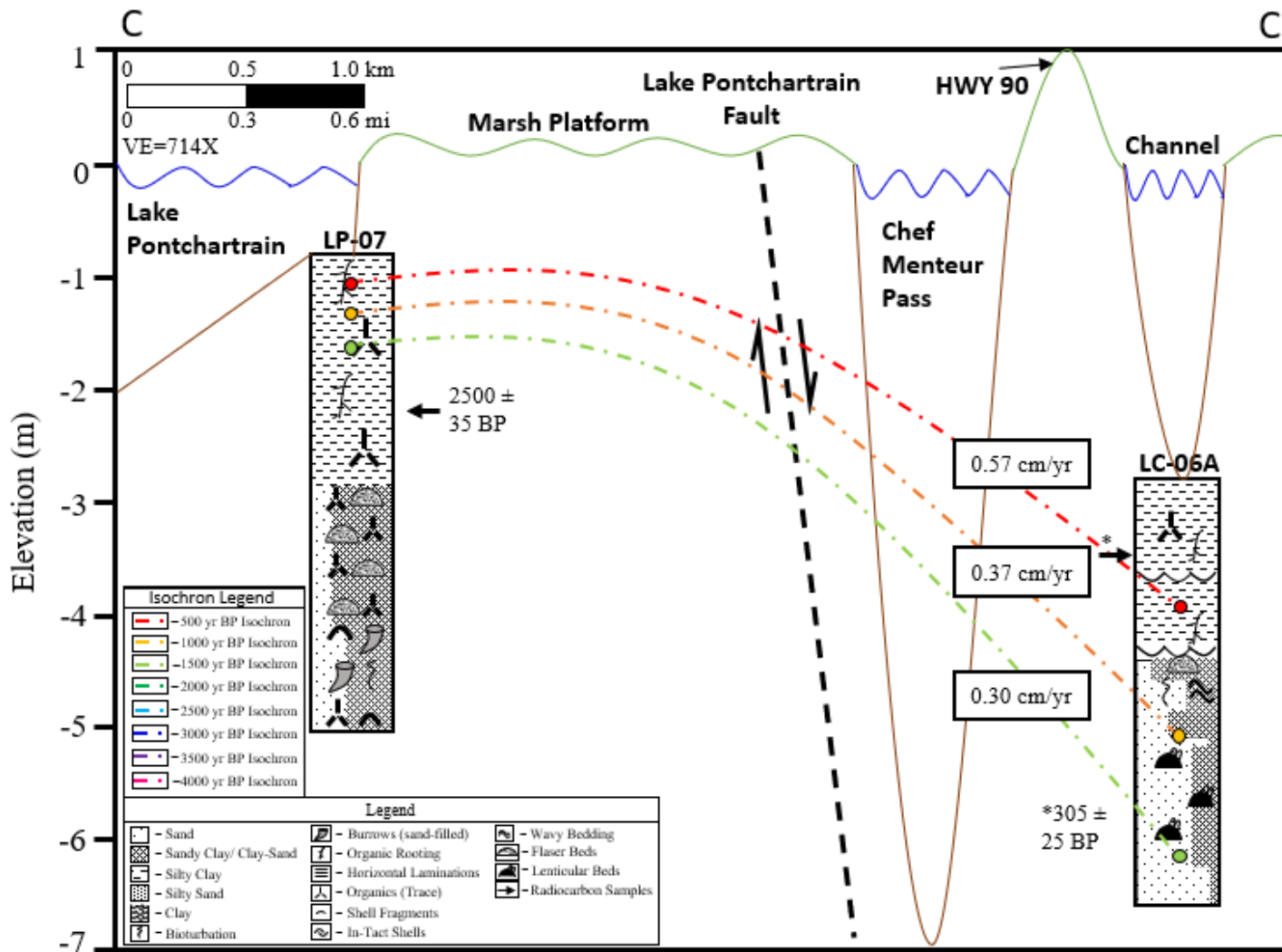


**Figure 48.** Chronostratigraphic cross-section C to C' (location in figure 25). Shallow depth to relatively older sediments in northern vibracore consistent with but not proof of recent offset across shallow fault. Boxes with values indicate the calculated fault displacement rate of that isochron. Radiocarbon sample ages and error estimates are labeled next to the black arrows marking positions of radiocarbon samples. Radiocarbon estimates positions are marked by colored circles according to age of estimate. VE is 714x.

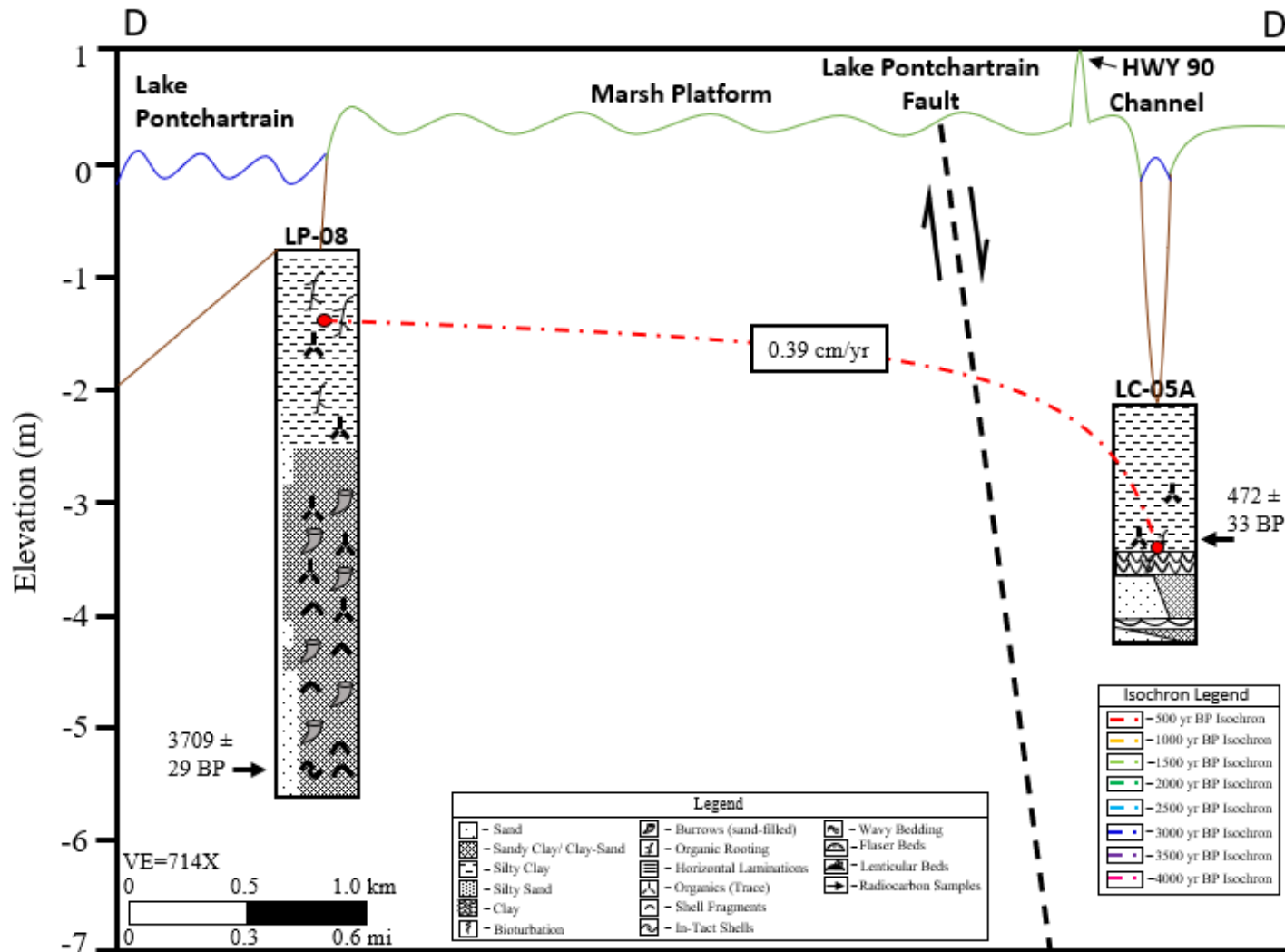


**Figure 49.** Chronostratigraphic cross-section D to D' (location in figure 25). Shallow depth to relatively older sediments in northern vibracore consistent with but not proof of recent offset across shallow fault. Boxes with values indicate the calculated fault displacement rate of that isochron. Radiocarbon sample ages and error estimates are labeled next to the black arrows marking positions of radiocarbon samples. Radiocarbon estimates positions are marked by colored circles according to age of estimate. VE is 714x.



## 4.5 Chirp Seismic Faults

Chirp collection resulted in 50 2-D SEG-Y segments that form 27 lines. These lines span the mappable lateral extent of fault segments of the BRFS and LBFS within Lake Pontchartrain, Lake Borgne, and Chef Menteur Pass (Fig. 28). Appendix B shows the collection information for those lines. These lines were processed with a frequency filter in *IHS Kingdom* and used to assess possible fault displacement in Holocene strata along with determining the depth to the Pleistocene-Holocene contact. Of the 50 SEG-Y lines, 13 show offset in shallow strata due to fault slip including lines 4-13, lines 15-16, line 16.004, and line 17.001. Figure 51 shows Chirp Line 10, which shows clear offset above Late Pleistocene strata as well as a reflection that may be interpreted as the Pleistocene-Holocene contact. A thick black polygon (Fig. 28) depicts the extent of the Chirp seismic grid that was used to create a top structure map of the Pleistocene surface (Fig. 52). Seismic reflections recorded in twt were depth-converted using a velocity of  $1500 \text{ ms}^{-1}$  (EdgeTech, 2015). Roth (1999) used boring logs and shallow seismic to interpret a depth to the Pleistocene surface between 5-12 m (16-39 ft) subsea in the region of the collected seismic from this study. This depth was used to pick the Pleistocene-Holocene contact in the Chirp seismic lines. Roth (1999) also contoured the Pleistocene surface and discovered a Pleistocene aged channel network (Fig. 53). The bottom of the Pleistocene paleochannel of the Amite River identified by Roth (1999) would form a very similar syncline structure as seen in the Pleistocene structure map created in this study.

Vibracore radiocarbon dates and isochron estimates were imported into *IHS Kingdom* and only the South Point Fault had adequate available Chirp data with available radiocarbon dates in order to estimate a rate of offset that may be a result of fault slip. Chirp Line 12 was overlain by vibracore “VC-LP-03” in figure 54. The bold reflection in the Chirp seismic line directly

correlates with an approximate isochron estimate of 2000 yr BP. The offset of the reflection across the fault is approximately 0.0072 s twt in the Chirp seismic line, which yields an offset rate of 0.035 cm yr<sup>-1</sup>. This rate is an order of magnitude smaller than the rates of offset in vibracore cross-sections. Chirp seismic lines, such as Line 12, show offset into the early Holocene strata, despite a lack of available age-constrained lithology to calculate rates of offset in the Holocene. The goal was to establish rates and correlate offset in the land bridge to fault motion, but with a lack of age-constrained lithology only presence of faulting may be identified.

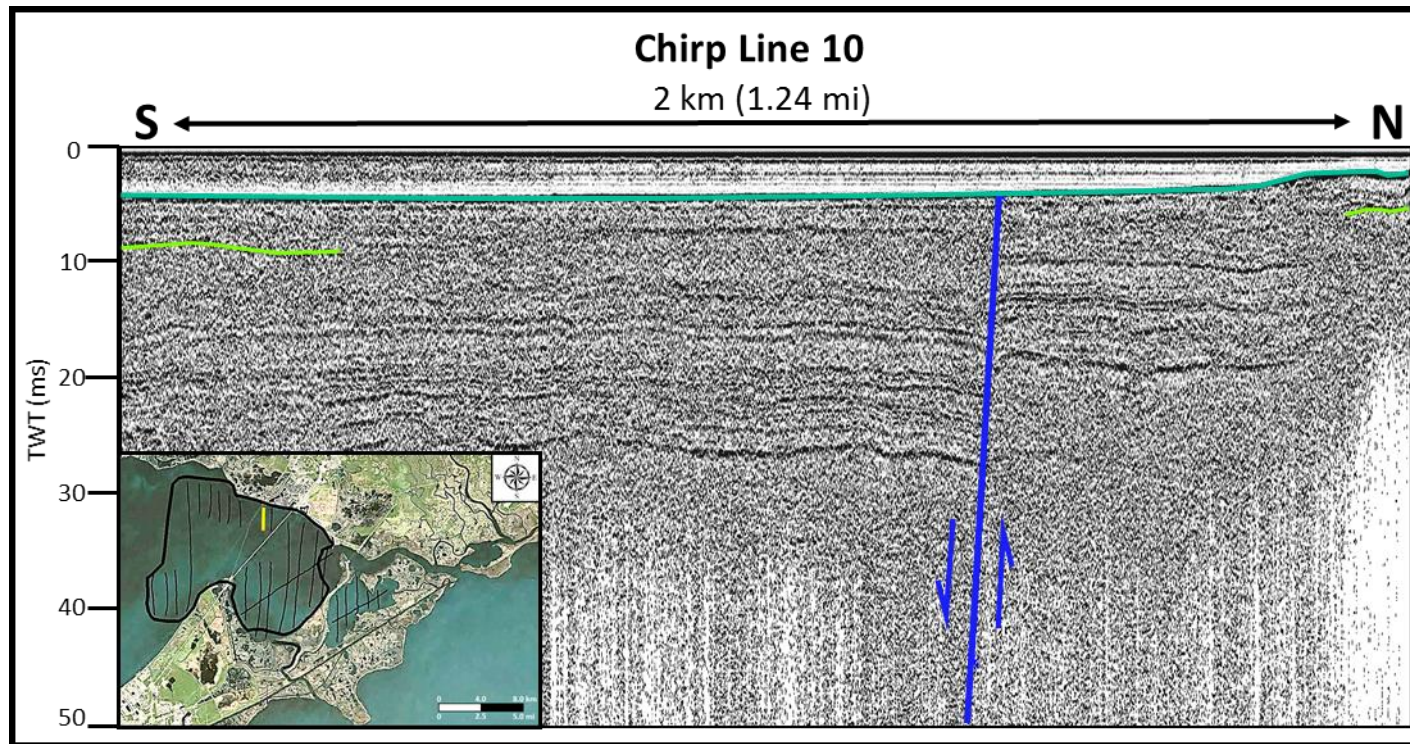


**Figure 51.** Noticeable offset of shallow stratigraphy is apparent in Chirp seismic lines, such as Chirp Line 10 shown above. The offset is caused by the motion of the Goose Point Fault (dark blue line). The teal line delineates water bottom in the Chirp seismic. The Pleistocene-Holocene contact is labeled by the lime green colored line and was interpreted from depth estimates made by Roth (1999). The location of the seismic line (yellow line) is shown in the reference map in the lower left corner of the figure.

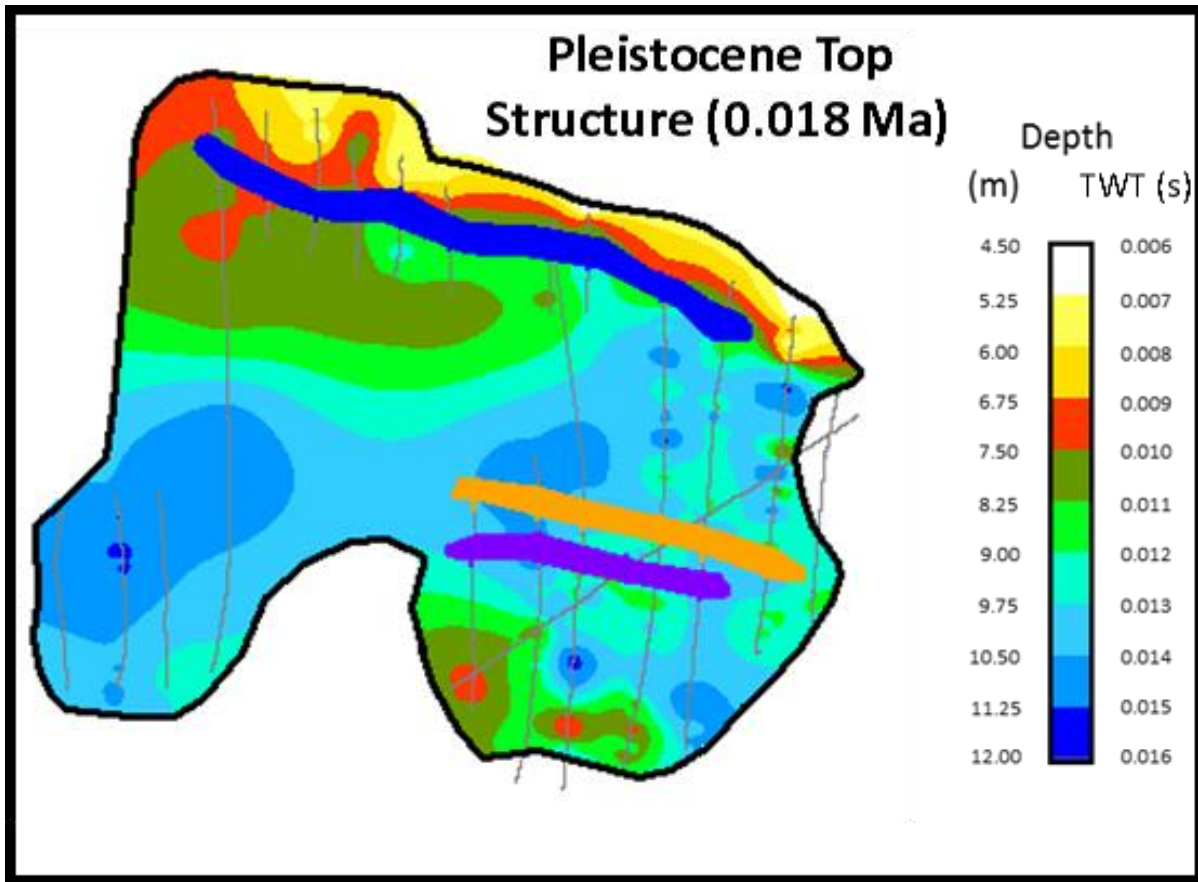


**Figure 52.** A twt structure map of the Pleistocene surface was created in *IHS Kingdom*. The blue, orange, and purple polygons represent anomalies found in the Chirp seismic interpreted as possible fault displacement. The blue polygon is along the same fault trace as the Goose Point Fault and the orange polygon is along the same fault trace as the South Point Fault. The purple polygon is a newly identified fault segment.

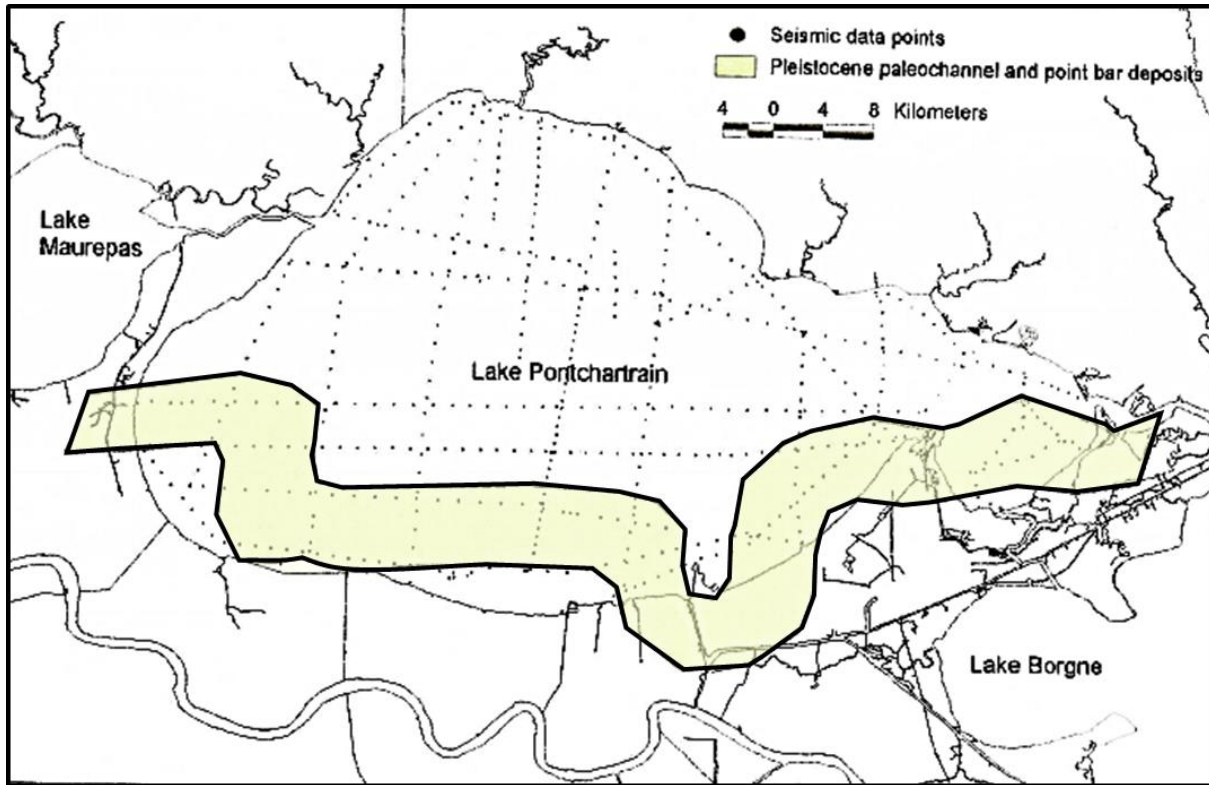


**Figure 53.** Map of the Amite River paleochannel and point bar deposits during the Pleistocene by Roth (1999). The location of this paleochannel is very similar to the areas of greater depth in twt on the Chirp Pleistocene structure map in figure 52.

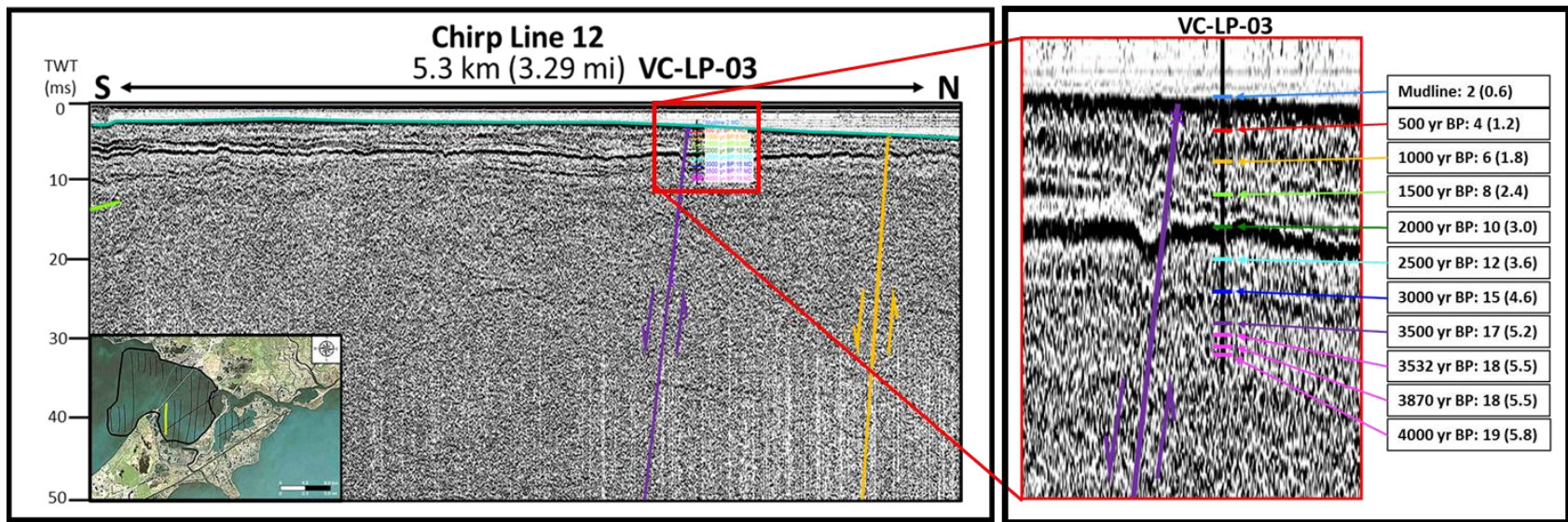


**Figure 54.** This Chirp seismic line shows little offset and slumping of the shallow stratigraphy. The inset map shows an enhanced view of the South Point Fault and values listed for core VC-LP-03 include the isochron or radiocarbon sample age and the measured depth in ft (m). The bold reflection correlates with vibracore VC-LP-03 to an isochron estimate of approximately 2000 yr BP. The amount of offset on the down-thrown side of the fault corresponds to approximately 0.001 s twt or 0.75 m (2.46 ft) of offset during the 2 ka timespan. The purple is the South Point Fault. The orange labeled line is a possible fault segment that continues through the Chirp data, but is in more gaseous sediments, so it is more difficult to accurately map.

## ***4.6 Aerial Imagery and Lidar***

Surface expressions in the form of stream alignment and fault scarps are visible in the study area. Figure 55 shows schematics of the associated surface expressions due to active fault displacement in the Holocene. A map of the study area shows the locations of visible surface expressions (Fig. 56). A closer view of Chef Menteur Pass (Fig. 56) depicts an example of stream alignment and other surface expressions defined by Gagliano et al. (2003). The marsh, however, remains relatively stable on the up-thrown side of the surface traces of the faults, similar to the results by Frank (2016). Lopez et al. (1997) also identified evidence of active fault slip in the Highway 11 Bridge offset, the Norfolk-Southern Railroad offset, and a series of earthquakes that have occurred in recent years. These locations are also marked in figure 5. In the case of land loss, the land bridge has experienced visible land loss of the marsh wetland in a map (Fig. 57) showing land loss between 1932-2015 by Couvillion et al. (2016). A time lapse using aerial imagery of the land bridge during the past several decades shows noticeable land loss in the areas located near surface fault traces (Fig. 58). Direct land loss as a result of the faults of this study cannot be quantified until the entire lateral extent of these faults have been mapped.

The Lidar data indicates changes in elevation of approximately 0.25 m (0.82 ft) in both the 2003 and 2018 datasets along the proposed surface traces of the faults (Figs. 59-62). Lidar was used extensively to map the extent of the BRFS in the region of Baton Rouge and Denham Springs (McCulloh, 2008; McCulloh and Heinrich, 2012). The 2003 Lidar data (Figs. 59-60) shows a clear distinction between the greenish-blue colors on the down-thrown side of the projected fault trace of the South Point Fault indicating lower elevations compared to the yellowish-orange colors on the up-thrown side of the fault trace indicating higher elevations.

This trend continues across the land bridge and provides evidence that the South Point Fault continues through the EOLB. The same trend occurs in the Lake Pontchartrain Fault to the South, although the change in elevation appears to be less. The 2018 data (Figs. 61-62) has very similar results with visible changes in elevation along the two fault traces. Therefore, Holocene geomorphology suggests some fault segments are active.

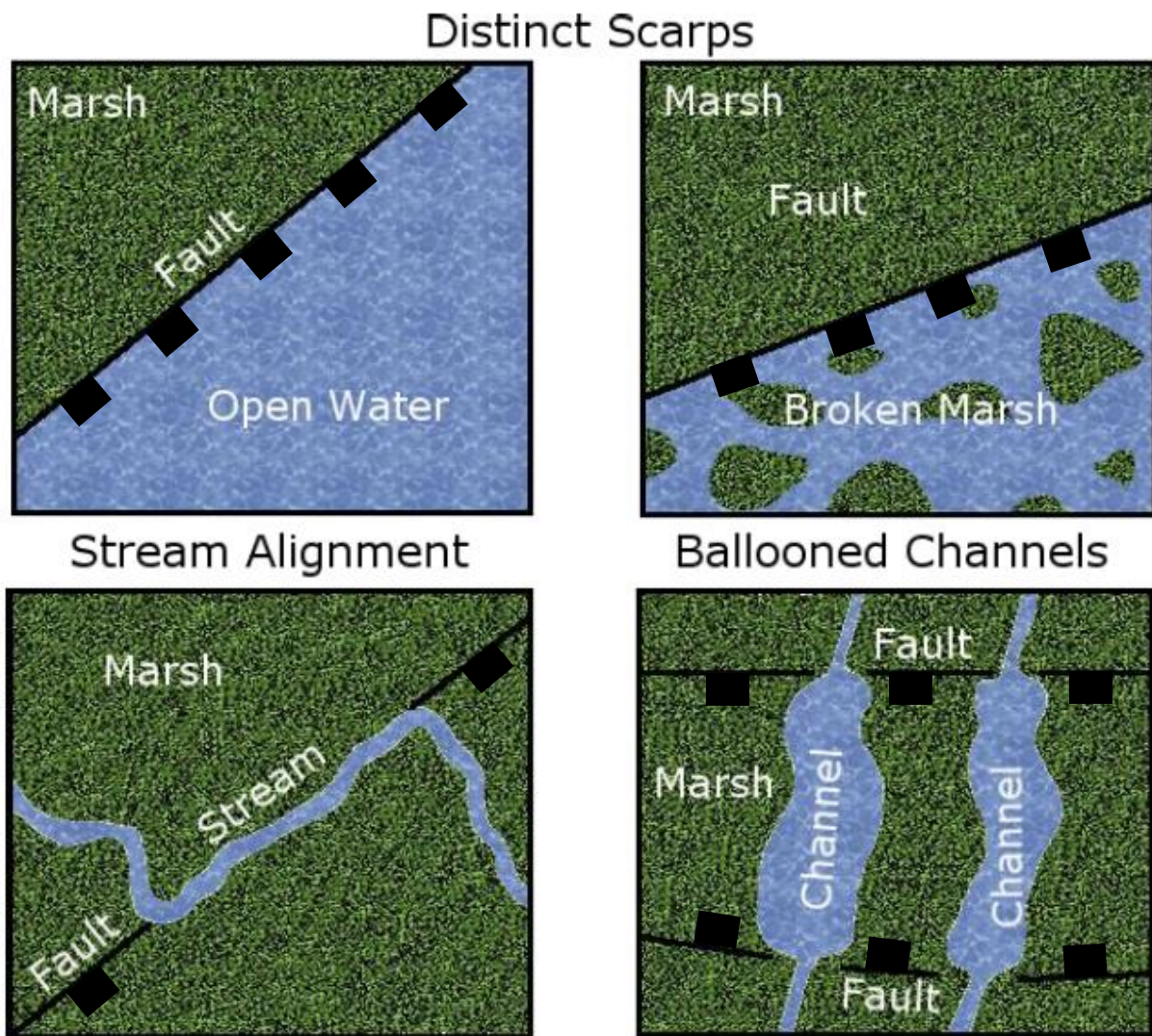


**Figure 55.** These schematic maps show the four main examples of surface expressions due to fault slip, according to Gagliano et al. (2003). Gagliano et al. (2003) suggested down-thrown fault blocks may be identified by broken marsh (top left), open water (top right), stream alignment (bottom left), or ballooned channels (bottom right).

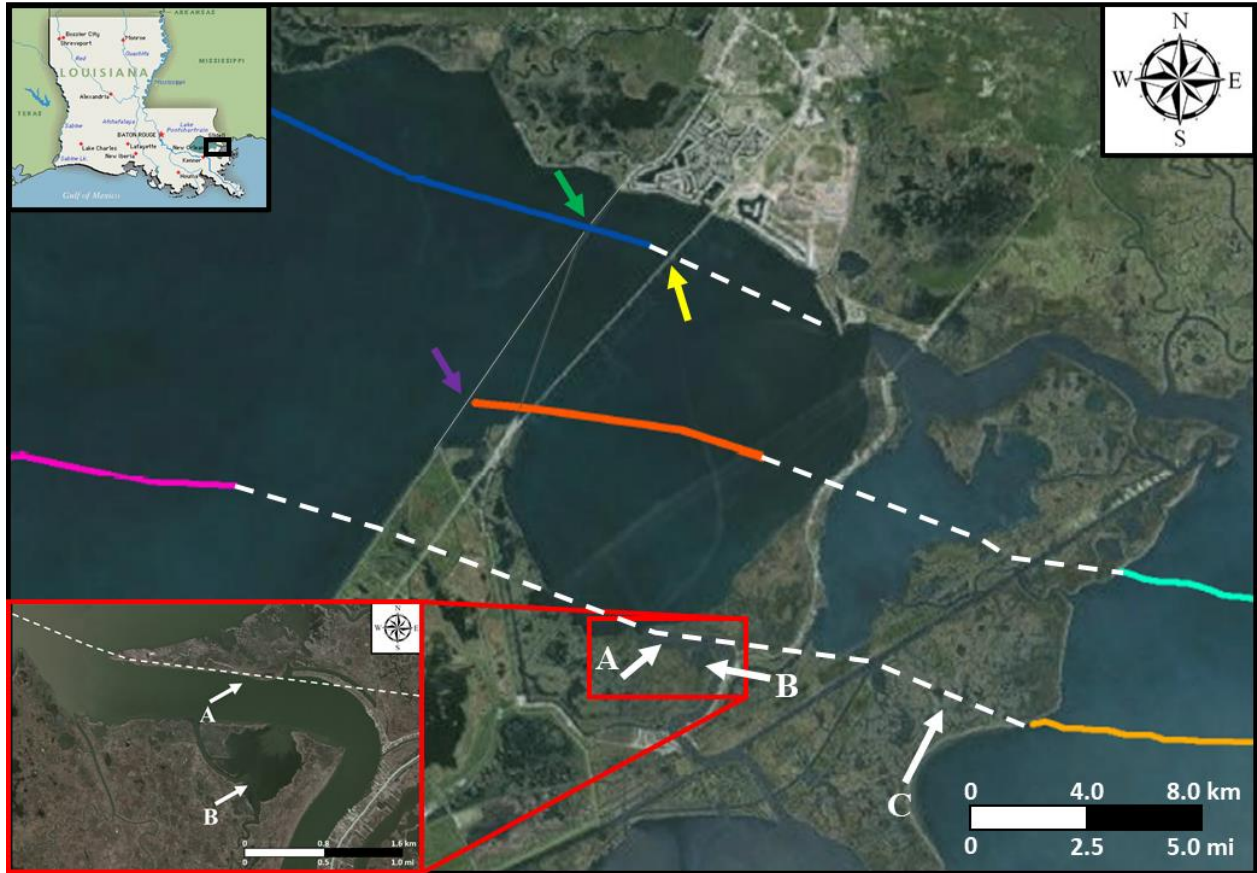


**Figure 56.** Map showing the projected surface traces of faults (colored lines are identified faults and white dashed lines are proposed fault traces from Lake Pontchartrain to Lake Borgne) and evidence of fault-induced surface expressions defined by Gagliano et al. (2003). Colored arrows mark the positions of infrastructure offset measurements, collected by Lopez (1991) and Lopez et al. (1998), in the Norfolk-Southern Railroad (purple arrow), Highway 11 Bridge (green arrow), and I-10 Bridge (yellow arrow). At Site A, the Chef Menteur Pass tidal inlet shows similar traits to an example of stream alignment by Gagliano et al. (2003) as well as a distinct scarp with open water on the down-thrown side of the fault trace. Site B shows the location of a ballooned channel. Site C identifies a distinct scarp with broken marsh along the down-thrown side of the projected surface trace of the Lake Pontchartrain Fault into Lake Borgne.

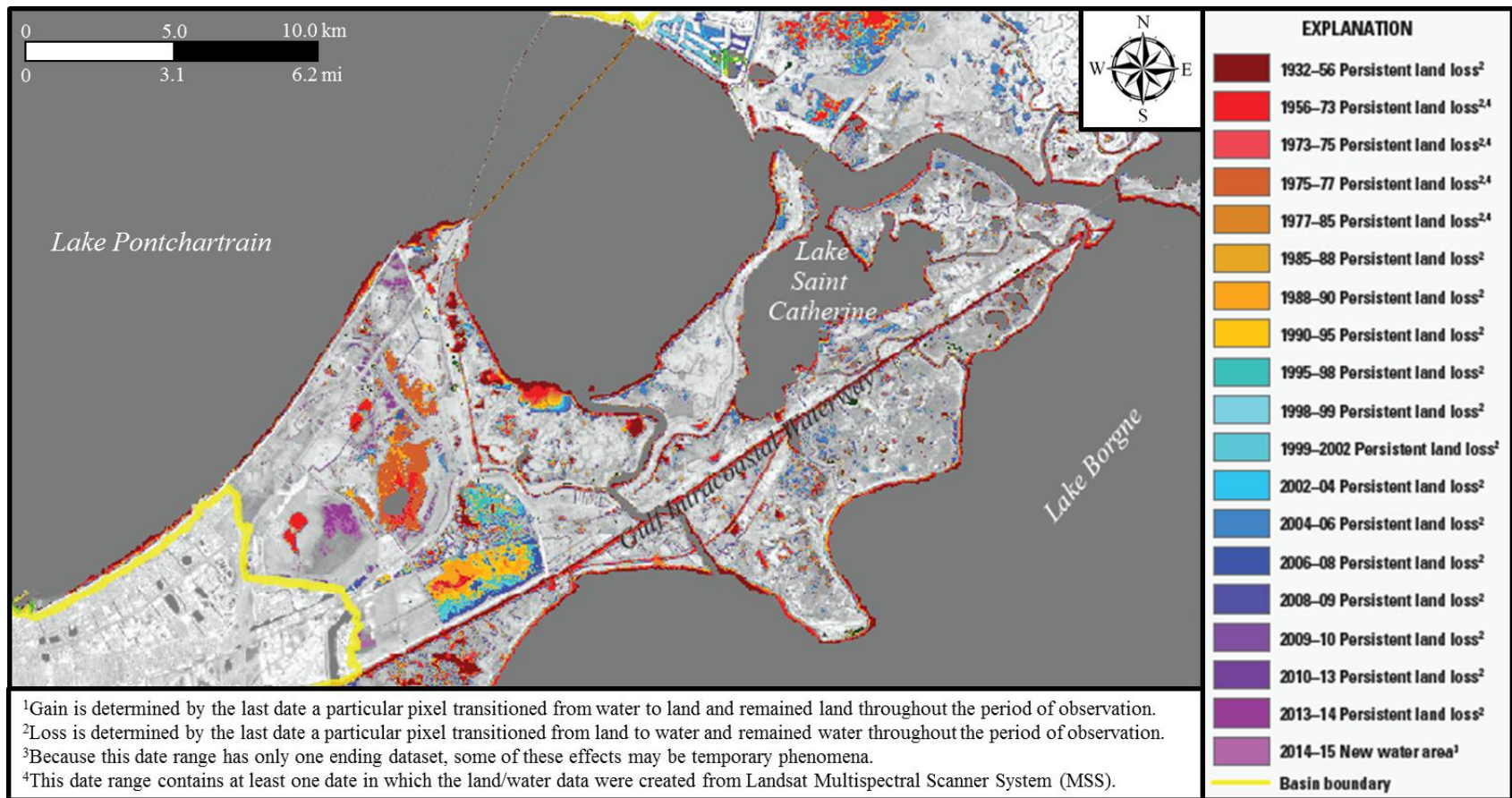


**Figure 57.** Map of persistent land loss within the study area from 1932-2015 by Couvillion et al. (2016). Mapped areas of persistent land loss allow for comparison of aerial imagery to identify coastal wetland loss that may be a result of fault slip of the BRFS during the same period (1932-2015).

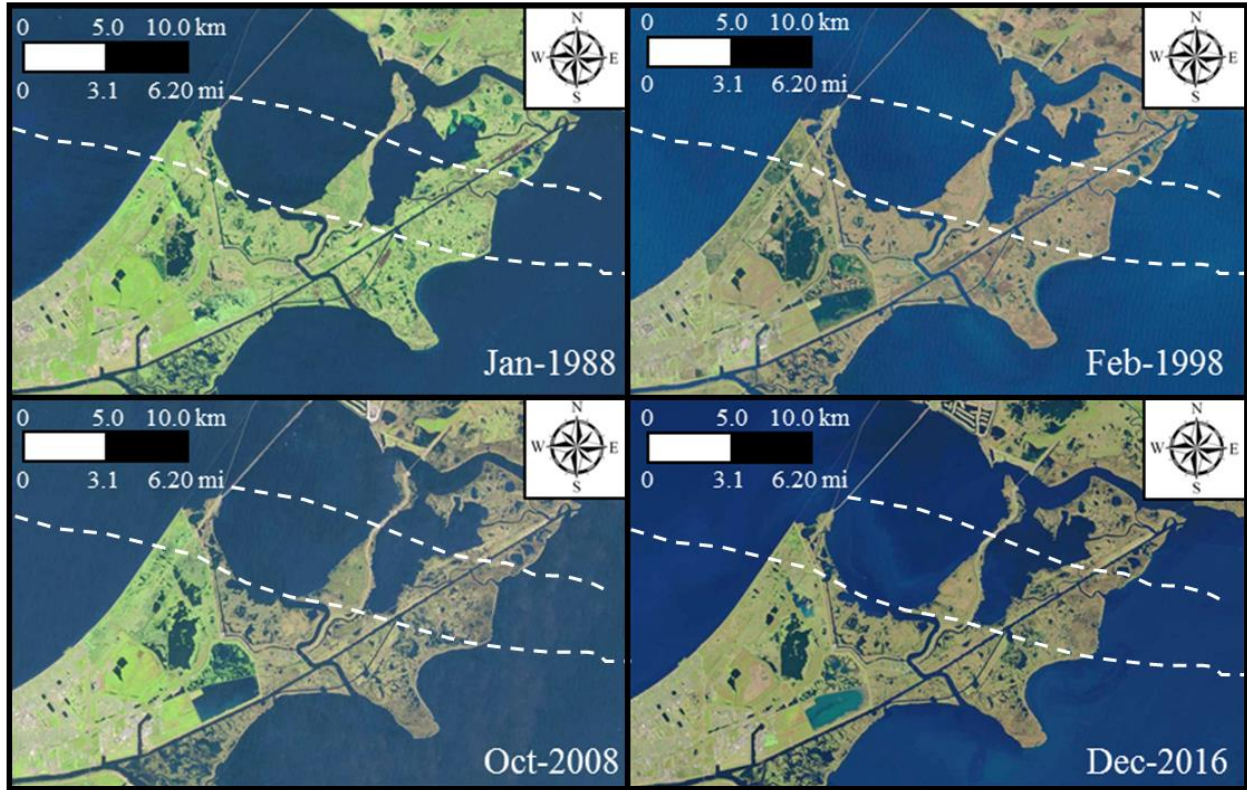


**Figure 58.** Images showing geomorphology of the land bridge from 1988-2016 using satellite imagery collected by USGS LandSat Look Viewer. These images indicate that there was stable marsh across much of the land bridge until sometime between 1988-2008 (likely Hurricane Katrina), followed by a brief period of broken marsh and open water. As the images approach December 2016, the marsh appears to be relatively stable compared to earlier time frames, despite some presence of broken marsh and open water near the locations of the surface traces of faults in the study area. Also, note the increase in presence of open water along the down-thrown side of the Lake Pontchartrain Fault trace at Chef Menteur Pass.

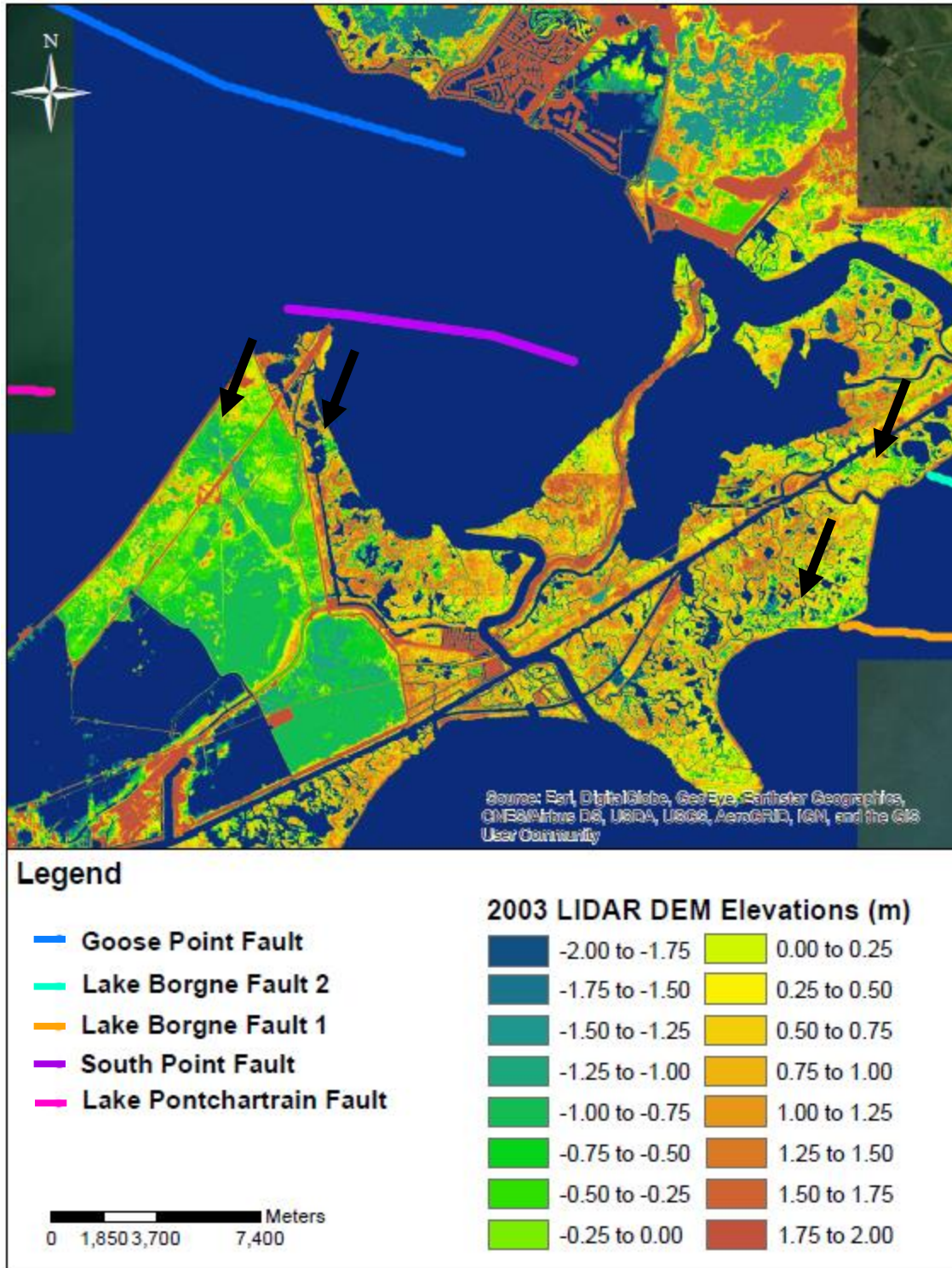


**Figure 59.** Lidar-derived digital elevation model (DEM) of the EOLB data from the 2003 Louisiana Statewide Atlas Project (from Cunningham et al, 2004). Data were symbolized at 0.25 m (0.82 ft) intervals to identify variations in the elevation of the geomorphology across the Land Bridge. Note the change from higher elevations on north to lower elevations towards the south at each of the black arrows. This change occurs along the projected surface traces of the faults, which seem to continue at least into the land bridge, if not through it completely.

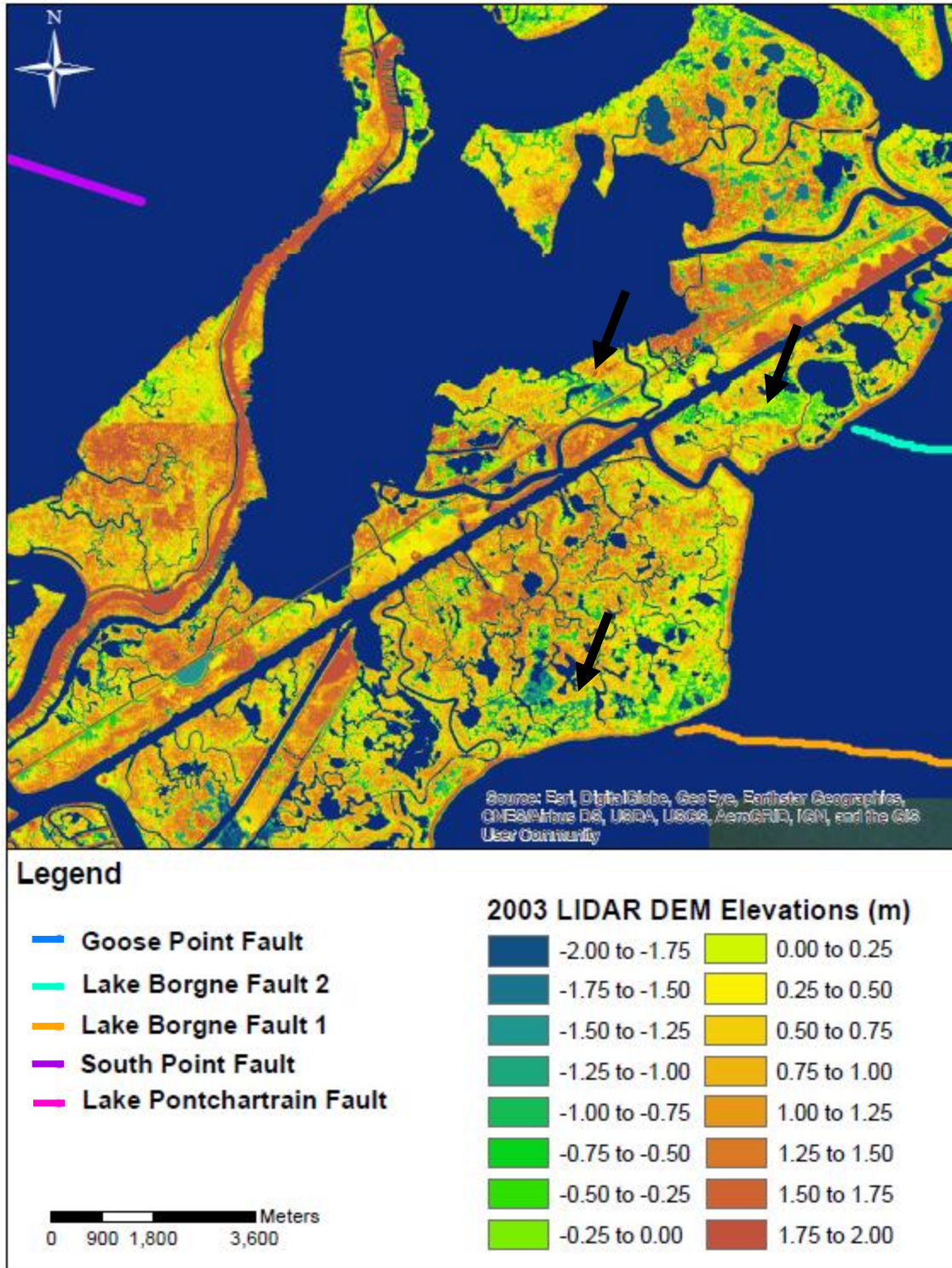


**Figure 60.** Enhanced view of the 2003 Louisiana Statewide Atlas DEM data (from Cunningham et al., 2004). Data were symbolized at 0.25 m (0.82 ft) intervals to identify variations in the elevation of the geomorphology across the Land Bridge. Note the change from higher elevations on north to lower elevations towards the south at each of the black arrows. This change occurs along the projected surface traces of the faults, which seem to continue at least into the land bridge, if not through it completely.

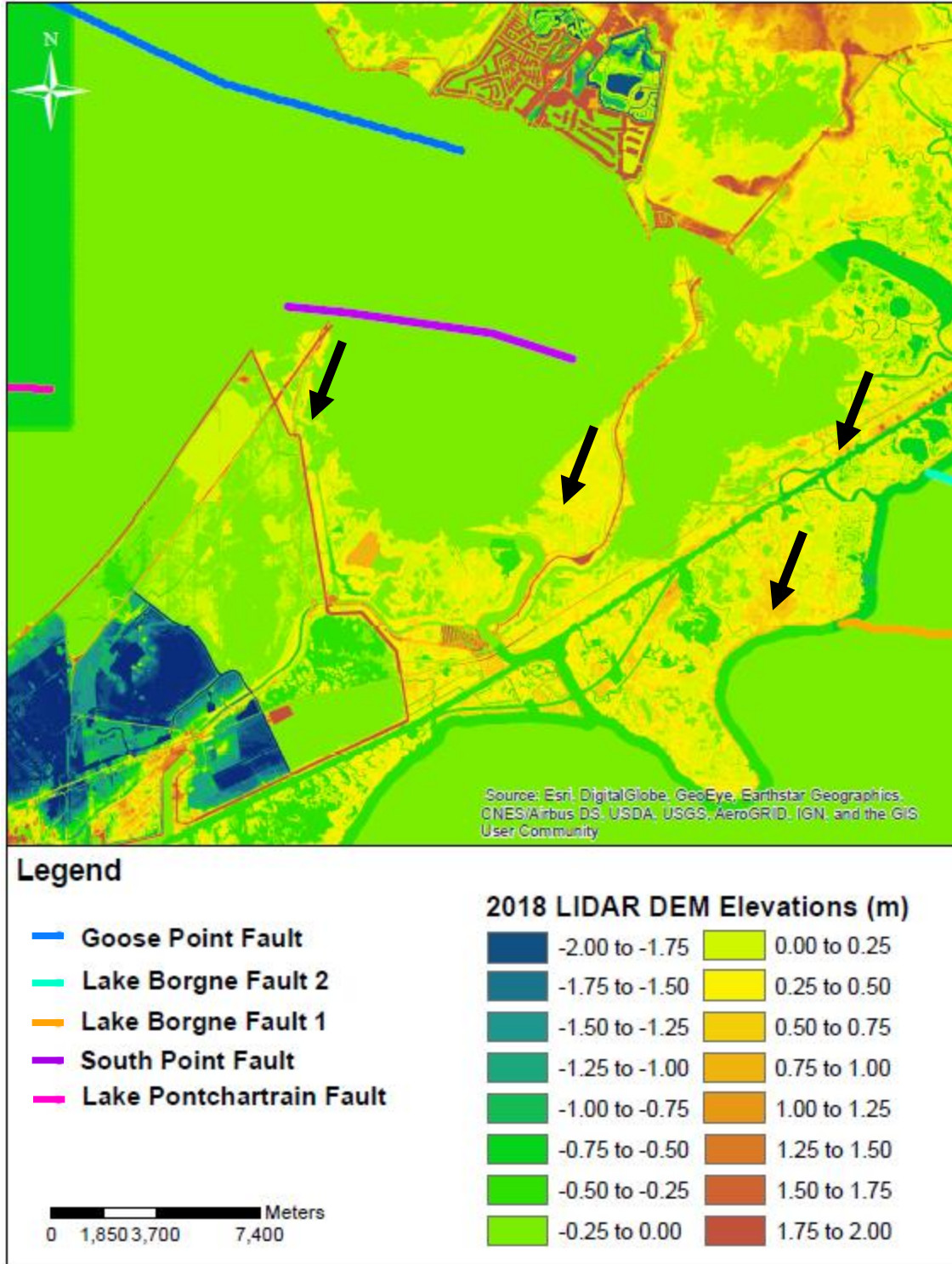


**Figure 61.** Map of the 2018 3-D Elevation Program (3-DEP) collected by USGS in 2017 to provide basic elevation information for the “National Map”. Data were symbolized at 0.25 m (0.82 ft) intervals to identify variations in the elevation of the geomorphology across the Land Bridge. Note the change from higher elevations on north to lower elevations towards the south at each of the black arrows, which is very similar to the 2003 dataset. This change occurs along the projected surface traces of the faults, which suggests that the faults have displaced sediment during the past two decades and the faults seem to continue at least into the land bridge, if not through it completely.

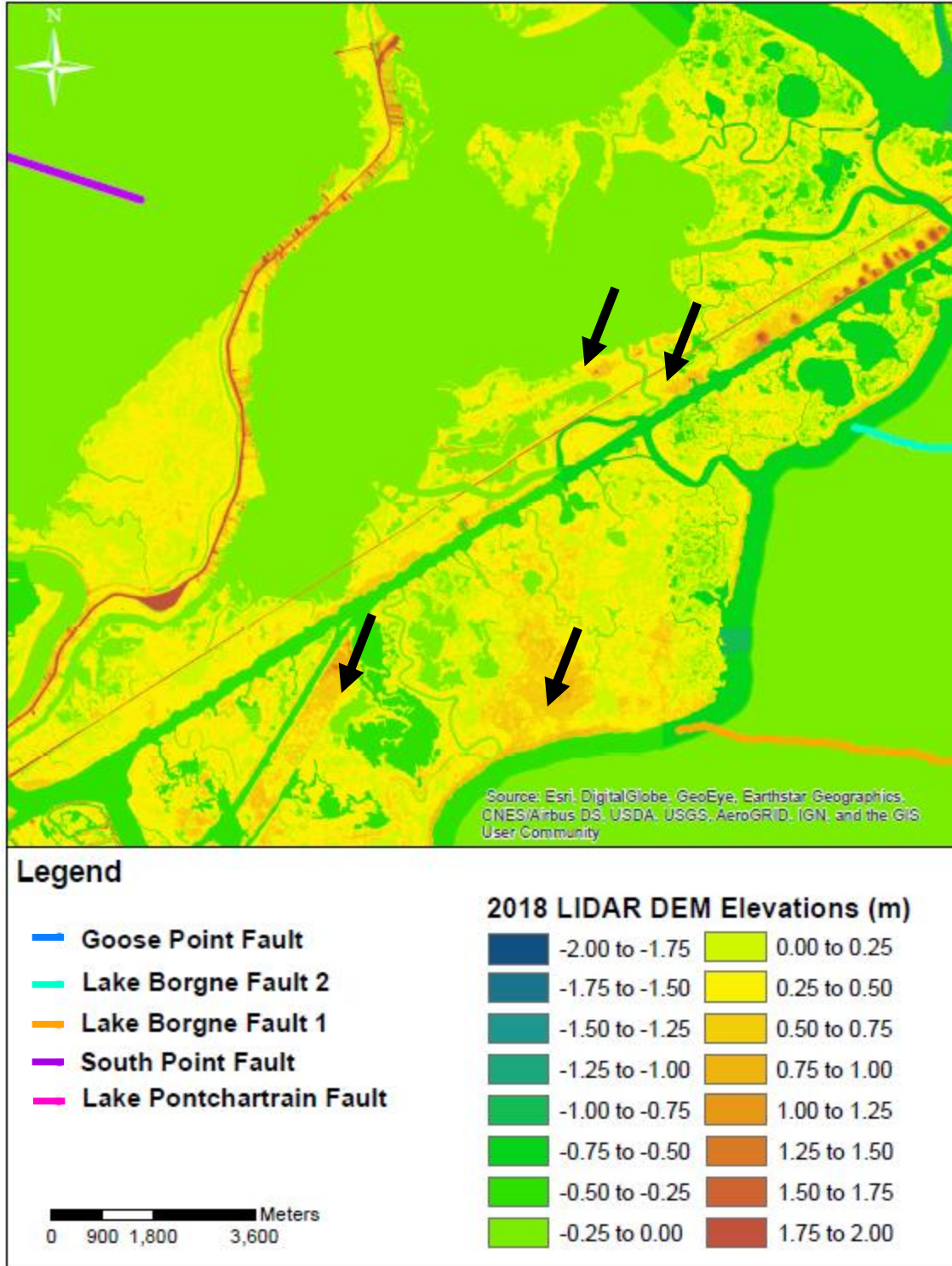


**Figure 62.** Enhanced view of the 2018 3-DEP map using data from USGS (2017). Data were symbolized at 0.25 m (0.82 ft) intervals to identify variations in the elevation of the geomorphology across the Land Bridge. Note the change from higher elevations on north to lower elevations towards the south at each of the black arrows, which is very similar to the 2003 dataset. This change occurs along the projected surface traces of the faults, which may indicate the faults have displaced sediment during the past two decades and the faults seem to continue at least into the land bridge, if not through it completely.

## Chapter 5. Discussion

### 5.1 Fault Activity

Deep seismic data of this study show evidence of fault displacement along the Goose Point Fault and Lake Pontchartrain Fault during the Late Eocene-Early Oligocene time. The data also indicates a decrease in magnitude of fault displacement at approximately the Middle to Late Miocene. It is probable that the faults initiated before the Late Eocene, but seismic resolution decreases significantly below the Late Eocene and therefore cannot be accurately identified. Evidence including the *BasinMod* burial history diagrams in figure 37 correlate well with this interpretation. The graph of expansion index versus time for the Goose Point Fault is consistent with these results as well. Cross-sections from 7 well logs in the study area show clear fault displacement during similar periods of time that are age-constrained by available biostratigraphy. There is also evidence supporting lateral continuity of fault segments beneath the EOLB (Figs. 30-31), but this cannot be confirmed until the entire lateral extent of the fault segments (including beneath the EOLB) are mapped. Chirp seismic data confirm presence of near-surface faults that have been projected upward from locations on conventional seismic.

Noticeable offset of strata above and below the Pleistocene-Holocene contact (correlated to Roth, 1999) is observable on Chirp seismic. This contact was determined to be accurately picked as a top structure map was created (Fig. 52) that shows the Amite River paleochannel as identified by Roth (1999). Late Holocene displacement is not observable due to combined limited vertical resolution of seismic and little or no fault offset at very shallow stratigraphic levels. Fault interpretations below the Pleistocene-Holocene contact are generally unreliable due to decline of Chirp seismic image with depth.

Fault-slip in this study area is likely caused by gravity slumping due to sediment loading by prograding shelf margin delta systems from Late Eocene through Middle Miocene time. After a period of quiescence, faults were reactivated by sediment loading during glacial cycles in the Pleistocene as well as progradation of the St. Bernard Delta (4-1ky). Fault motion may be continuing today due to the effects of recent sediment and eustatic loading. This proposed sequence of events correlates well with the available data (2-D seismic data, well-log cross-sections, BasinMod burial history diagrams, Chirp seismic data, and vibracore cross-sections) indicating that the results for this study are consistent with fault-motion models suggested by McCulloh and Heinrich (2012), Galloway et al. (2000), Lopez (1991), Lopez et al. (1998), Nunn (1985), Ocamb (1961), Rowan et al. (2000), Shen et al. (2016), and Winker (1982).

## ***5.2 Inactive Fault Segments***

Evidence from analysis of shallow, Chirp seismic lines indicates that the Lake Pontchartrain Fault, with noticeable offset in the 2-D deep seismic data, is not actively displacing visible Holocene strata in the shallow Chirp seismic data. As previously stated, this may be due to limited resolution of the Chirp seismic data that crosses the fault. Another possible cause for the appearance of inactivity is due to a lack of compaction of sediments causing a broad slump instead of a distinct scarp (Yuill et al., 2009). Therefore, the fault segment may be active in the Holocene, but evidence of displacement may not exist. Evidence supporting this concept can be seen in a surface expression of stream alignment, whereby the Chef Menteur Pass channel seems to trend along the surface fault trace (Fig. 56). Gagliano et al. (2003) identified similar surface expressions due to at-depth fault motion (Fig. 55). Additionally, the cross-section across the EOLB (Fig. 30) shows offset in strata indicating that the fault may continue through the land bridge along the surface trace predicted from the deep seismic data. Isochron fault displacement

estimates, while relying on the assumptions of constant accretion rates and negligible effects of subsidence, were calculated to have an average rate of 0.22 cm yr<sup>-1</sup>. This rate is similar to the rate of 0.25 cm yr<sup>-1</sup> that Lopez et al. (1997) calculated from offset in the Norfolk-Southern Railroad Bridge. Lake St. Catherine also lacked available deep seismic data for analysis in this study. Therefore, the extent of deep-seated faulting in Lake St. Catherine cannot be accurately inferred from the available data.

### ***5.3 Preservation of Stratigraphy***

Preservation of stratigraphy is critical to assessing lithostratigraphic offset for specific time intervals. Erosional events cause unconformities or breaks in the geologic record, which can make estimates of rates of offset difficult or inaccurate. Therefore, establishing defined chronostratigraphic intervals is necessary to the process of quantifying fault slip rates. The goal of collecting vibracores was to penetrate the Pleistocene-Holocene contact, which would allow for the comparison of up and down sides of strata across projected surface traces and whether offset of the Pleistocene-Holocene contact exists. Isochrons from radiocarbon data indicate fault displacement has occurred across the Lake Pontchartrain Fault except in cross-section A-A' (Fig. 46), possibly a result of stratigraphy preservation in "VC-LP-01", "VC-LP-02", "VC-LP-03", and "VC-LP-04" below the 1500 yr BP isochron. The northern Lake Borgne fault in cross-section F-F' (Fig. 50) may be a result of lack of preservation of stratigraphy as well. Correlation of biostratigraphy and well logs is more reliable in establishing average rates of fault offset because stratigraphy is better preserved at longer timescales in this depositional setting.

Well logs provided by the Department of Natural Resources penetrate depths of more than 25,000 ft (7,620 m). Most well logs, however, do not collect well cuttings for

biostratigraphic analysis at shallow depths (<4,000 ft or 1219 m). In order to interpret the shallow intervals in the seismic data, estimates of depth to shallower biostratigraphic foraminifera were calculated (Table 3). A period of quiescence is visible in the seismic as rates of offset of strata decreases in the shallow strata, but the duration of this period was defined using estimates of shallow biostratigraphic horizons. New well logs may become available with biostratigraphic markers at more shallow intervals (<4000 ft or 1219 m), but these estimates made it possible to address the interpretation of the presence of a period of quiescence. Offset estimates were made with the assumption that there are no breaks in the geologic record, that sediment accumulation remained relatively stable after the deposition of the *Robulus L* pick, and that the biostratigraphic foraminifera would be found in bold reflections corresponding to bounding marine shale sequences as suggested by Galloway et al. (2000).

Offset of near surface strata (Late Pleistocene-Holocene) are visible on 10 Chirp lines crossing the Goose Point Fault. Similar offset is not observed on any of the 4 Chirp seismic lines crossing the Lake Pontchartrain Fault. This suggests the Goose Point Fault is active, whereas the Lake Pontchartrain Fault has not been active during the Holocene. However, Chirp data across the Lake Pontchartrain fault are lower in resolution than those across the Goose Point Fault, so lack of Late Pleistocene-Holocene movement on the Lake Pontchartrain Fault in this study area is not definitive. Yuill et al. (2009) suggested that shallow Holocene sediments in Louisiana commonly undergo slumping instead of sudden fault slips, due to the presence of soft, less viscous sediments. In the deep 2-D seismic data, resolution increases below 2.5 s twt, and fault-slip below 2.5 s twt can only be suggested. However, evidence suggests that the Lake Pontchartrain Fault and Goose Point Fault were active during the Late Eocene-Early Oligocene.

Seismic with higher resolution and biostratigraphy below 2.5 s twt could provide an alternative explanation.

#### ***5.4 Implications of BasinMod Burial History***

*BasinMod* has not been previously used to interpret fault slip rates or to study the effects of decompaction on those fault slip rates. The burial history models were created to compare the up- and down-thrown side of the Goose Point Fault and show fault initiation that is consistent with the suggestion by McCulloh and Heinrich (2012). The *BasinMod* burial history models were also used to estimate the effect of decompaction in the comparison of modern fault slip rates against fault slip rates at the proposed initiation of fault slip in the study area (Late Eocene-Early Oligocene). The plot rate of offset versus time (Fig. 36), shows an abrupt increase associated with a reactivation of the fault slip between the Late Pliocene-Late Pleistocene period and continuing into the Holocene. *BasinMod* shows the abrupt increase in subsidence, but the exact time is debatable due to the lack of available shallow biostratigraphic foraminifera data. During the period of reactivation, there is a sharp increase in rate of offset for time increments, and rates have values similar with or greater than those calculated in Middle Miocene and older times, perhaps a result of decompaction. Strata at 10,000 ft depth (~3,048 m) are subject to higher overburden pressures, which cause the strata to appear thinner than their thickness at original deposition. *BasinMod* has an option to use various decompaction methods to estimate the original thickness of strata. In this case the Baldwin-Butler (1985) method was used. Rates of offset in the decompacted Miocene and older sediments increase as much as “50%” compared to rates calculated from current thicknesses. Thus, slip rates during the period of fault reactivation are likely similar or lower than those during fault initiation and primary activity.

## ***5.5 Impacts to Local Geomorphology***

Vertical offset measured on the Highway 11 Bridge along the Goose Point Fault surface trace and open water on the down-thrown side of faults (such as the Goose Point Fault) indicate that these faults are Holocene strata, but in some cases (such as the Lake Pontchartrain Fault) there is lack of offset evident in Chirp seismic. Well log cross-sections indicate there is noticeable offset in the deep strata across the faults and the faults seem to show lateral continuity beneath the land bridge, even though the extent of these faults cannot be mapped without available deep seismic data in the eastern-most part of Lake Pontchartrain and Lake St. Catherine in whole. This result led to the development of the fault traces (Fig. 56), which are subject to interpretation with the lack of available data.

## Chapter 6. Conclusions

Wetland loss as a result of relative sea level rise and subsidence is evident across southern Louisiana (Couvillion et al., 2017; Dokka, 2006; Flocks et al., 2009a; Gagliano et al., 2003; Haggard, 2014; Kulp, 2000; Yuill et al., 2009). Industry seismic surveys, deep well logs, vibracores, and Chirp seismic were used to attempt to locate the lateral extent of faults proximal to the EOLB, east Lake Pontchartrain, Lake St. Catherine, and Lake Borgne. Deep seismic was used to confirm offset of biostratigraphic markers in well log cross-sections and was used to correlate periods of fault activity/inactivity during the Cenozoic as predicted in the *BasinMod* software. Fault displacement rates were also calculated from the available deep seismic surveys, well logs with biostratigraphy data, isochron estimates, and high-resolution Chirp seismic. Well logs with biostratigraphic markers were used to confirm the presence of deep-seated faults as well as calculate offset due to a combination of faulting and subsidence across the study area. Cross-sections of well logs with biostratigraphic markers also indicate fault offset beneath the EOLB indicating lateral continuity. However, connectivity of certain fault segments cannot be determined without deep industry seismic data between the Lake Borgne and Lake Pontchartrain fault segments.

Burial History diagrams made using biostratigraphic correlations of well logs indicate a similar period of activity (40-16 Ma), inactivity with continued subsidence (16-1.8 Ma), and reactivation (approximately 1.8 Ma-Recent) along segments of the larger Baton Rouge Fault System. This may be a result of continued progradation of the Cenozoic shelf margins as sediment loading in the study area decreased in the Middle-Late Miocene and reactivated as a result of basin loading, glacial cycles and subsidence from 1.8 Ma to present day. Chirp seismic, vibracore cross-sections, aerial imagery, and Lidar data support the interpretation that the BRFS,

LBFS, and Lake Pontchartrain Fault are in lateral communication beneath the EOLB. Shallow Chirp seismic collected across  $\pm 5^\circ$  dip of surface fault trace projections predicted using available deep seismic data. Vibrocore cross sections identify possible offset of shallow strata and isochrones across the project fault trends. The BRFS and LBFS are currently affecting Holocene geomorphology. At present there is inadequate data to support the idea that the Lake Pontchartrain Fault has been active in Recent time. Understanding the potential effect of fault motion is critical to formulating mitigation plans for the widespread wetland loss of coastal Louisiana well as protecting infrastructure such as levees and major roadways.

## References

- Autin, W.J.; Burns, S.F.; Miller, B.J.; Saucier, R.T., and Snead, J.I., 1991, Quaternary geology of the Lower Mississippi Valley. In: Morrison, R.B. (ed.), Quaternary Nonglacial Geology Conterminous United States, The Geology of North America, K-2, Boulder, Colorado, Geological Society of America, p. 547-582.
- Autin, W., 1996. Pleistocene stratigraphy in the southern Lower Mississippi valley. *Engineering Geology*, no. 45, p. 87-112.
- Avseth, A., Mukerji, T., Mavko, G., 2010, *Quantitative Seismic Interpretation*, Cambridge, p. 168-211.
- Baldwin, B., and Butler, C.O., 1985, *Compaction Curves*, The American Association of Petroleum Geologists Bulletin, v. 69, no. 4, p. 622-626.
- Bentley, S. J. Sr., Blum, M.D., Maloney, J., Pond, L., Paulsell, R., 2015, The Mississippi River source-to-sink system: Perspectives on tectonic, climatic, and anthropogenic influences, Miocene to Anthropocene, *Earth-Science Reviews*, 36 p.
- Blum, M., and Pecha, M., 2014, Mid-Cretaceous to Paleocene North American drainage reorganization from detrital zircons, *Geology*, v. 42, no. 7, p. 607-610.
- Couvillion, B.R., Beck, H., Schoolmaster, D., and Fischer, M., 2017, Land area change in coastal Louisiana 1932 to 2016: U.S. Geological Survey Scientific Investigations Map 3381, pamphlet, 16 p.
- Cunningham, R., Gisclair, D., & Craig, J., 2004, The Louisiana Statewide Lidar Project, [Online], Available From: [https://www.researchgate.net/publication/237366946\\_The\\_Louisiana\\_Statewide\\_LIDAR\\_Project](https://www.researchgate.net/publication/237366946_The_Louisiana_Statewide_LIDAR_Project)
- Department of Natural Resources, 2017, Strategic Plan Fiscal Year 2017-2018 through Fiscal Year 2021-2022, 27 p.
- Dokka, R. K., 2006, Modern-day tectonic subsidence in coastal Louisiana. *Geology* 34, p. 281-284.
- Dunbar, J.B., Blaes, M.R., Dueitt, S.E., May, J.R., 1994, *Geologic Investigation of the Mississippi River Delta Plain: U.S. Engineers Waterways Experiment Station, Technical Report GL-84-15, Report 2*, 36 p.
- Durham, C.O. Jr., and Peebles, E.M. III, 1956, Pleistocene Fault Zone in Southeastern Louisiana, *Gulf Coast Association of Geological Societies Transactions*, v. 6, p. 65-66.
- EdgeTech, 2015, 3100-P Portable Sub-Bottom User Hardware Manual, 79 p.
- Feng, J., 1995, Post mid-Cretaceous seismic stratigraphy and depositional history, deep Gulf of Mexico, Austin, Texas: University of Texas at Austin, Ph.D. Dissertation, 253 p.

- Fisk, H.N., 1944, Fine-Grained Alluvial Deposits and Their Effects on Mississippi River Activity, Vicksburg, Mississippi: Mississippi River Commission, U.S. Army Corps of Engineers, v. 2, 82 p.
- Fisk, H. and McFarlan, E., 1955. Late Quaternary Deltaic Deposits of the Mississippi River, Geological Society of America, Special Paper 62, p. 279-302.
- Flocks, J., Kulp, M., Smith, J., & Williams, S. J., 2009a, Review of the geologic history of the Pontchartrain Basin, Northern Gulf of Mexico, *Journal of Coastal Research*, p. 12-22.
- Flocks, J., Kindinger, J., Marot, M., and Holmes, C., 2009b, Sediment characterization and dynamics in Lake Pontchartrain, Louisiana, *Journal of Coastal Research*, p. 113-126.
- Frank, J., 2017, Integrating 3-D seismic with shallow high resolution seismic: evidence of fault movement during the Holocene in Southern Louisiana, New Orleans, Louisiana: University of New Orleans, Master's Thesis, 91 p.
- Gagliano, S.; Kemp, E.; Wicker, K., and Wiltenmuth, K., 2003, Active Geological Faults and Land Change in Southeastern Louisiana, *Gulf Coast Association of Geological Societies Transactions*, no. 53, 178 p.
- Gagliano, S., 2005, Testimony: Effects of Geological Faults on Levee Failures in South Louisiana. Prepared for Presentation and Discussion U.S. Senate Committee on Environment and Public Works, Presented by Coastal Environments, Inc., November 17, 2005, 26 p.
- Galloway, W. E., D. G. Bebout, W. L. Fisher, R. Cabrera-Castro, J. E. Lugo-Rivera, and T. M. Scott, 1991, Cenozoic, in A. Salvador, ed., *The geology of North America: the Gulf of Mexico basin*, v. J, Boulder, Colorado, Geological Society of America, p. 245–324.
- Galloway, W.E., Ganey-Curry, P.E., Li, X., and Buffler, R., 2000, Cenozoic depositional history of the Gulf of Mexico basin, *AAPG Bulletin*, v. 84, no. 11, p. 1743-1774.
- Galloway, W.E., Whiteaker, T.L., and Ganey-Curry, P.E., 2010, History of Cenozoic North American drainage basin evolution, sediment yield, and accumulation in the Gulf of Mexico basin, *Geosphere*, v. 7, no. 4, p. 938-973.
- Haggard, K.S., 2014, Coastal land loss and landscape level plant community succession: An expected result of natural tectonic subsidence, fault movement, and sea level rise: *Gulf Coast Association of Geological Societies Transactions*, v. 64, p. 139–159.
- Hanor, J.S., 1982, Reactivation of Fault Movement, Tepehate Fault Zone, South Central Louisiana, *Gulf Coast Association of Geological Societies Transactions*, v. 32, p. 237-245.

- Kindinger, J.L., Williams, S.J., Penland, S., Flocks, J.G., and Connor, P.C., 1997, Holocene geologic framework of Lake Pontchartrain Basin and lakes of southeastern Louisiana, Gulf Coast Association of Geological Societies Transactions, no. 47, p. 635–638.
- Kolb, C. R., F. L. Smith, and R. C. Silva., 1975, Pleistocene sediments of the New Orleans-Lake Pontchartrain area, US Army Corps Technical Report, No. S-75-6, 56 p.
- Kulp, M.A., 2000, Holocene Stratigraphy, History, and Subsidence of the Mississippi River Delta Region, North-Central Gulf of Mexico, Lexington, Kentucky: University of Kentucky, Ph.D. dissertation, 347 p.
- Kulp, M.A., Howell P., Adiau S., Penland S., Kindinger J., Williams S.J, 2002, Latest Quaternary stratigraphic framework of the Mississippi delta region, Transactions of The Gulf Coast Association of Geological Societies, 52, p. 572–82.
- Levesh, J., 2019, Middle Miocene to Holocene History of the Delacroix Island Fault System, New Orleans, Louisiana: University of New Orleans, Master's Thesis, 89 p.
- Lopez, J.A., 1991, Origin of Lake Pontchartrain and the 1987 Irish Bayou earthquake, In: Coastal Depositional Systems in the Gulf of Mexico: Quaternary Framework and Environmental Issues. Gulf Coast Section Society for Sedimentary Geology (GCSSEPM) Twelfth Annual Research Conference, v. 9, p. 103–110.
- Lopez, J.A., Penland, S., and Williams, J., 1998, Confirmation of active geologic faults in Lake Pontchartrain in southeast Louisiana, Gulf Coast Association of Geological Societies Transactions, no. 47, p. 299–303.
- Lopez, J. and Connor, P. Jr., 2001, Fault map depicting the Baton Rouge-Denham Springs Fault system in Lake Pontchartrain (Original Plate).
- McCulloh, R.P., 2001, Active Faults in East Baton Rouge Parish, Louisiana. Louisiana Geological Survey.
- McCulloh, R.P., and Heinrich, P.V., 2012, Surface faults of the south Louisiana growth-fault province, Geological Society of America Special Papers, no. 493, p. 37-49.
- Nunn, J.A., 1985, State of stress in the northern Gulf Coast, Geology, v. 13, no. 6, p. 429-432.
- Ocamb, R.D., 1961, Growth Faults of South Louisiana, Gulf Coast Association of Geological Societies Transactions, v. 11, p. 139-175.
- Otvos, E.G., Jr., 1978, New Orleans-South Hancock Holocene barrier trends and origins of Lake Pontchartrain. Gulf Coast Association of Geological Societies Transactions, no. 28, p. 337–355.
- Otvos, E.G. and Howatt, W.E., 1992, Late Quaternary coastal units and marine cycles: correlations between northern Gulf sectors, Gulf Coast Association of Geological Societies Transactions, v. 42, p. 571-585.

- Paleo Data, 2018, Unpublished Biostratigraphic Formation Tops and Paleobathymetry Maps, Paleo Data Inc., Metairie, Louisiana.
- Peel, F.J., Travis, C.J., & Hossack, J.R., 1995, Genetic Structural Provinces and Salt Tectonics of the Cenozoic Offshore U.S. Gulf of Mexico: A preliminary analysis, *Salt Tectonics: A Global Perspective*, V. 65, p. 153-175.
- Roland, H. L., Hill, T. F., Autin, P., Durham Jr, C. O., & Smith, C. G., 1981, The Baton Rouge and Denham Springs-Scotlandville faults, Louisiana Geological Survey, Department of Natural Resources.
- Roth, M.L., 1999, Late Pleistocene to Recent Subsurface Geology of Lake Pontchartrain, Louisiana: Integration of Geophysical and Geological Techniques, New Orleans, Louisiana: University of New Orleans, Master's Thesis, 187 p.
- Rowan, M. G., Trudgill, B. D., and Fiduk, J. C., 2000, Deep-water, salt-cored foldbelts: lessons from the Mississippi Fan and Perdido foldbelts, northern Gulf of Mexico, *Geophysical Monograph by the American Geophysical Union*, no.115, p. 173-192.
- Salvador, A., 1987, Late Triassic-Jurassic paleogeography and origin of Gulf of Mexico Basin, *American Association of Petroleum Geologists Bulletin*, no. 71, p. 419–451.
- Sasser, C.E., Visser, J.M., Mouton, E., Linscombe, J., and Hartley, S.B, 2008, Vegetation types in coastal Louisiana in 2007, U.S. Geological Survey Open-File Report 2008–1224, 1 sheet, scale 1:550,000.
- Saucier, R.T., 1963, Recent Geomorphic History of the Pontchartrain Basin. Louisiana State University Studies, Coastal Studies Series, v. 9, 114 p.
- Saucier, R.T., 1994, Geomorphology and Quaternary Geologic History of the Lower Mississippi Valley. Vicksburg, Mississippi: U.S. Army Corps of Engineers, Waterways Experiment Station, v. 1, 361 p.
- Seed, R., Abdelmalak, R., Athanasopoulos, A., Bea, R., Boutwell, G., Bray, J., Briaud, J., Cheung, C, Cobos-Roa, D., Cohen-Waeber, J., Collins, B., Ehrensing, L., Farber, D., Hanenmann, M., Harder, L., Inamine, M., Inkabi, K, Kammerer, A., Karadeniz, D., Kayen, R., Moss, R., Nicks, J., Nimala, S., Pestana, J., Porter, J., Rhee, K., Riemer, M., Roberts, K., Rogers, J., Storesund, R., Thompson, A., Govindasamy, A., Vera-Grunauer, X., Wartman, J., Watkins, C., Wenk, E., and Yim, S., 2006, Investigation of the Performance of the New Orleans Flood Protection Systems in Hurricane Katrina on August 29, 2005, Independent Levee Investigation Team Report, chapter 3, part III, v. 1, 19 p.
- Shen, Z., Dawers, N.H., Törnqvist, T.E., Gasparini, N.M., Hijma, M.P., & Mauz, B., 2016, Mechanisms of late Quaternary fault throw-rate variability along the north central Gulf of Mexico coast: implications for coastal subsidence, *Basin Research*, v. 29, p. 557-570.

- Trahan, L.J., 1989, Soil survey of Orleans Parish, Louisiana, Washington, D.C., Soil Conservation Service, 89 p.
- United States Geological Survey, 2018, USGS NED 1/3 arc-second n31w090 1 x 1 degree ArcGrid 2018: U.S. Geological Survey.
- Winker, C.D., 1982, Cenozoic Shelf Margins, Northwestern Gulf of Mexico, Gulf Coast Association of Geological Societies Transactions, v.32, p. 427-448.
- Worrall, D. M., and Snelson, S., 1989, The geology of North America—An overview, Geological Society of America, The Geology of North America, p. 97-138.
- Wu, X., 2004, Upper Miocene Depositional History of the Central Gulf of Mexico Basin, Austin, Texas: University of Texas at Austin, Ph.D. Dissertation, 337 p.
- Yeager, K.M., Brunner, C.A., Kulp, M.A., Fischer, D., Feagin, R.A., Schindler, K.J., Prouhet, J., & Bera, G., 2012, Significance of active growth faulting on marsh accretion processes in the Lower Pearl River, Louisiana, *Geomorphology*, no. 153-154, p. 127-143.
- Yuill, B., Lavoie, D., and Reed, D.J., 2009, Understanding subsidence processes in coastal Louisiana, *Journal of Coastal Research*, Special Issue 54, p. 23-36.

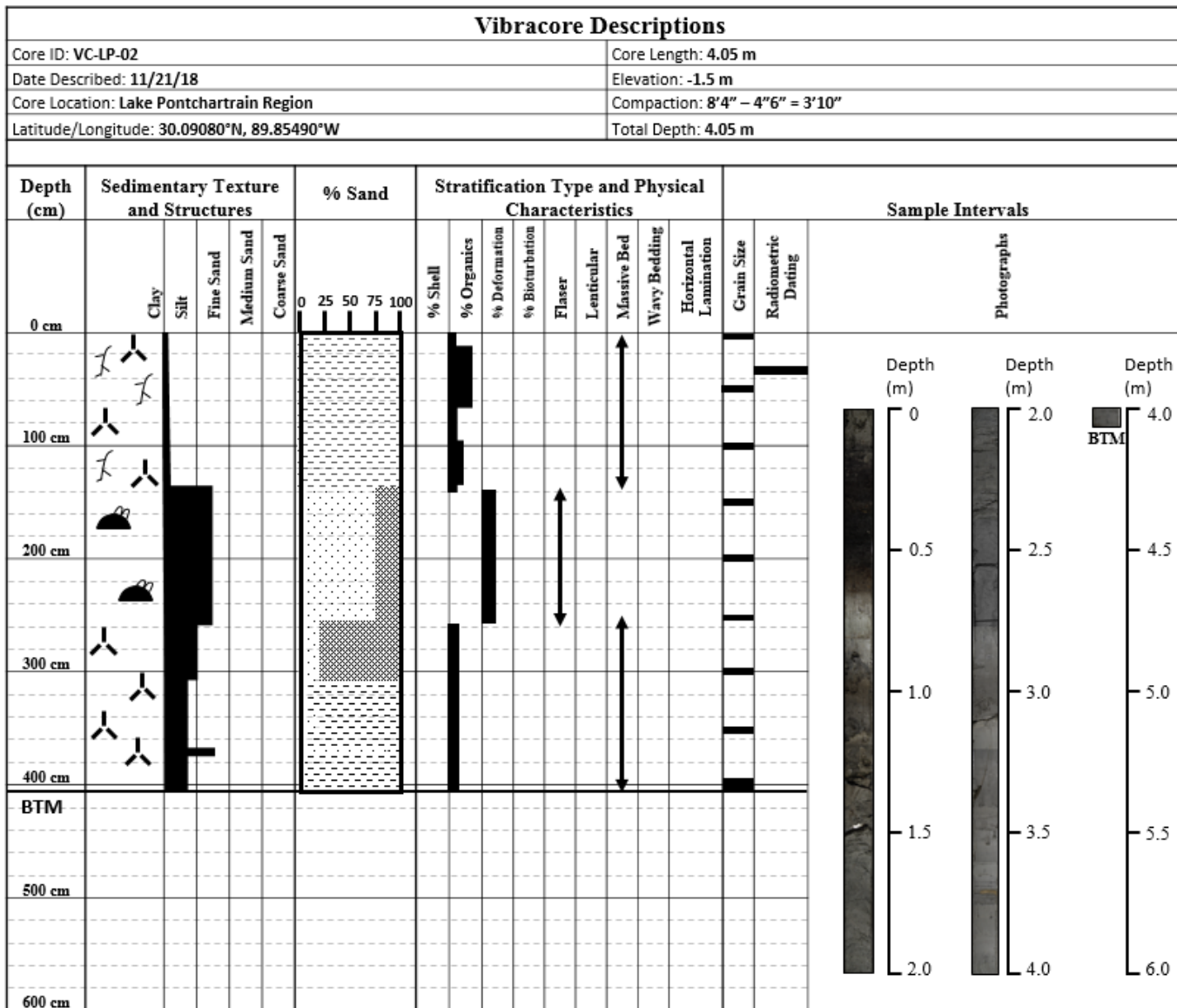
## Appendix A: Vibracore Descriptions

Legend	
	- Sand
	- Sandy Clay/ Clay-Sand
	- Silty Clay
	- Silty Sand
	- Clay
	- Bioturbation
	- Burrows (sand-filled)
	- Organic Rooting
	- Horizontal Laminations
	- Organics (Trace)
	- Shell Fragments
	- In-Tact Shells
	- Wavy Bedding
	- Lenticular Beds
	- Flaser Beds

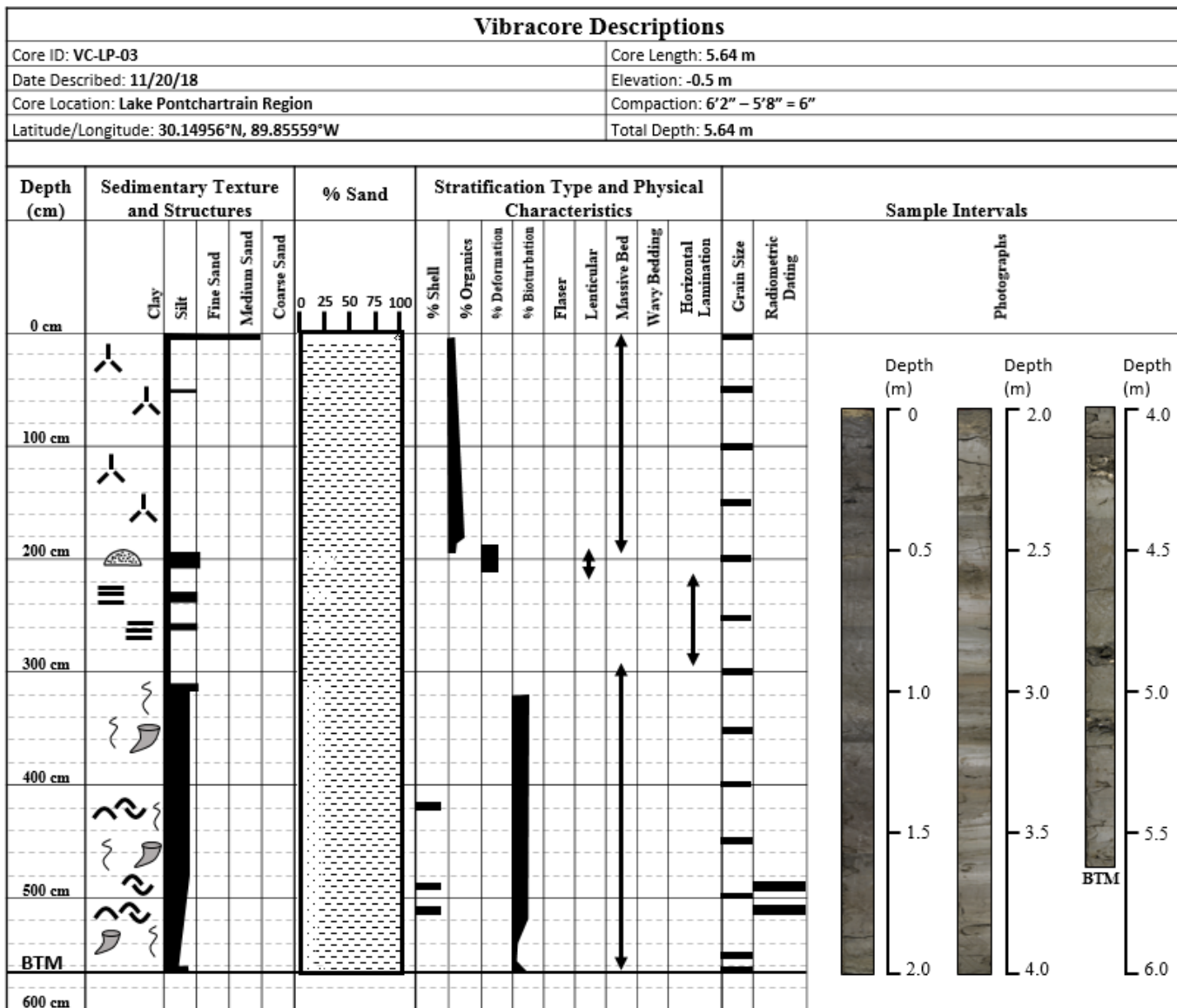
Appendix A Figure 1. Vibracore legend used to describe shallow stratigraphy in collected vibracores.

Vibracore Descriptions																					
Core ID: VC-LP-01							Core Length: 0.83 m														
Date Described: 9/01/18							Elevation: -2.8 m														
Core Location: Lake Pontchartrain Region							Compaction: 9'1" – 8'1" = 1.0'														
Latitude/Longitude: 30.08098°N, 89.85302°W							Total Depth: 0.83 m														
Depth (cm)	Sedimentary Texture and Structures					% Sand	Stratification Type and Physical Characteristics							Sample Intervals							
														Photographs							
0 cm	Clay	Silt	Fine Sand	Medium Sand	Coarse Sand	0 25 50 75 100	% Shell	% Organics	% Deformation	% Bioturbation	Flaser	Lenticular	Massive Bed	Wavy Bedding	Horizontal Lamination	Grain Size	Radiometric Dating	Depth (m)	Depth (m)	Depth (m)	
BTM																			0	2.0	4.0
100 cm																		0.5	2.5	4.5	
200 cm																		1.0	3.0	5.0	
300 cm																		1.5	3.5	5.5	
400 cm																		2.0	4.0	6.0	
500 cm																					
600 cm																					

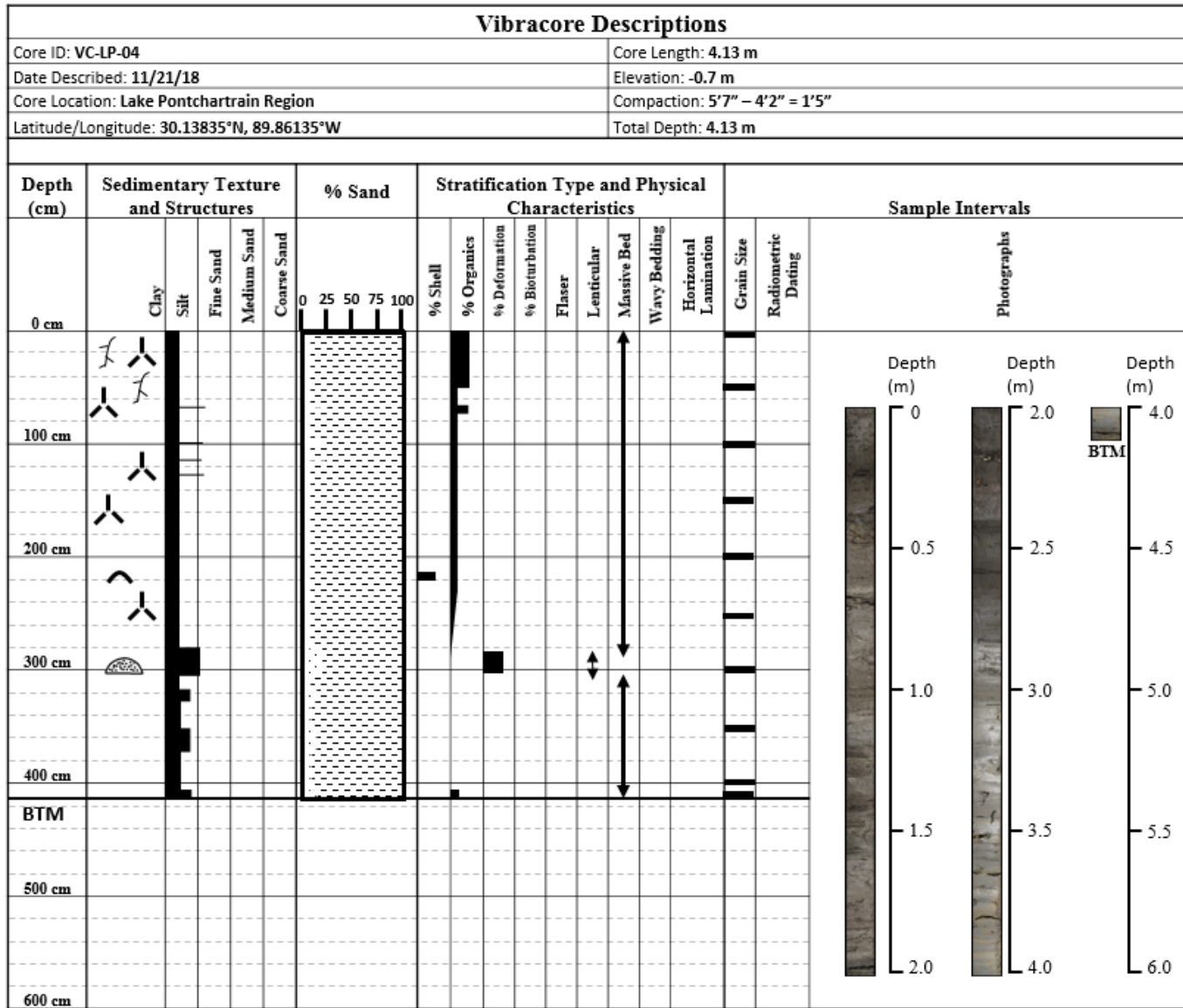
Appendix A Figure 2. Description of core VC-LP-01.



Appendix A Figure 3. Description of core VC-LP-02.

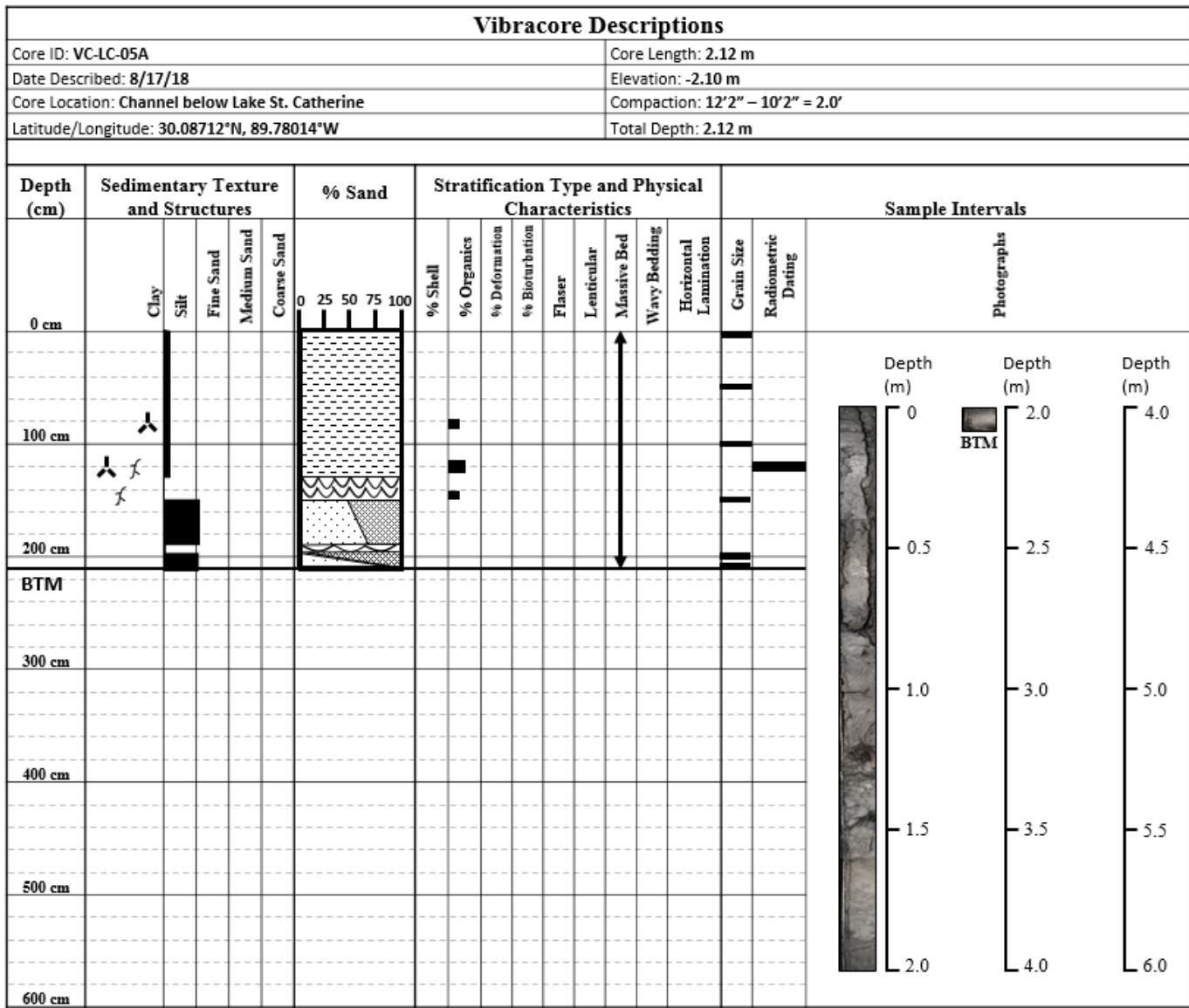


Appendix A Figure 4. Description of core VC-LP-03.

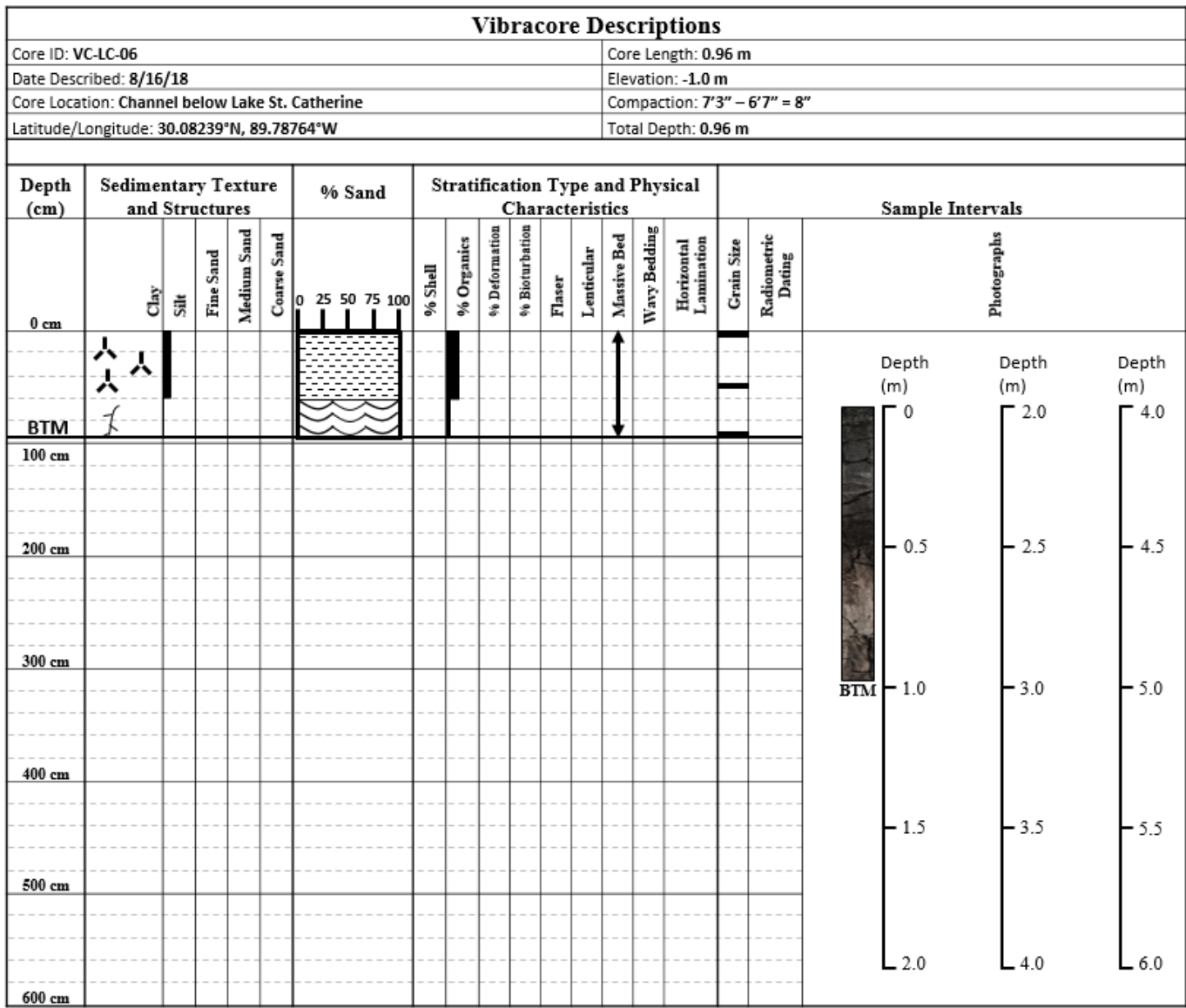


Appendix A Figure 5. Description of core VC-LP-04.

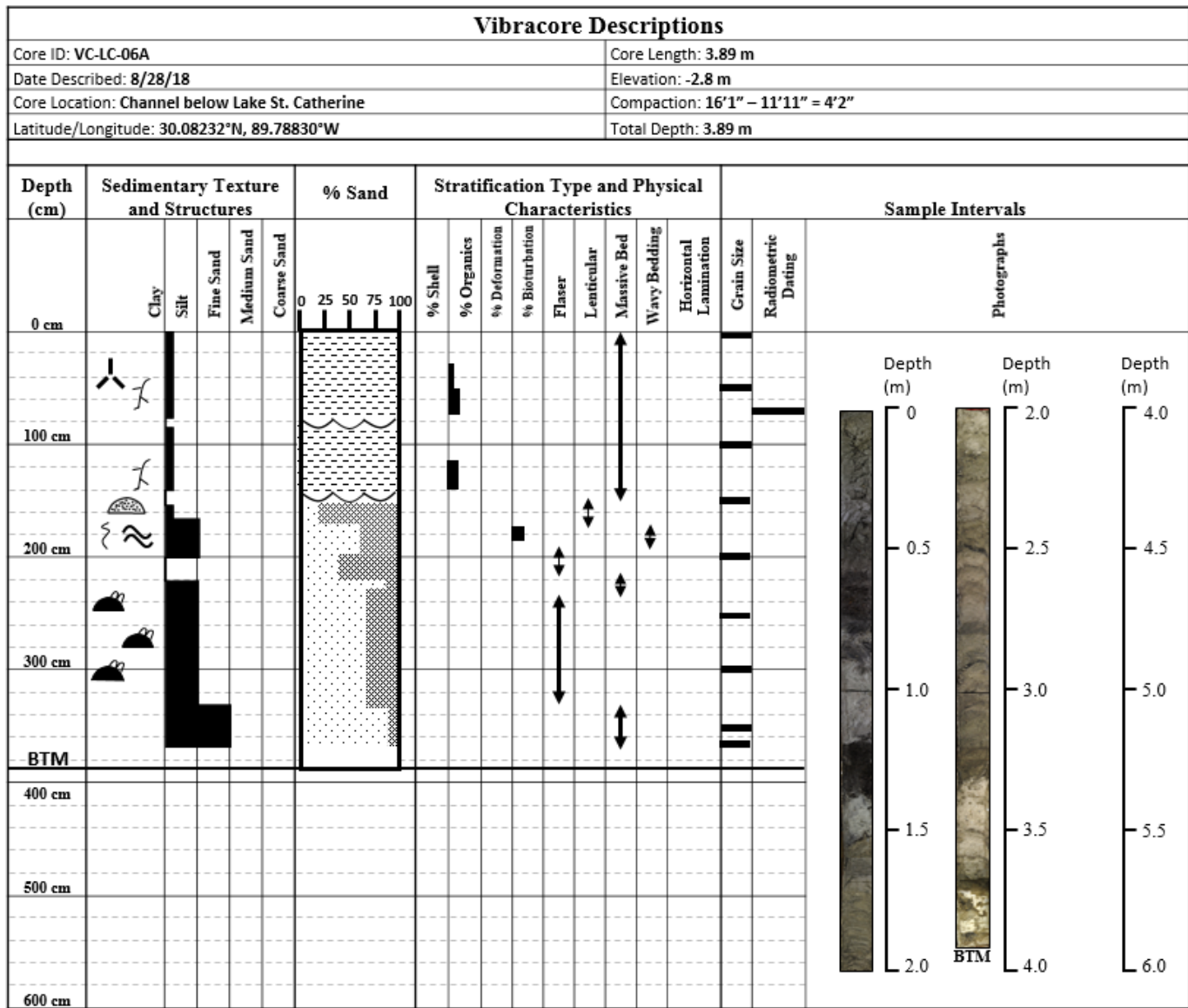




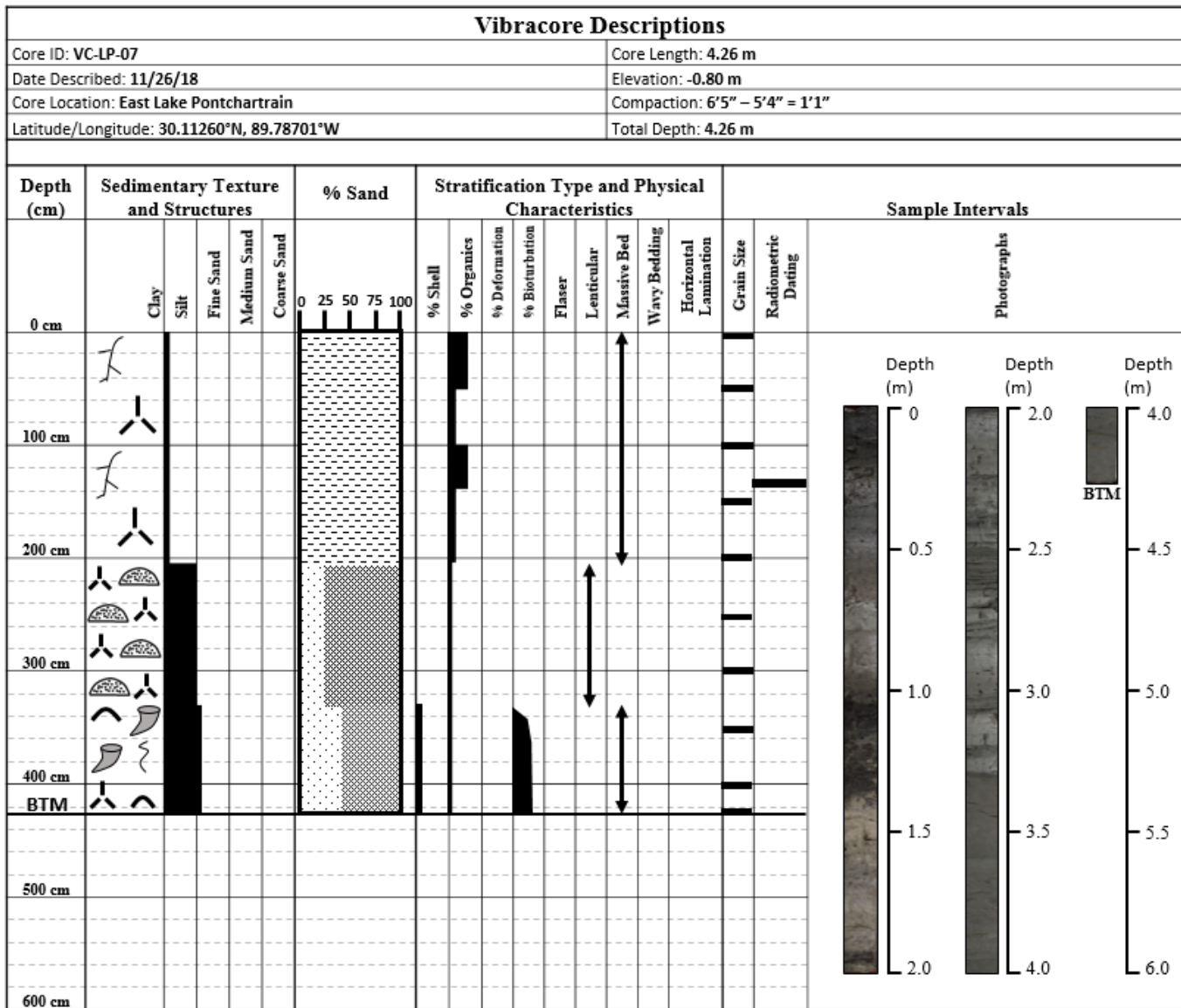
Appendix A Figure 7. Description of core VC-LC-05A.



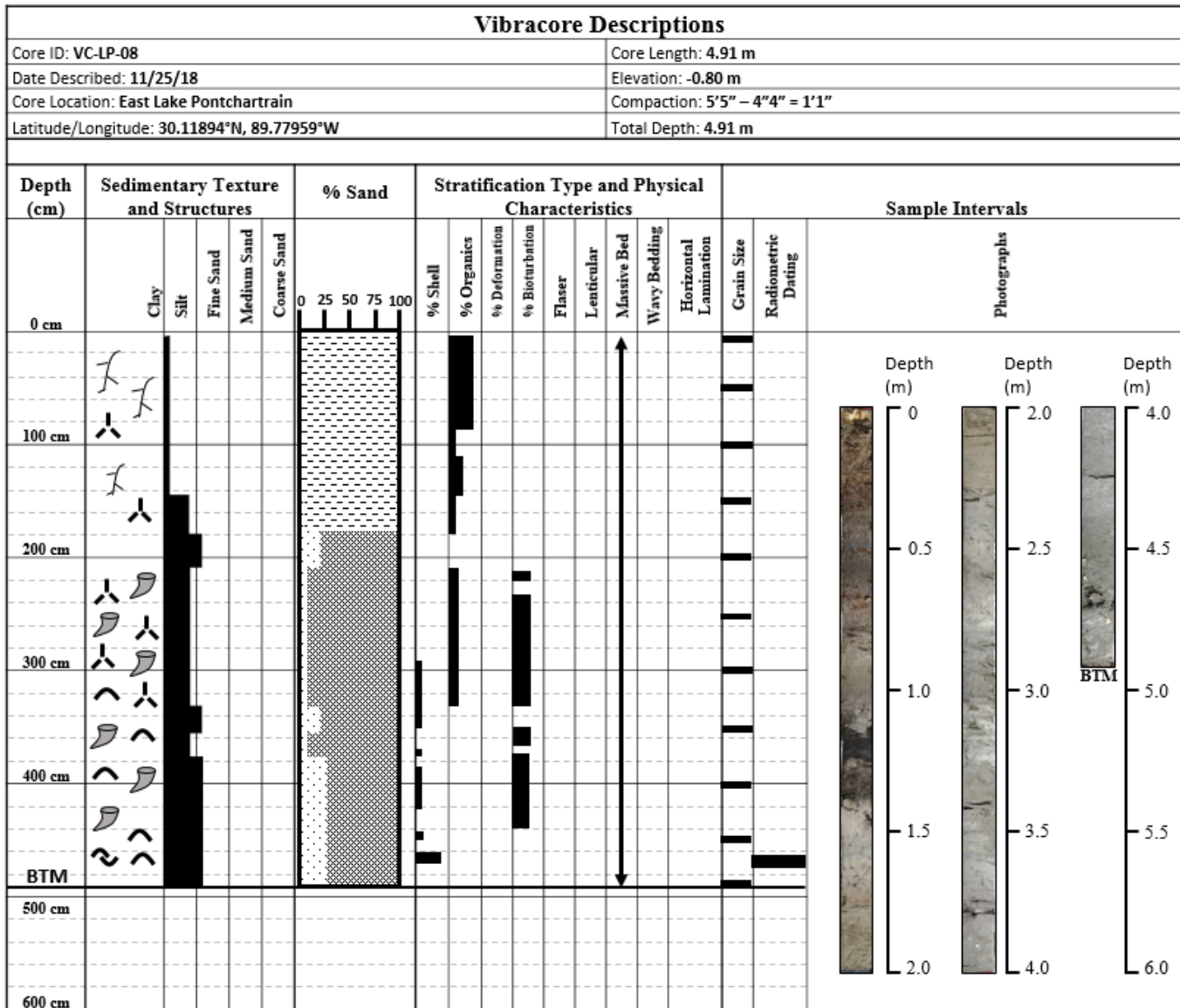
Appendix A Figure 8. Description of core VC-LC-06.



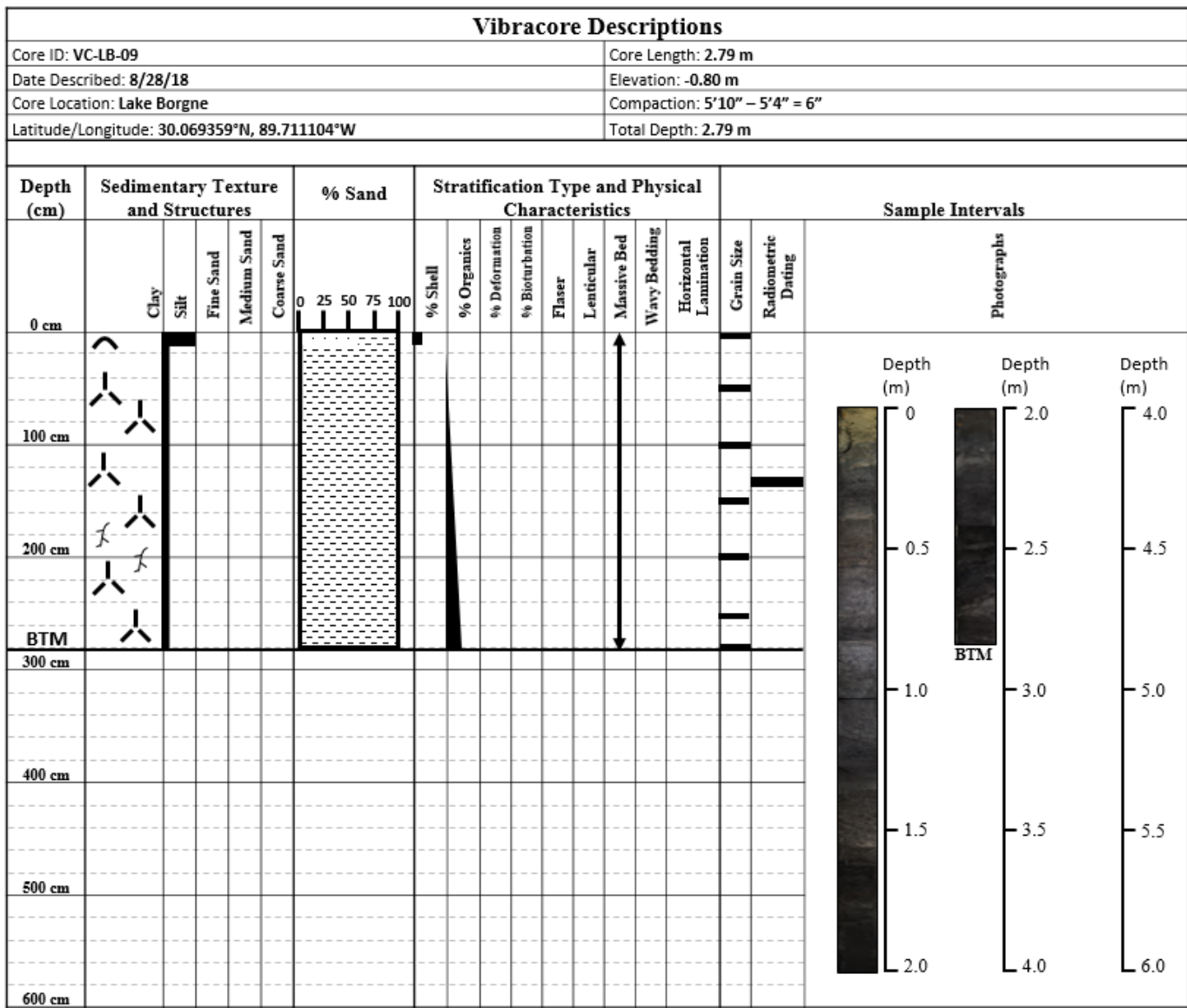
Appendix A Figure 9. Description of core VC-LC-06A.



Appendix A Figure 10. Description of core VC-LP-07.

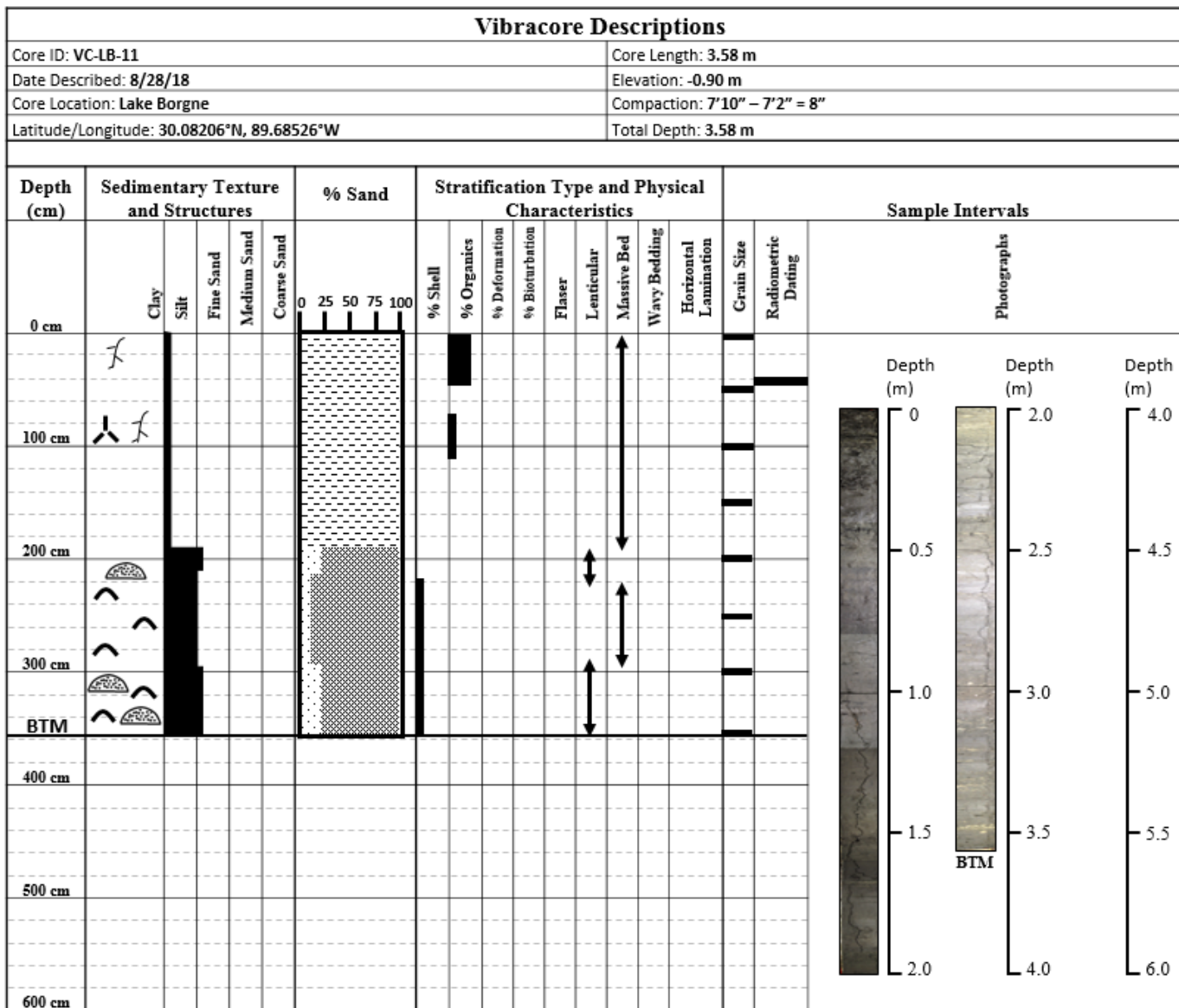


Appendix A Figure 11. Description of core VC-LP-08.

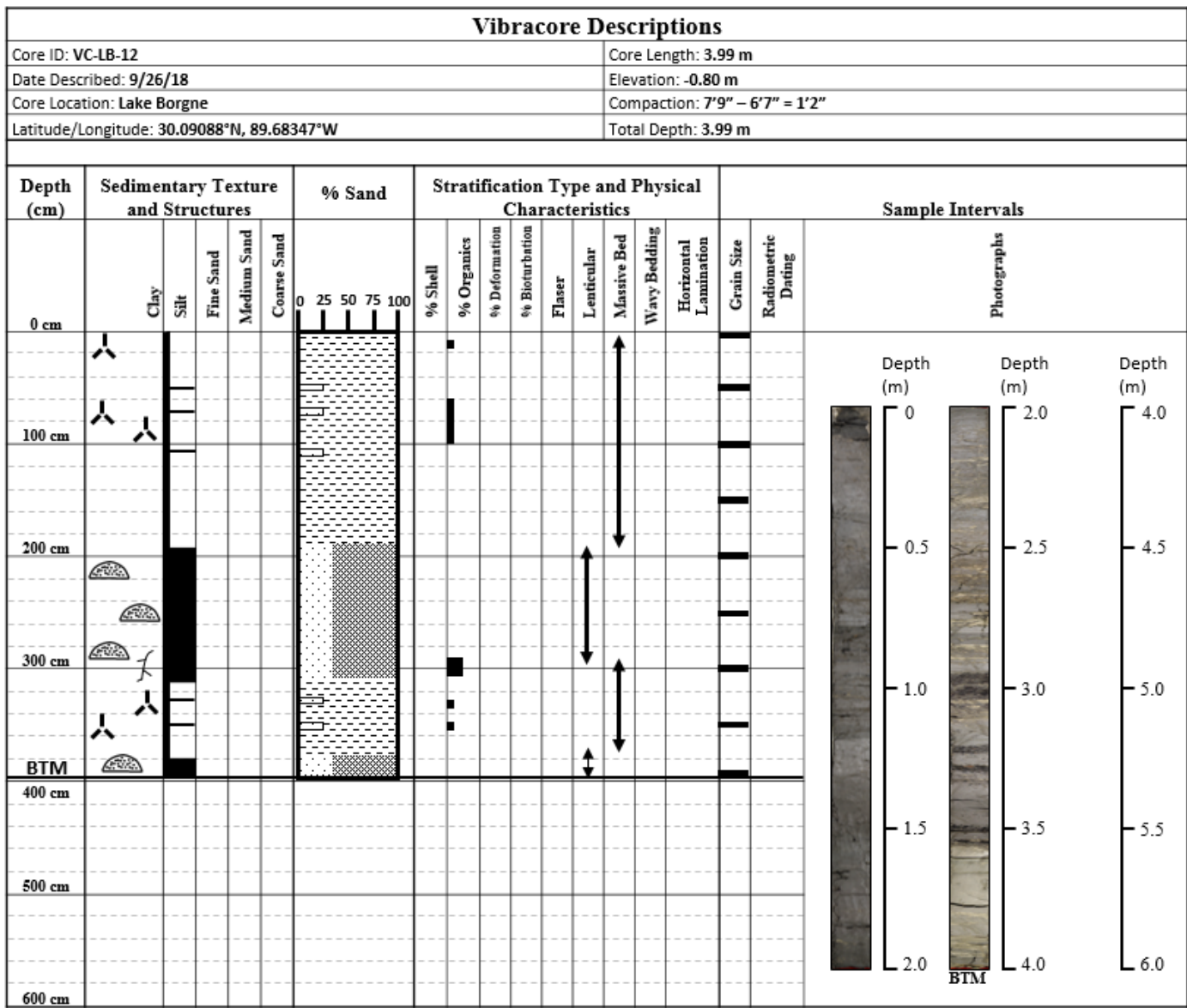


Appendix A Figure 12. Description of core VC-LB-09.

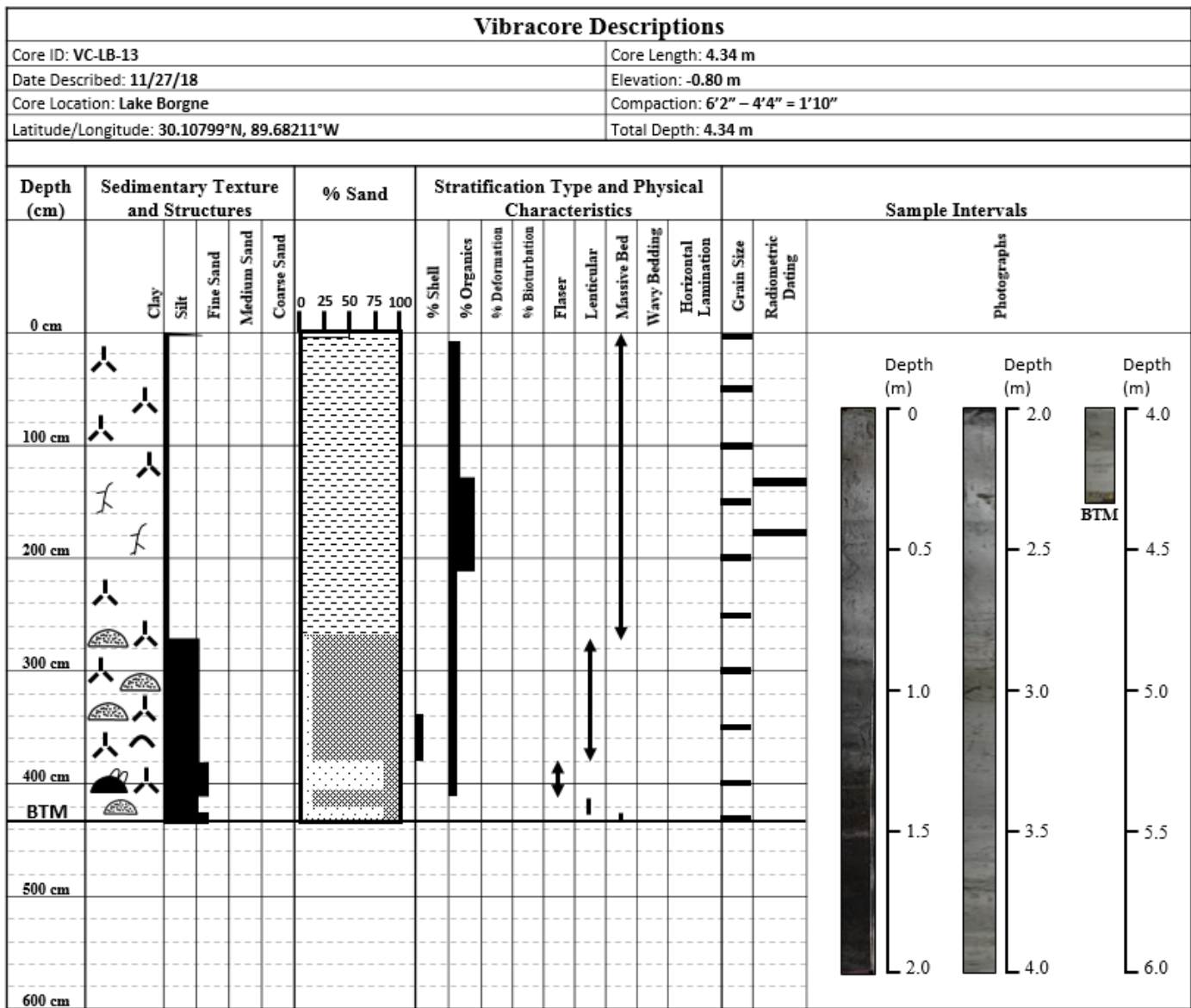




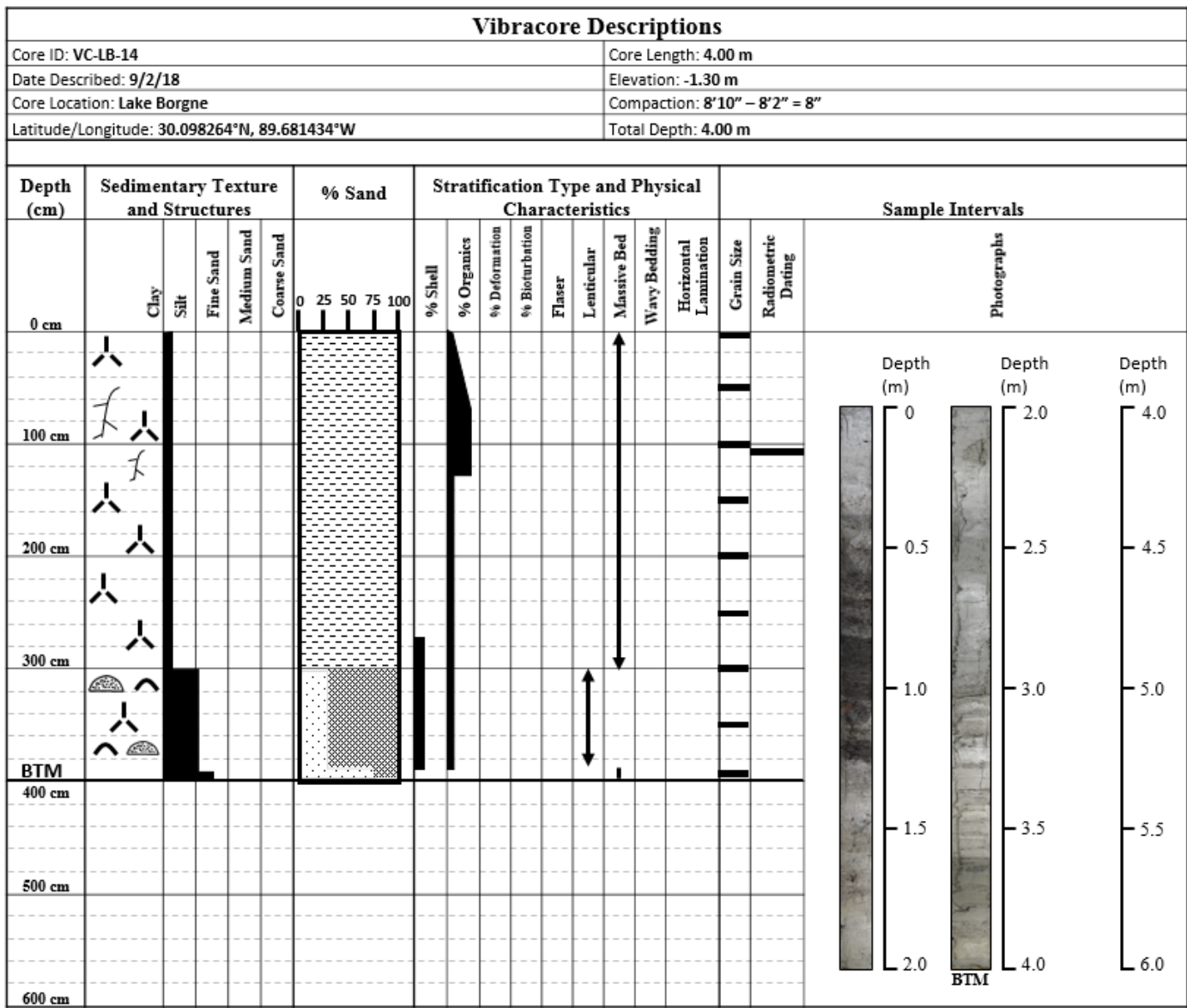
Appendix A Figure 14. Description of core VC-LB-11.



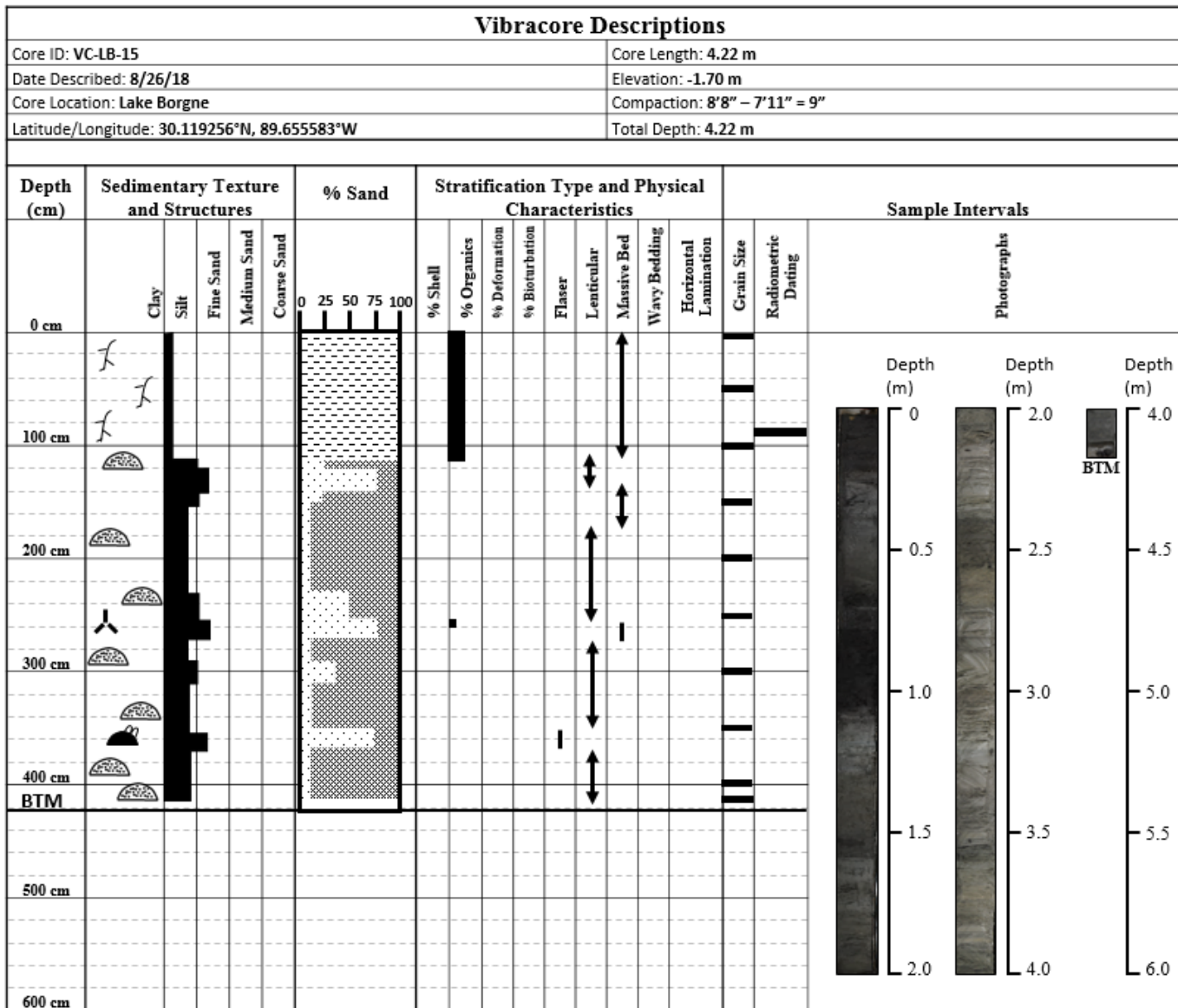
Appendix A Figure 15. Description of core VC-LB-12.



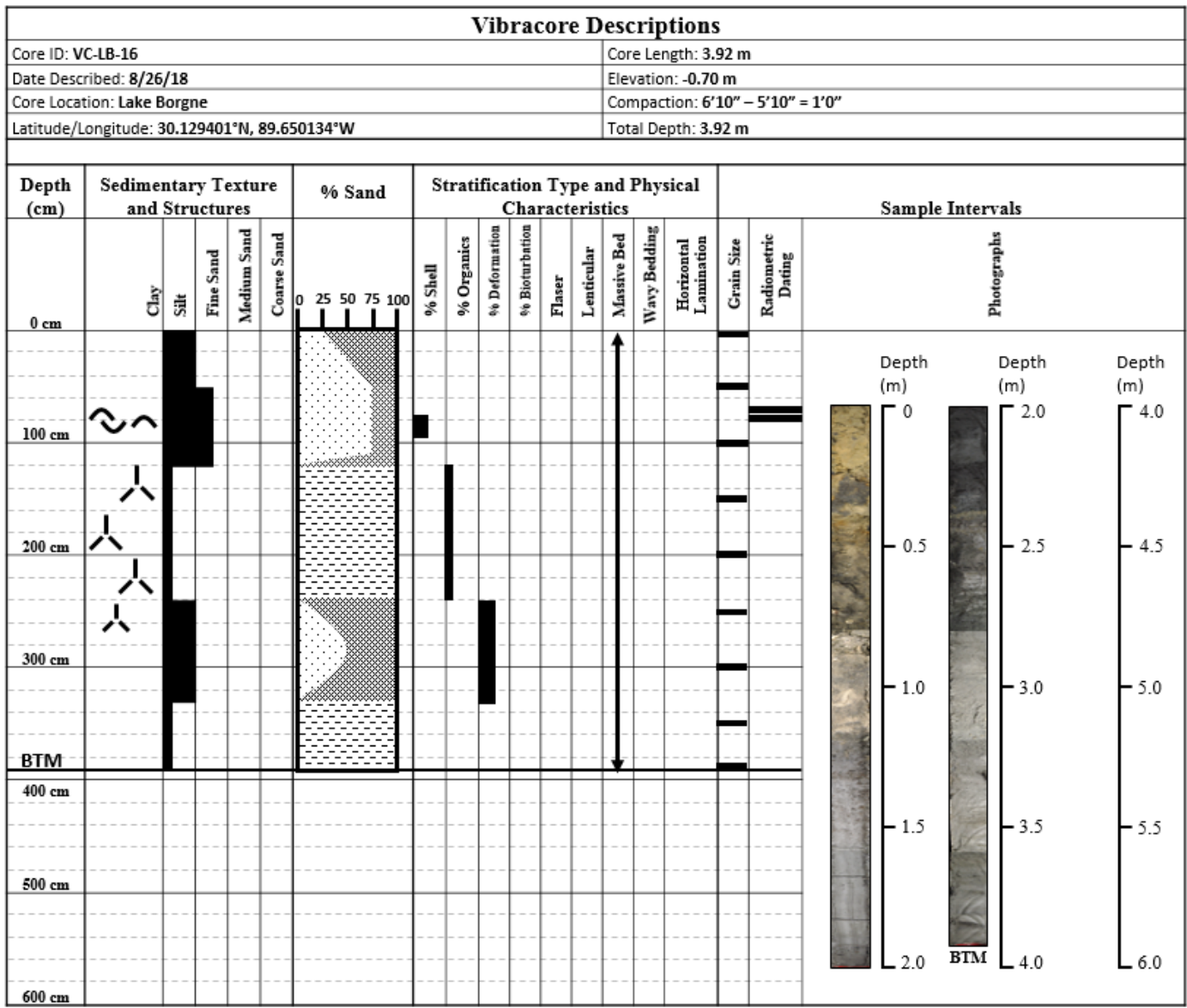
Appendix A Figure 16. Description of core VC-LB-13.



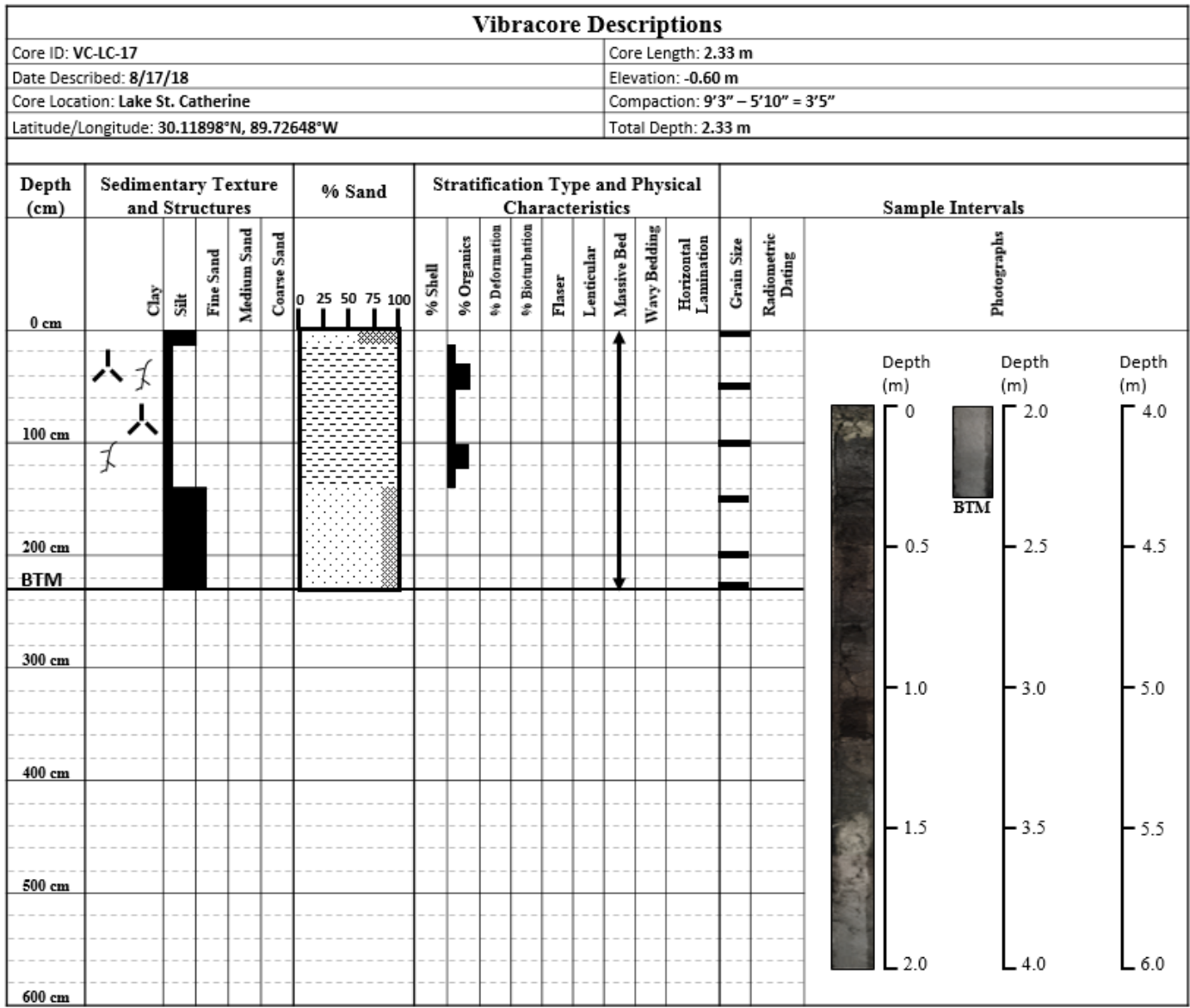
Appendix A Figure 17. Description of core VC-LB-14.



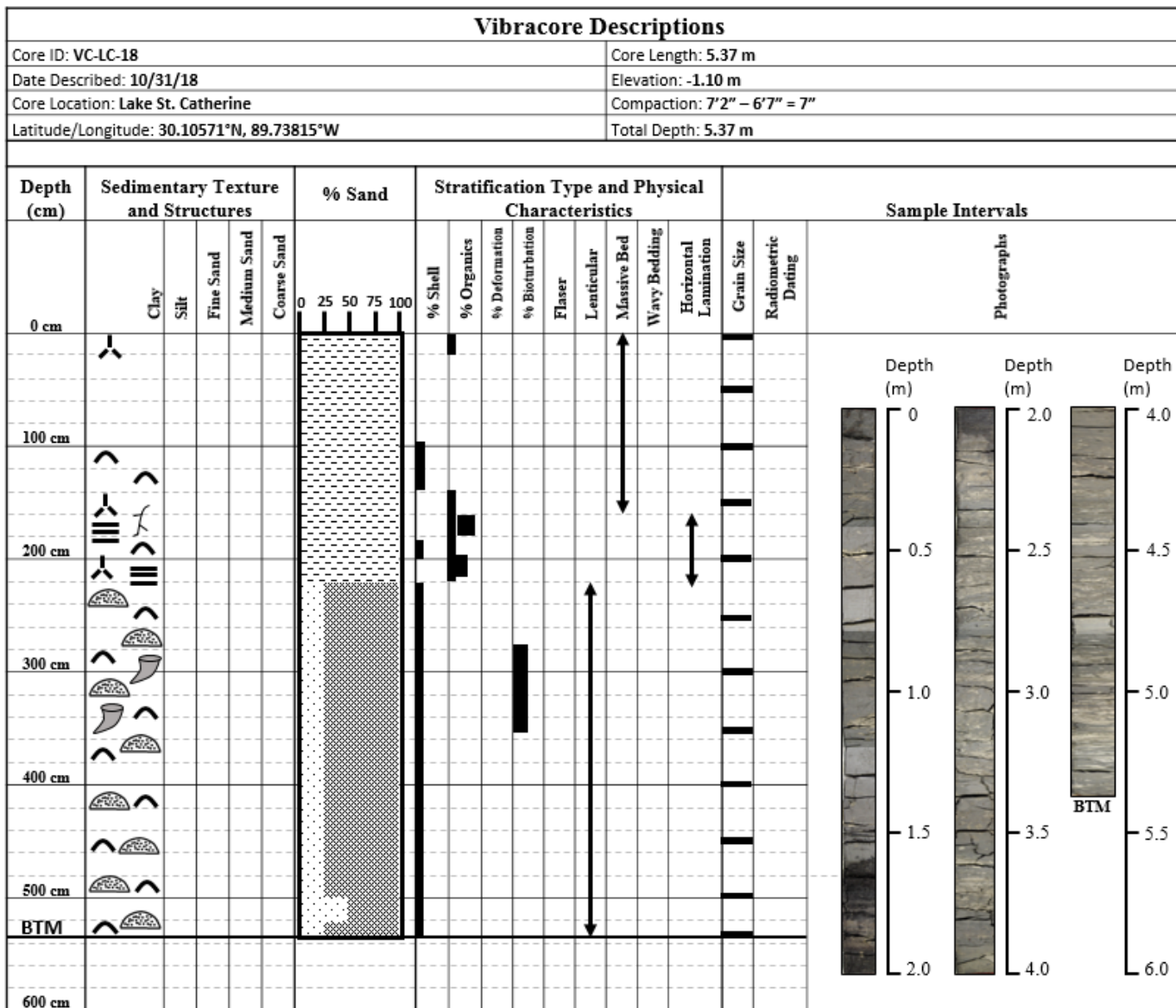
Appendix A Figure 18. Description of core VC-LB-15.



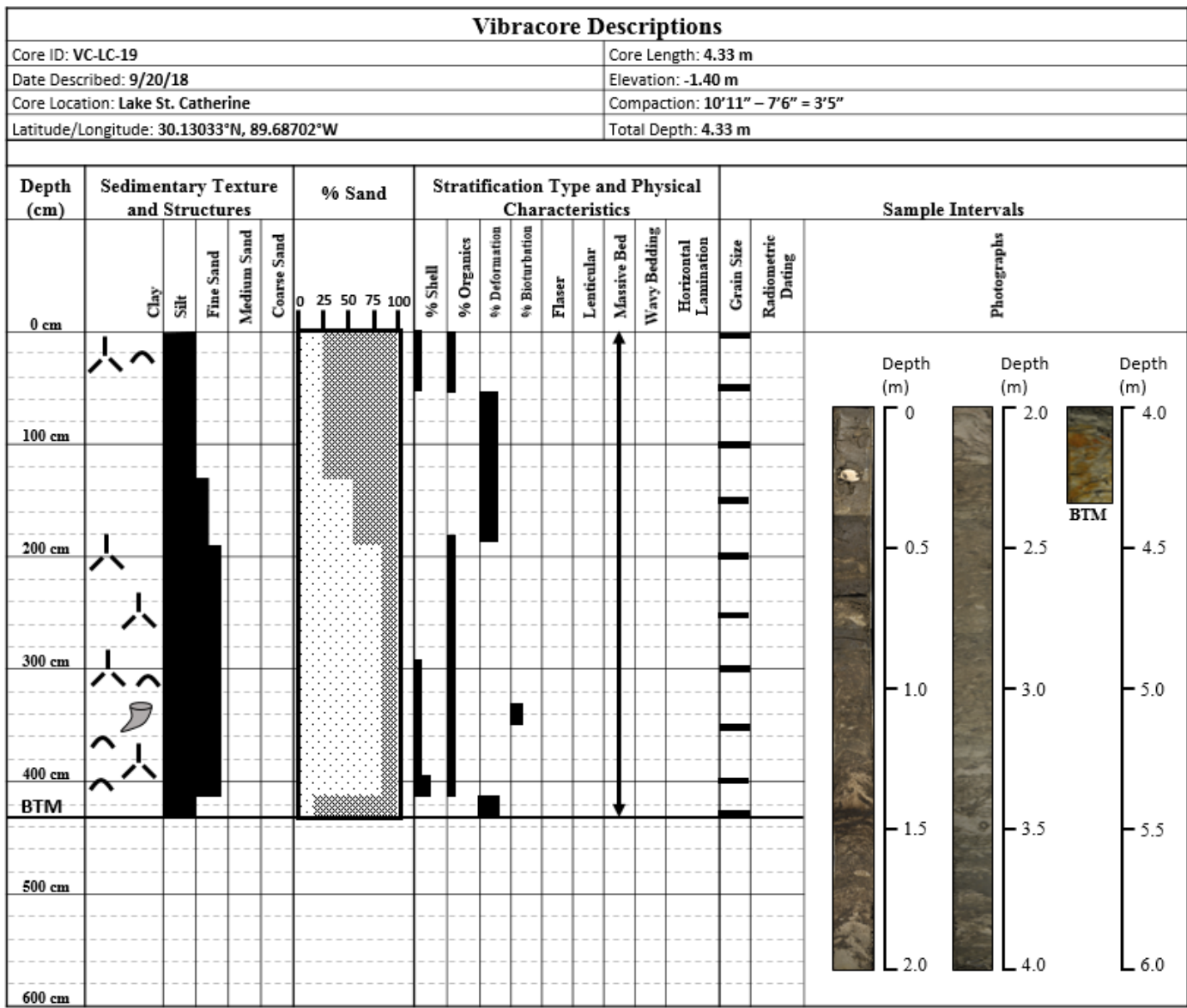
Appendix A Figure 19. Description of core VC-LB-16.



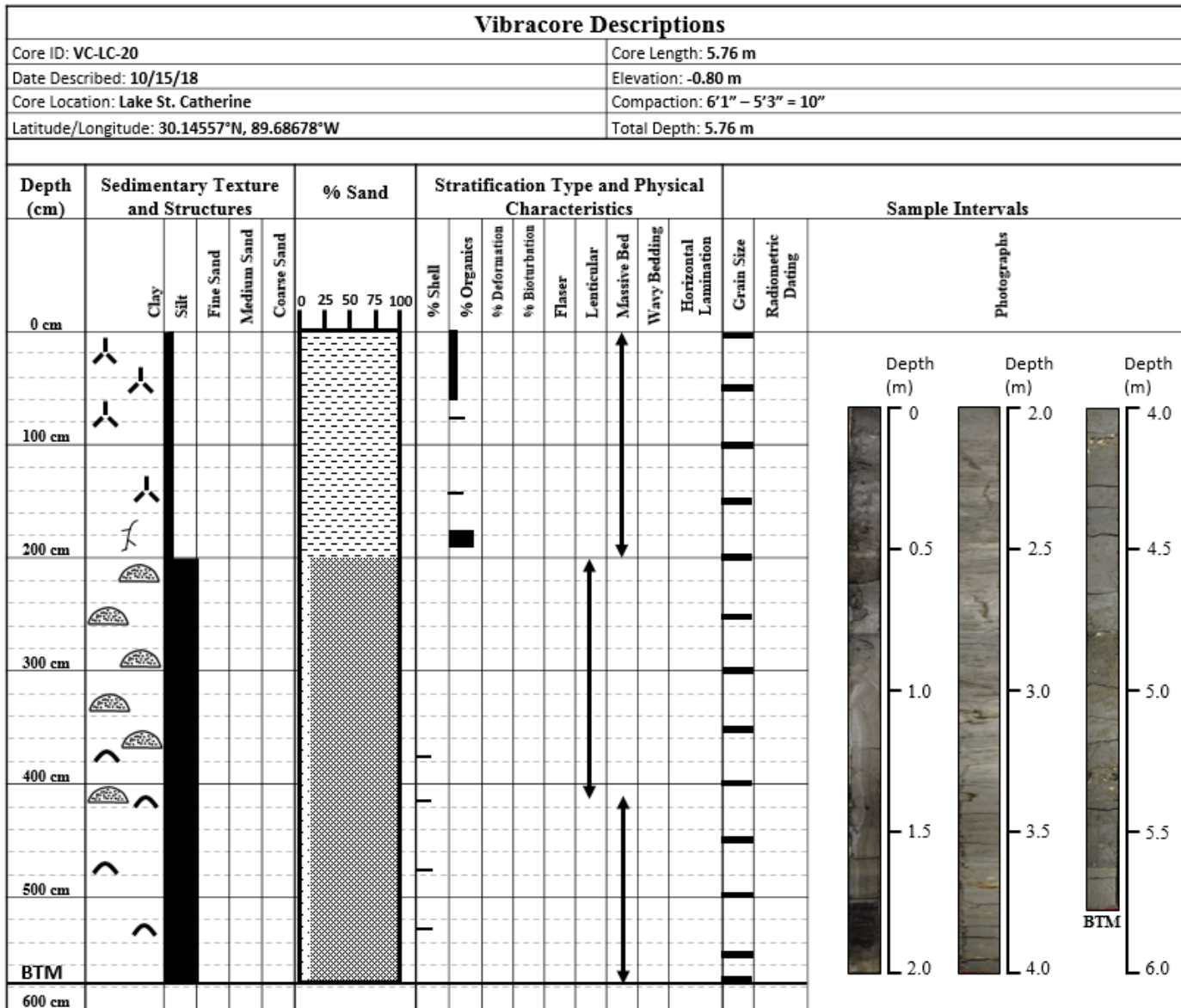
Appendix A Figure 20. Description of core VC-LC-17.



Appendix A Figure 21. Description of core VC-LC-18.



Appendix A Figure 22. Description of core VC-LC-19.



Appendix A Figure 23. Description of core VC-LC-20.

## Appendix B: Chirp Seismic Collection Information

Date:	Line #:	Weather:	Wind:	Seas:	Frequency:	Start Time:	End Time:	Direction:
2/27/19	26	Partly Cloudy	< 5 knts	< 1 ft	2-12 kHz	11:50 AM	12:50 PM	N
2/27/19	27	Partly Cloudy	< 5 knts	< 1 ft	2-12 kHz	1:00 PM	2:00 PM	S
3/25/19	17.001	Partly Cloudy	< 10 knts	1-2 ft	2-10 kHz	N/A	N/A	N
3/25/19	17.002	Partly Cloudy	< 10 knts	1-2 ft	2-12 kHz	N/A	N/A	N
3/25/19	17.003	Partly Cloudy	< 10 knts	1-2 ft	2-10 kHz	N/A	N/A	N
3/25/19	17.004	Partly Cloudy	< 10 knts	1-2 ft	2-12 kHz	N/A	N/A	N
3/25/19	17.005	Partly Cloudy	< 10 knts	1-2 ft	2-10 kHz	N/A	N/A	N
3/25/19	17.006	Partly Cloudy	< 10 knts	1-2 ft	2-12 kHz	N/A	N/A	N
3/25/19	17.007	Partly Cloudy	< 10 knts	1-2 ft	2-10 kHz	N/A	N/A	N
3/25/19	17.008	Partly Cloudy	< 10 knts	1-2 ft	2-12 kHz	N/A	N/A	N
3/25/19	17.009	Partly Cloudy	< 10 knts	1-2 ft	2-10 kHz	N/A	N/A	N
3/25/19	17.010	Partly Cloudy	< 10 knts	1-2 ft	2-12 kHz	N/A	N/A	N
3/25/19	17.011	Partly Cloudy	< 10 knts	1-2 ft	2-10 kHz	N/A	N/A	N
3/25/19	17.012	Partly Cloudy	< 10 knts	1-2 ft	2-15 kHz	N/A	N/A	N
3/25/19	17.013	Partly Cloudy	< 10 knts	1-2 ft	2-10 kHz	N/A	N/A	N
3/25/19	17	Partly Cloudy	< 10 knts	1-2 ft	2-12 kHz	12:30 PM	1:15 PM	N

**Appendix B Table 1.** This table lists weather information, dates, times, azimuth direction of collected lines, and frequency set on Edgetech *Discover* software, for all collected chirp lines in this study.

<b>Date:</b>	<b>Line #:</b>	<b>Weather:</b>	<b>Wind:</b>	<b>Seas:</b>	<b>Frequency:</b>	<b>Start Time:</b>	<b>End Time:</b>	<b>Direction:</b>
3/25/19	15.001	Partly Cloudy	< 10 knts	1-2 ft	2-12 kHz	N/A	N/A	S
3/25/19	15.002	Partly Cloudy	< 10 knts	1-2 ft	2-10 kHz	N/A	N/A	S
3/25/19	15.003	Partly Cloudy	< 10 knts	1-2 ft	2-12 kHz	N/A	N/A	S
3/25/19	15.004	Partly Cloudy	< 10 knts	1-2 ft	2-10 kHz	N/A	N/A	S
3/25/19	15.005	Partly Cloudy	< 10 knts	1-2 ft	2-12 kHz	N/A	N/A	S
3/25/19	15.006	Partly Cloudy	< 10 knts	1-2 ft	2-10 kHz	N/A	N/A	S
3/25/19	15	Partly Cloudy	< 10 knts	1-2 ft	2-10 kHz	1:30 PM	2:30 PM	S
3/25/19	16.001	Partly Cloudy	< 10 knts	1-2 ft	2-12 kHz	N/A	N/A	N
3/25/19	16.002	Partly Cloudy	< 10 knts	1-2 ft	2-10 kHz	N/A	N/A	N
3/25/19	16.003	Partly Cloudy	< 10 knts	1-2 ft	2-12 kHz	N/A	N/A	N
3/25/19	16.004	Partly Cloudy	< 10 knts	1-2 ft	2-10 kHz	N/A	N/A	N
3/25/19	16.005	Partly Cloudy	< 10 knts	1-2 ft	2-12 kHz	N/A	N/A	N
3/25/19	16.006	Partly Cloudy	< 10 knts	1-2 ft	2-10 kHz	N/A	N/A	N
3/25/19	16	Partly Cloudy	< 10 knts	1-2 ft	2-10 kHz	3:00 PM	4:10 PM	N
4/2/19	12	Clear, Sunny	< 13 knts	1-2 ft	2-10 kHz	10:30 AM	11:15 AM	N
4/2/19	13	Clear, Sunny	< 13 knts	1-2 ft	2-10 kHz	11:30 AM	12:15 PM	S

Appendix B Table 1 (cont.).

<b>Date:</b>	<b>Line #:</b>	<b>Weather:</b>	<b>Wind:</b>	<b>Seas:</b>	<b>Frequency:</b>	<b>Start Time:</b>	<b>End Time:</b>	<b>Direction:</b>
4/17/19	20	Mostly Cloudy	< 10 knts	< 1 ft	2-10 kHz	10:30 AM	11:15 AM	N
4/17/19	21	Mostly Cloudy	< 10 knts	< 1 ft	2-10 kHz	11:30 AM	12:15 PM	S
4/17/19	22	Mostly Cloudy	< 10 knts	< 1 ft	2-10 kHz	12:15 PM	1:00 PM	N
4/17/19	23	Mostly Cloudy	< 10 knts	< 1 ft	2-10 kHz	1:15 PM	2:00 PM	S
4/17/19	24	Mostly Cloudy	< 10 knts	< 1 ft	2-10 kHz	2:15 PM	3:00 PM	N
4/17/19	25	Mostly Cloudy	< 10 knts	< 1 ft	2-10 kHz	3:15 PM	4:00 PM	S
4/30/19	10	Mostly Cloudy	< 20 knts	1-2 ft	2-10 kHz	10:15 AM	10:45 AM	S
4/30/19	11	Mostly Cloudy	< 20 knts	1-2 ft	2-10 kHz	11:00 AM	11:30 AM	N
4/30/19	14	Mostly Cloudy	< 20 knts	1-2 ft	2-10 kHz	11:45 AM	12:30 PM	S
4/30/19	18	Mostly Cloudy	< 20 knts	1-2 ft	2-10 kHz	1:00 PM	1:45 PM	N
4/30/19	19	Mostly Cloudy	< 20 knts	1-2 ft	2-10 kHz	2:15 PM	3:15 PM	S
6/9/19	9	Clear, Sunny	< 10 knts	1-2 ft	2-10 kHz	9:45 AM	10:15 AM	N
6/9/19	8	Clear, Sunny	< 10 knts	1-2 ft	2-10 kHz	10:30 AM	11:00 AM	S
6/9/19	7	Clear, Sunny	< 10 knts	1-2 ft	2-10 kHz	11:15 AM	11:45 AM	N
6/9/19	6	Clear, Sunny	< 10 knts	1-2 ft	2-10 kHz	12:00 PM	12:30 PM	S
6/9/19	5	Clear, Sunny	< 10 knts	1-2 ft	2-10 kHz	12:45 PM	1:15 PM	N

Appendix B Table 1 (cont.).

<b>Date:</b>	<b>Line #:</b>	<b>Weather:</b>	<b>Wind:</b>	<b>Seas:</b>	<b>Frequency:</b>	<b>Start Time:</b>	<b>End Time:</b>	<b>Direction:</b>
6/9/19	4	Partly Cloudy	< 10 knts	1-2 ft	2-10 kHz	1:30 PM	2:00 PM	S
6/9/19	3	Partly Cloudy	< 20 knts	2-3 ft	2-10 kHz	2:15 PM	3:00 PM	N
6/9/19	2	Partly Cloudy	< 20 knts	2-3 ft	2-10 kHz	3:15 PM	4:00 PM	S
6/9/19	1	Partly Cloudy	< 20 knts	2-3 ft	2-10 kHz	4:15 PM	5:00 PM	N

Appendix B Table 1 (cont.).

## VITA

The author is originally from Pottstown, Pennsylvania. He earned his B.S. in Geoscience from West Chester University of Pennsylvania and gained valuable experience as a Geotechnical Associate while working for Advanced GeoServices Inc. However, his goal was to attain his M.S. degree and work in the petroleum industry. At UNO, he was part of an UNO Imperial Barrel Award team, which achieved second place at the Gulf Coast regional competition in the spring of 2018. His M.S. thesis research on the Baton Rouge Fault System was partially supported by the RESTORE Act Center of Excellence Program. Analysis of well logs, industry seismic data, shallow vibracores, and Compressed High-Intensity Radar Pulse (Chirp) seismic allowed him to assess the lateral continuity of the BRFS as well as study the history of motion to determine the BRFS is affecting Holocene geomorphology.